

**Theory and Vlasov-code simulations of
thin current sheet
instabilities in collisionless space
plasmas**

Von der Gemeinsamen Naturwissenschaftlichen Fakultät
der Technischen Universität Carolo-Wilhelmina

zu Braunschweig

zur Erlangung des Grades eines
Doktors der Naturwissenschaften

(Dr.rer.nat.)

genehmigte

D i s s e r t a t i o n

von Illia Silin

aus Bachtschissaraj

2004

Bibliografische Information Der Deutschen Bibliothek

Die Deutsche Bibliothek verzeichnet diese Publikation in der Deutschen Nationalbibliografie; detaillierte bibliografische Daten sind im Internet über <http://dnb.ddb.de> abrufbar.

Gedruckt mit Unterstützung des Deutschen Akademischen Austauschdienstes.

1. Referentin oder Referent: Prof. Dr. U. Motschmann

2. Referentin oder Referent: Prof. Dr. M. Scholer

eingereicht am: 19.04.2004

mündliche Prüfung (Disputation) am: 12.07.2004

Copyright © Der Andere Verlag 2004

ISBN X-XXXXXX-XX-X

Der Andere Verlag, Osnabrück

Printed in Germany

Vorveröffentlichungen der Dissertation

Teilergebnisse aus dieser Arbeit wurden mit Genehmigung der Gemeinsamen Naturwissenschaftlichen Fakultät, vertreten durch den Betreuer der Arbeit, in folgenden Beiträgen vorab veröffentlicht:

Publikationen

Silin, I., Büchner, J. & Zelenyi, L. Linear theory and simulations of current sheet instabilities. In: Space Plasma Simulation (Eds.) J. Büchner, Chr. Dum and M. Scholer. Copernicus Gesellschaft e. V.: 352 - 355 (2001).

Silin, I., Büchner, J. & Zelenyi, L. Instabilities of collisionless current sheets: Theory and simulations. Phys. Plasmas 9: 1104 - 1112 (2002).

Silin, I. & Büchner, J. Kinetic instabilities of thin current sheets. Results of 2 1/2D Vlasov code simulations. Phys. Plasmas 10: 1299 - 1307 (2003).

Silin, I. & Büchner, J. Vlasov-code simulations of collisionless plasmas. GWDG Berichte 60: 35 - 50 (2003).

Silin, I. & Büchner, J. Nonlinear instability of thin current sheets in anti-parallel and guided magnetic fields. Phys. Plasmas 10: 3561 - 3570 (2003).

Tagungsbeiträge

Silin, I., Büchner, J. & Wiegmann, T. 2D kinetic simulations of thin current sheet instabilities using a Vlasov code. (Oral). Jahrestagung Arbeitsgemeinschaft Extraterrestrische Forschung, Hamburg (2001).

Silin, I., Büchner, J. & Wiegmann, T. 2D kinetic simulations of thin current sheet instabilities using a Vlasov code. (Oral). European Geophysical Society Annual Assembly, Nice (2001).

Silin, I., Büchner, J. & Zelenyi, L. Linear theory and Vlasov code simulations of current sheet instabilities. (Poster). International School on Plasma Simulations, Garching (2001).

Silin, I., Büchner, J. & Zelenyi, L. Analytical investigation and numerical simulations of instabilities of thin current sheets. (Poster). Jahrestagung Arbeitsgemeinschaft Extraterrestrische Forschung, Leipzig (2002).

Silin, I., Büchner, J. & Zelenyi, L. Analytical investigation and numerical simulations of instabilities of thin current sheets. (Poster). European Geophysical Society Annual Assembly, Nice (2002).

Silin, I. & Büchner, J. Nonlinear instability of thin current sheets with magnetic shear. (Oral). Jahrestagung Arbeitsgemeinschaft Extraterrestrische Forschung, Jena (2003).

Silin, I. & Büchner, J. Instability of thin current sheets with magnetic shear. (Poster). European Geophysical Society Annual Assembly, Nice (2003).

Silin, I. & Büchner, J. 3D Vlasov-code simulations of current sheet instabilities. (Poster). 26-th International Conference on Processes in Ionized Gases, Greifswald (2003).

Silin, I. & Büchner, J. Coupling of waves and reconnection in thin, collisionless current sheets. (Poster). American Geophysical Union fall meeting, San Francisco (2003).

Silin, I. & Büchner, J. Vlasov-code simulations of reconnection through magnetopause-like current layers. (Oral). European Geophysical Union General Assembly, Nice (2004).

Notation¹

β	plasma beta, i.e. thermal to magnetic pressure ratio
γ	instability growth rate
λ	instability wavelength
λ_D	Debye length
λ_{LH}	lower-hybrid wavelength
Ω	instability oscillation frequency
$\omega = \Omega + i\gamma$	complex instability frequency
ω_{pi}	ion plasma frequency
ω_{pe}	electron plasma frequency
Ω_{0i} or Ω_i	ion gyro-frequency
Ω_{0e} or Ω_e	electron gyro-frequency
Ω_{LH}	lower-hybrid frequency
ϵ_0	vacuum dielectric constant
μ_0	free space magnetic permeability
ϕ	electrostatic potential
ρ	charge density
θ	angle between a wavevector and magnetic field direction ²
Θ	angle between asymptotic magnetic fields at the magnetopause
\mathbf{A}	vector-potential
\mathbf{B}	magnetic field, identical to magnetic induction
B_0	asymptotic magnetic field outside the current sheet
B_{y0}	uniform guide magnetic field

c	speed of light
\mathbf{E}	electric field
e	elementary charge
f	particle distribution function
\mathbf{j}	electric current density
\mathbf{k} and k	wavevector and wavenumber
$k_{LH} = 2\pi/\lambda_{LH}$	lower-hybrid wavenumber
L_z	current sheet half-width
m_i and m_e	ion and electron masses
m_i/m_e	particle mass ratio
n	particle number density
n_0	maximum particle number density at the current sheet center
ρ_i	ion gyroradius
ρ_e	electron gyroradius
ρ_{0i}	ion gyroradius in the asymptotic magnetic field B_0
ρ_{0e}	electron gyroradius in the asymptotic magnetic field B_0
T_i and T_e	ion and electron temperatures ³
T_i/T_e	particle temperature ratio
u_i and u_e	ion and electron drift velocities, respectively
\mathbf{v}	particle velocity
\mathbf{v}_s	sound speed
$v_{th,i}$	ion thermal velocity
$v_{th,e}$	electron thermal velocity
\mathbf{v}_w	phase velocity of a wave
z	direction normal to the current sheet plane

¹Symbols which occur only rarely are not given.

²All angular quantities in this work are expressed in radians.

³Everywhere in this work temperature is expressed in energy units, already containing the Boltzmann's constant κ .

Contents

Notation	v
Summary	3
Acknowledgements	7
1 Introduction	9
1.1 The relevance of thin current sheets	9
1.2 Instabilities of thin current sheets	12
1.3 Open questions and aims of the present work	16
2 Thin current sheet models	23
2.1 Symmetric current sheets	23
2.2 Magnetopause-like current sheets at the boundary between two plasmas	26
3 Linear theory of instabilities in thin Harris current sheets	31
3.1 Previous kinetic linear perturbation theories of thin current sheets	31
3.2 Derivation of linear perturbation theory of thin Harris sheets	32
3.3 Numerical solutions of dispersion relation	39
4 Vlasov-code simulations	45
4.1 Description of the numerical code	45
4.2 Parallelization architectures	49
4.2.1 OpenMP	50
4.2.2 Message-Passing Interface (MPI)	51
4.2.3 Hybrid architecture	54

5	Simulation results	61
5.1	Thin current sheets with anti-parallel magnetic fields	61
5.1.1	Resonant interaction of lower-hybrid drift waves with ion flow . .	61
5.1.2	Coupling between the resonantly amplified lower-hybrid drift waves and the eigenmodes of the current sheet	65
5.2	Thin current sheets with guided magnetic fields	73
5.3	Magnetopause-like boundaries	80
5.4	Comparison of simulation results with space experiments	86
6	Summary of the main results	91
	Bibliography	95
	Curriculum Vitae	107

Summary

This work discusses the results of analytical and numerical investigations of thin current sheets in collisionless space plasmas. Current sheets are relatively thin layers of counterstreaming charged particles, occurring in the regions where magnetic field rotates. They are formed due to plasma trapping in the minimum magnetic field. These structures are encountered in the Earth magnetosphere, e.g. in geomagnetic tail and at the magnetopause, or in solar corona, ion cometary tails, galactic nuclei, as well as in laboratory plasma experiments. Although current sheets may be quasi-stable, they can give rise to a number of various instabilities. The dissipation of current sheets is associated with the explosive release of magnetic field energy called magnetic reconnection. During this process part of the energy stored in the magnetic fields outside the current sheet is partially transformed into the thermal and kinetic energy of plasma and energetic particles.

The main tools for studying the current sheet dynamics are linear perturbation theories, numerical simulations and space experiments. The disadvantage of linear perturbation theories is that they take in consideration only part of the physical processes. On the other hand, though simulations allow consideration of all possible physical processes including their nonlinear interactions, there are usually strong technical limitations imposed by computer hardware. For example, it has become a usual practice to use artificially small particle mass ratios, which in turn lead to artificial ratios between plasma parameters such as particle gyroradii and Debye length or cyclotron and plasma frequencies. These technical problems make the scaling of the simulated phenomena and their comparison to realistic conditions rather non-trivial. As for the space experiments, their disadvantage is that so far only local measurements were carried out, while the reconnection is a non-local process. This usually provides too much freedom for imagination

during the physical interpretation of the measurements.

Because of the complexity of the problem and different methods used for investigations, all having their specific application ranges and disadvantages, there are still many open questions. We try to combine the analytical and numerical methods and investigate this way the most basic processes which, according to the present knowledge, might play an important role in magnetic reconnection. In particular, this work is devoted to plasma evolution on the small kinetic scales. An attempt is made to compare the results of analytical linear theory and numerical kinetic simulations with in-situ observations for a specific case of thin collisionless current sheets, like e.g. in Earth magnetosphere. The following questions are addressed:

- The role of electrostatic effects in the evolution of linearly unstable cross-field eigenmodes of thin current sheets
- The role of microscopic unstable waves in the nonlinear evolution of current sheet decay
- Basic physical process leading to the magnetic energy dissipation in course of collisionless reconnection through thin current sheets
- The influence of magnetic guide field on the unstable modes active in the current sheets
- The role of finite plasma beta and magnetic field rotation at the magnetopause-like boundaries on their stability

A linear perturbation theory is developed in order to investigate the behaviour of eigenmodes of thin current sheet. For simplification of the dispersion relation analysis we make several simplifying assumptions. We consider perturbations symmetric around the current sheet central plane with wavelengths large compared to the current sheet thickness. This way we focus our investigation on symmetric sausage eigenmodes of current sheets which are so far less investigated compared to their asymmetric counterpart, the kink mode. At the same time, the simplified dispersion relation allows us to investigate the eigenmodes propagating in all directions in the current sheet plane. The long-wavelength

approximation is chosen, because traditionally it was believed that long waves are most important in the current sheet dynamics. Also, during the calculation of perturbation integral in Vlasov equation we assume the straight-line motion of particles similarly to the guide-center motion approximation. These simplifications allow us to reduce the system of integro-differential equations to a system of linear algebraic equations and obtain a relatively simple dispersion relation. In order to separate the role of electrostatic perturbations from the electromagnetic mode we consider independently the full dispersion relation and the reduced one, with electrostatic part neglected. In the absence of electrostatic perturbations the numerical solution of the reduced dispersion relation has two branches - electron and ion modes for all propagation angles in the current sheet plane. When, however, the electrostatic perturbations are included in the consideration, the ion branch disappears completely and only the electron solution remains in the propagation angles range $\theta < \pi/8$. Thus, we find that electrostatic perturbations stabilize all linear long-wavelength eigenmodes of thin current sheets except the aperiodic electron tearing-mode instability.

A numerical simulation code was developed, which directly solves the Vlasov-Maxwell system of equations and enables one to self-consistently describe the evolution of collisionless plasmas. A series of numerical simulations of thin current sheets was carried out and the results were compared to the linear theory predictions. It turns out, that, contrary to the expectation from the linear theory, the current-aligned modes are not stabilized. However, the wavelength of the dominant mode steadily shortens with the increasing particle mass ratio and the long-wavelength approximation $kL_z < 1$ is no longer applicable for mass ratios $m_i/m_e > 16$. Thus, the linear theory results suggest that the instabilities of thin current sheets obtained in numerical simulation studies are due to a nonlinear small-scale kinetic process.

The simulations of current sheets in the antiparallel magnetic fields show that the lower-hybrid-drift (LHD) waves, which appear at the edges of the current sheet, get in Landau-resonance with the ion flow and grow exponentially. As they grow, they also expand from the current sheet edges towards the central plane and trigger a global instability of the current sheet. This global wave-mode inherits the wavelength and oscillation frequency from the lower hybrid waves and grows on a typical ion gyroperiod time scales.

It can directly couple to the orthogonal tearing-mode instability and cause rapid three-dimensional reconnection.

In the presence of current-aligned guide magnetic field the LHD waves propagate obliquely to the current direction. Hence, the waves encounter fewer resonant ions and grow slower. Since the waves at the opposite edges of the sheet are no longer aligned with each other they can no longer couple to the global eigenmodes of the current sheet. In this configuration the magnetic field lines no longer form the classical X- and O-line reconnection pattern. Instead, they form chaotic vortices, twisting around each other and wandering further to the periphery of the current sheet. This eventually allows plasma diffusion across the current sheet plane and can be relevant for explaining flux-transfer events (FTE's) through the Earth magnetopause.

Vlasov simulations were also used to investigate the stability of the magnetopause-like tangential discontinuities separating two plasmas with different densities and temperatures with rotating magnetic field. In order to make our results more realistic we developed a dynamical equilibrium model for the plasma and magnetic fields at the magnetopause. Over the years two opposite opinions formed concerning the question of whether magnetic reconnection at the magnetopause occurs only in the regions where the magnetic fields are locally anti-parallel across the magnetopause or whether reconnection is possible also when the magnetic fields are sheared by a smaller angle (so-called "component reconnection"). So far, all previous theoretical results suggested that the "component reconnection" is either very weak or is completely suppressed. On the other hand, many investigations, theoretical, numerical and experimental, pointed at very strong lower-hybrid (LH) waves at the magnetopause with electric field amplitudes up to 10 mV/m. In agreement with some of these findings our simulations reveal strong activity of transverse electrostatic lower-hybrid waves at the magnetospheric side of the density gradient. Because we used a rotating magnetic field across the magnetopause, the drift direction of the LH waves is also turning at different magnetic horizons. Hence, the resonant interaction with particles was very weak and as a result the short waves coalesced and produced long tearing-type wavelengths, which eventually lead to reconnection and plasma diffusion across the magnetopause. This process seems to be independent of the magnetic field rotation angle, and thus favours the concept of "component reconnection".

Acknowledgements

The author acknowledges the financial support of Deutscher Akademischer Austauschdienst (DAAD) during the work on this Ph.D. thesis. The help of Dr. Thomas Wiegelmann is acknowledged for introduction to the numerical methods and the initiation of the Vlasov code simulations. Professor Lev Zelenyi is acknowledged for motivation and guidance during the work on the linear theory. Professor Dr. Uwe Motschmann is acknowledged for his careful reading of the manuscript and constructive suggestions concerning its improvement. The help of Professor Oswald Haan and Dr. Ulrich Schwartzmann of Gesellschaft für Wissenschaftliche Datenverarbeitung mbH Göttingen (GWDG) in parallelization and optimization of the numerical code is acknowledged. The help of Dr. Dieter Schmitt in preparing the manuscript for publication is greatly appreciated. Finally, my greatest thanks goes to Dr. Jörg Büchner, who inspired and supported this work in every possible way.

Chapter 1

Introduction

1.1 The relevance of thin current sheets

In astrophysics and space plasma physics current sheets play an important role. The main reason is that on the vast interplanetary distances the plasma is usually "frozen" into the magnetic field which limits the variety of processes there to few rather well-studied instabilities and waves. Current sheets usually build up in the so-called critical regions of magnetic fields, where the field changes direction (see e.g. *Syrovatskii (1971); Bulanov et al. (2002)*). A schematic current sheet configuration used in the present work is demonstrated in Figure (1.1). Current sheets play the role of magnetic traps where plasma is accumulated. Plasma pressure inside the current sheet is balanced by the magnetic field pressure from outside, while the current is maintained by the rotation of the magnetic field through the current sheet. This balance makes current sheets quasi-stationary features in space and laboratory plasmas. Such current sheets with the thickness of the order of few ion gyroradii or even less have been observed by in-situ measurements in Earth magnetosphere (see e.g. *Pulkkinen et al. (1992); Sergeev et al. (1993); Øieroset et al. (2001); André et al. (2004)*). Current sheet models were also used to explain solar flares (*Priest (1976, 2001)*) (see Figure (1.2)).

The main reason why current sheets cause such interest is that the most dynamic processes in interplanetary plasmas occur there. In the perfectly conducting space plasma the current sheets are the primary sites of rapid magnetic energy dissipation. This dissi-

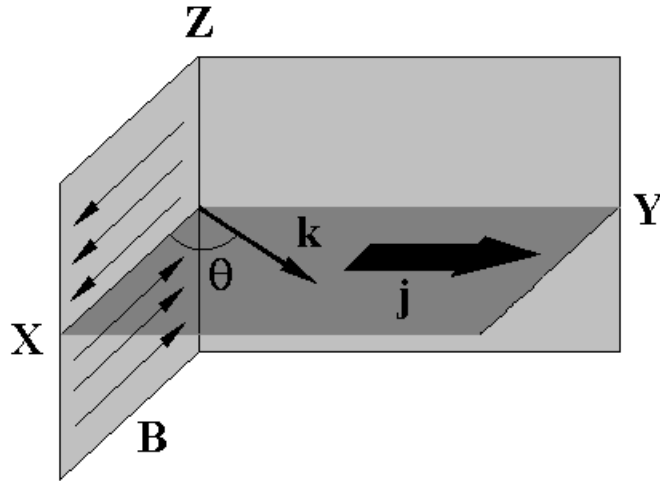


Figure 1.1: A sketch of a current sheet geometry. Unless specified otherwise, the magnetic field B is anti-parallel at the opposite sides of the sheet and has only x-component. The current j flows in the y-direction and z-axis is normal to the current sheet plane. The investigated instabilities propagate in the current sheet plane with a wavevector k , which can make an arbitrary angle θ with the x-axis.

pation occurs due to various types of waves and instabilities which grow in thin current sheets. The dynamics of plasma in these regions becomes very complicated and is still not fully understood. In general, the explosive dissipation of current sheets is identified as "magnetic reconnection", although the original identification of reconnection just with collisionless tearing-mode instability now becomes more diffuse and includes a number of various processes.

Here are a few examples of astrophysical and interplanetary phenomena where reconnection plays an important role. In solar flares reconnection leads to release of enormous amount of energy in a very short time (see e.g. *Parker (1957); Priest (2001); Kusano (2001)*). As a result, huge clouds of hot plasma are ejected from the solar atmosphere into the outer space with a velocity of up to 10^3 km/s, accompanied by bursts of highly energetic particles. Reconnection is also thought to play a leading role in coronal heating (*Dmitruk et al. (2002)*), accounting for the tremendous temperature gradient between the solar chromosphere and the corona (from $6 \cdot 10^3$ K to 10^6 K). Also, strong particle acceleration (sometimes to high relativistic energies) in astrophysical plasmas, e.g. in active

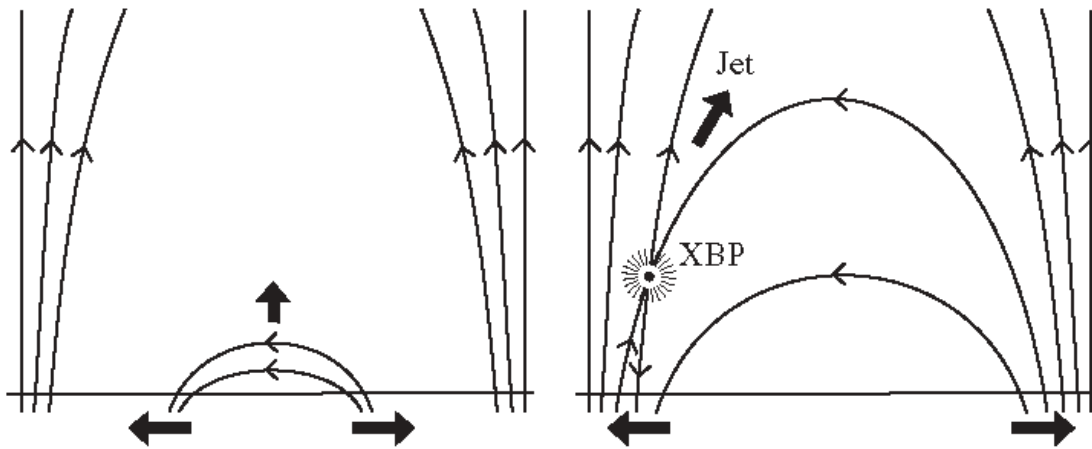


Figure 1.2: A schematic geometry of reconnection in solar atmosphere at the foot of a magnetic loop (taken from *Priest* (2001)).

galactic nuclei (*Lesch and Reich* (1992); *Lesch and Birk* (1997); *Schopper et al.* (1998); *Kobak and Ostrowski* (2000)), extragalactic jets (*Lesch and Birk* (1998)) or stellar flares (*Schaefer et al.* (2000)), is associated with magnetic reconnection. But, perhaps, the most well-studied example of magnetic reconnection is at the Earth magnetopause (*Sonnerup et al.* (1981); *Øieroset et al.* (2001); *Russell* (2003)) and in the Earth magnetotail (*Coppi et al.* (1966); *Bieber et al.* (1984); *Birn and Hesse* (1994); *Slavin et al.* (2002)). Figure (1.3) gives a simplified impression of where the reconnection can occur (N marks the so-called "neutral point", the center of the reconnection region) in case of southward or northward interplanetary magnetic field (IMF) orientation. At the magnetopause, reconnection leads to penetration of the energetic solar wind particles into the inner magnetosphere. This eventually causes polar aurora in the Earth ionosphere. The reconnection in the far tail of the magnetosphere, the so-called magnetic substorms, causes strong perturbations of the magnetic field in the magnetosphere and at the Earth surface. Such magnetic field changes were found to generate induction currents in oil and gas pipelines and high voltage networks in the high latitude regions of up to 100 Amperes.

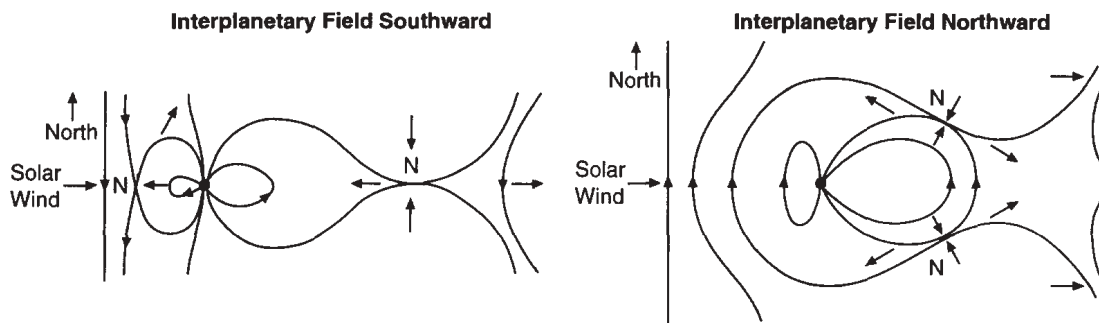


Figure 1.3: A schematic geometry of reconnection at the Earth magnetosphere for southward (left) and northward (right) interplanetary magnetic field (IMF) (taken from *Dungey* (1961, 1963)).

1.2 Instabilities of thin current sheets

Although thin current sheets can build up in the magnetic field critical regions and reach an equilibrium state, they are a subject to a large number of instabilities. The instabilities can use various free-energy sources, that are available in thin current sheets, for example, relative particle drift or plasma and magnetic field gradients. In turn, the fastest growing instabilities can alter the equilibrium situation and give rise to secondary instabilities by introducing, e.g. tangential plasma velocity shear or particle beams. Since this work focuses on collisionless space plasmas, i.e. very rarefied and hot matter where direct particle collisions can be neglected, the instabilities which are saturated in laboratory plasma by collisions can still be important for our investigation. But on the other hand, the particular conditions in the Earth magnetosphere, which is our main application, are usually such that not all possible plasma instabilities can be encountered. We shall give here a short account of instabilities which are known to exist in current sheets in Earth magnetosphere and discuss the particular conditions favouring or stabilizing each of them.

Collisionless **tearing-mode instability** is the most important plasma instability which controls the global plasma dynamics in the Earth magnetosphere. It is an aperiodic standing long-wavelength mode with a wavevector parallel to the ambient magnetic field. Tearing-mode instability is purely electromagnetic, i.e. electrostatic perturbations do not play any significant role in it. It grows in current sheets separating anti-parallel magnetic

fields and transforms a fraction of energy stored in magnetic fields into plasma kinetic and thermal energy through the inverse Landau-resonance with electrons. *Coppi et al.* (1966) first proposed that the collisionless linear tearing mode instability of current sheets leads to reconnection and substorms in the Earth magnetotail. Later, non-symmetric tearing-mode instability was proposed for reconnection at the Earth magnetopause (see e.g. *Sonnerup and Ledley* (1979); *Greenly and Sonnerup* (1981)). Different analytical models have been proposed for the tearing-mode instability (see e.g. *Petschek and Thorne* (1967); *Parker* (1973)), including slow shock waves, which could accelerate plasma outside the central "diffusion region", but unfortunately, the growth rate of the linear tearing-mode instability was still too small to explain the observations. Thus, it was concluded that linear tearing-mode instability alone cannot account for the rapid onset of the observed magnetic reconnection, since it saturates early and can be easily stabilized by a normal magnetic field component perpendicular to the current sheet plane (see *Lembege and Pellet* (1982)). Also, the magnetohydrodynamic (MHD) and fluid theories require an *ad-hoc* resistivity, which results from the microscopic kinetic processes. Thus, the MHD picture of reconnection can not be a consistent one and the problem of thin current sheet stability has to be considered in the kinetic approach. This approach immediately multiplies the number of possible instabilities and makes the picture far more complicated.

Another long-wavelength instability which is known from the MHD and fluid investigations is the **Kelvin-Helmholtz instability (KHI)** (see e.g. *Melrose* (1986)). This instability is driven by tangential velocity shear and exists both in magnetized and unmagnetized plasmas. For example, KHI can be excited when a current sheet is surrounded by a stationary background plasma. It was found in MHD and kinetic approaches that in such situation, even if the density of the background plasma is very small, the current sheet will start kinking and eventually disintegrate after approximately 100 ion gyroperiods (*Lee et al.* (1988); *Daughton* (1999a)). However, the growth rate of KHI is so small compared to most kinetic instabilities, that it usually comes into play when many other instabilities have already reached a strongly non-linear stage and significantly modified the current sheet. KHI can be separated from such fast kinetic processes only in fluid and MHD approximation.

An important class of instabilities is eigen-oscillations of current sheet proper. These

are kinetic plasma instabilities, which can be investigated either by linear kinetic theory or by kinetic numerical simulations (for example, *Yamanaka (1978); Pritchett et al. (1996); Lapenta and Brackbill (1997); Yoon et al. (1998); Daughton (1998)*). Traditionally, these eigen-modes are divided into two classes: an anti-symmetric **kink-mode instability**, also sometimes called **drift-kink instability (DKI)** and a symmetric **sausage-mode instability** or **drift-sausage instability (DSI)**. These instabilities are purely electromagnetic drifting plasma waves with the wavevector perpendicular to the ambient magnetic field.

Recently *Karimabadi et al. (2003a,b)* carried out analytical and numerical investigation of a thin current sheet in a stationary background plasma and found a kinetic **ion-ion kink instability (IIKI)**. This instability grows due to velocity shift between two ion populations inside the current sheet and a tangential velocity shear at the edges, electrons do not play any role in it. It has a long wavelength $kL_z \sim 1$ and a growth rate of approximately $\gamma \sim 0.18$ (in a current sheet with a half-width of an ion gyro radius $L_z = \rho_{0i}$). This growth rate puts the IIKI somewhere in between the KHI (the slowest-growing instability) and the kinetic DKI and DSI (relatively fast instabilities).

Apart from the global instabilities which evolve on the scales of ion gyroradii and affect the entire current sheet there are also local instabilities, which have a much shorter wavelength and reside only at the periphery of the current sheet. The most universal of these is the **lower-hybrid drift instability (LHDI)** (see e.g. *Davidson and Gladd (1975); Davidson et al. (1976); Davidson and Krall (1977); Huba et al. (1977, 1980); Winske and Liewer (1978); Winske (1981)*). This instability uses the plasma density and magnetic field gradients as the free-energy source and is always encountered by spacecraft in the vicinity of magnetotail and magnetopause current sheets (*Gurnett et al. (1976); Vaisberg et al. (1983); Lucek et al. (2001); Bale et al. (2002); Vaivads et al. (2004)*). It has a typical wavelength of the hybrid ion-electron scale $\lambda_{LH} = (\rho_i \rho_e)^{1/2}$ and oscillation frequency $\Omega_{LH} = \omega_{pi}(1 + \omega_{pe}^2/\Omega_e^2)^{-1/2}$, which in the typical magnetospheric conditions can be simplified to $\Omega_{LH} \approx (\Omega_i \Omega_e)^{1/2}$. The growth rate of LHDI is typically a fraction of its oscillation frequency and is rather large compared to the previously discussed global instabilities of current sheets. LHDI can be described both in two-fluid and kinetic approximations, depending on the local diamagnetic drift velocity: fluid - strong drift and kinetic - weak drift. *Yoon et al. (2002)* developed an eigen-oscillation theory for thin

current sheets and found that the lower-hybrid drift (LHD) waves were in fact higher-order eigenmodes of current sheets, while the lower-order modes corresponded to kink and sausage instabilities. In this class of instabilities the quasi-electrostatic LHDI is the fastest growing unstable mode residing at the current sheet edges. Thus, theoretically, in the first few gyroperiods LHD waves should be observed at the periphery of the current sheet and later a longer-wavelength global instability should grow. According to this theory, for small particle mass ratios $m_i/m_e < 100$ asymmetric kink mode should dominate, while for higher mass ratios sausage-mode instability is more probable.

Among current-driven instabilities the most common one is **ion-acoustic** or **ion-sound instability** (*Krall and Trievelpiece (1973); Melrose (1986)*). The ion-acoustic waves are generated by resonant interaction of drifting electrons with electrostatic field perturbations. They can propagate in plasmas with $T_e \gg T_i$ and are strongly damped in plasmas with $T_e \sim T_i$. As a special branch of ion-acoustic instability one finds also **Buneman instability** (*Buneman (1958); Melrose (1986); Tsytovich (1995)*). This mode is also driven by resonance between electron beam and electrostatic plasma perturbations, but it appears in the strong-drift regime when electron drift velocity is much larger than the electron thermal velocity $u_e \gg v_{th,e}$. This situation corresponds to the so-called "cold electron beam" plasma. However, this condition is much stronger than the $u_e > u_s$ for the ion-acoustic waves. Thus one would expect that ion-acoustic waves develop first and prevent the Buneman instability from ever occurring. However, in Earth magnetosphere and magnetosheath proton temperature is typically an order of magnitude larger than electron temperature, $T_i \approx 10T_e$, and hence, ion-acoustic waves are strongly damped. In addition, in the magnetospheric plasmas the drift velocity of electrons can exceed their thermal velocity only in exceptional cases and Buneman instability is a rather exotic phenomenon.

A special class of metastable (i.e. stable in linear approximation but unstable in the non-linear regime) **drift-tearing instabilities** has been found theoretically by *Galeev et al. (1985); Kuznetsova and Zelenyi (1985, 1990a)* for current sheets in the presence of the uniform current-aligned guide field. This instability could lead to a destruction of the magnetic surfaces, beginning at the center of the current sheet, and propagating further to the periphery. The growth rate and wavelength of such mode was predicted to strongly depend on the propagation angle. Short-wavelength modes should appear closer

to the center of the sheet, grow faster and resemble the classical aperiodic tearing instability. The modes which grow later at the peripheral magnetic surfaces should have longer wavelengths, grow slower and resemble a MHD-like kink instability. Basing on these results the authors proposed a model of **stochastic percolation** of plasma across current sheets in course of drift-tearing-mode activity (see *Kuznetsova and Zelenyi (1990b)*). The authors argued that if the unstable modes grow at all magnetic surfaces the magnetic field lines will reconnect at random so that eventually some of them will start on one side of the current sheet and end on the other. This process could explain e.g. the possibility of flux transfer events (FTE's) at Earth magnetopause. However, so far the drift-tearing instability has not been confirmed by any other investigation. Some particle-in-cell (PIC) simulations of current sheets with guide field have been carried out recently by *Scholer et al. (2003)* and *Pritchett and Coroniti (2004)*. The results of *Scholer et al. (2003)* suggest that the guide field $B_y \sim B_0$ decreases the reconnection rate by a factor of three, but the structure of the reconnected field clearly demonstrates a two-dimensional tearing-mode instability. *Pritchett and Coroniti (2004)* investigated forced reconnection by introducing the initial X-line, as in the Geomagnetic Environment Modelling (GEM) challenge (see e.g. (*Birn et al., 2001*)). They found that the guide fields $B_y \sim B_0$ did not change the reconnection rate and the current sheet decayed through the tearing-mode instability, although the structure of the reconnection region was altered by the guide field.

1.3 Open questions and aims of the present work

The existing knowledge about thin current sheets gives some idea about the possible instabilities taking place there and their dynamics. The most active instabilities are the lower-hybrid-drift, kink, sausage and the tearing-mode. We have already discussed the results of investigations of most of these instabilities in the introduction section. However, as we mentioned, there are still some contradictions and open questions. Here is an overview of the most important problems that are addressed in this work.

Different instabilities in current sheets are, in some sense, competing with each other. But there are so many different conditions and free parameters in this problem, that it is not clear which of the possible instabilities is the most robust and efficient in triggering

magnetic reconnection. We analyse the basic physical processes which operate in thin current sheets and can lead to current sheet decay and magnetic reconnection.

Some investigations point at the important role of electrostatic effects in course of current sheet destabilization (e.g. (*Daughton, 1998; Silin et al., 2002*)) while others find a purely electromagnetic explanation of reconnection through the acceleration of electrons at the current sheet center by the electric field induced by the LHDI (e.g. (*Drake et al., 2003; Scholer et al., 2003*)). Are the electrostatic effects important there or can reconnection be consistently described as an electromagnetic phenomenon? And which role do the microscopic current-driven instabilities play in this process?

There is an important problem of interpretation of simulation results. Since simulations are forced to apply unrealistic parameters, like for example particle mass ratios, the translation of temporal and spatial scales to the realistic situation becomes non-trivial. Also, in order to avoid numerical instabilities one is forced to resolve Debye radius in kinetic simulations. In realistic magnetospheric parameters the ion gyroradius to Debye radius ratio is approximately 10^5 . Even with the most powerful now-a-days computer it is impossible to have a resolution of few Debye radii in a simulation box several ion gyroradii large in every dimension. One has to "tune" some physical parameters, like particle mass, temperature or the speed of light in order to comply with physical and technical constraints, to find a compromise between the computer resources and the physics. Thus, it is still not very clear if the instabilities observed in simulations are in fact weaker or stronger in realistic conditions.

Also, traditionally it was believed that the longest waves are also the most efficient ones, since the time of interaction of a wave with a particle is proportional to the wavelength. However, the a two-fluid current sheet linear stability theory of *Pritchett et al. (1996)* predicted that the wavenumber of the fastest-growing DKI mode changes as $kL_z \sim (m_i/m_e)^{1/2}/2$. Apparently, the fluid approach becomes non-applicable for high mass ratios, since the wavelength of the instability gets smaller than ion gyroradius. But this scaling law eventually pointed at short waves as the most linearly unstable. Later also *Büchner and Kuska (1998, 1999)* investigated the dependence of the DSI wavelength on the particle mass ratio by analytically solving the full eigenmode equations and by PIC-code simulations. They obtained a $kL_z \sim (m_i/m_e)^{1/4}$ dependence of the wavenumber of

the fastest-growing mode.

The question of whether kink or sausage mode should prevail in a current sheet and why is still a matter of discussion. For example, 3D PIC-code simulations of thin current sheets were carried out by *Büchner and Kuska (1996)*; *Zhu and Winglee (1996)* and *Pritchett et al. (1996)*. In the simulations of *Büchner and Kuska (1996)* the current-driven instability was a symmetric sausage-mode, while in the simulations of *Zhu and Winglee (1996)* the unstable mode was an asymmetric kink-mode. *Pritchett et al. (1996)* obtained both antisymmetric kink and symmetric sausage modes with almost identical wavelengths and growth rates. *Yoon et al. (1998)* considered the problem of the instability parity kink mode vs. sausage mode in the framework of a two-fluid eigenmode theory. They found that the symmetric sausage modes were growing faster than the asymmetric kink modes. But since they considered wavenumbers in the range $0.2 \leq kL_z \leq 2$ they could identify the fastest-growing mode only for $m_i/m_e = 10$. The growth rates increased for smaller wavelengths and larger particle mass ratios.

The interaction of microinstabilities like LHDI with global eigen modes of current sheets is also an important issue, not completely resolved at the moment. For example, LHDI was suggested by *Huba et al. (1978)* for enhancing reconnection by dissipation and anomalous resistivity. *Winske (1981)* investigated the LHDI by means of a 2D full particle-in-cell (PIC) code. He observed the onset of a global instability of the current sheet which was resonantly driven by ions. He suggested that this global instability could be a non-linear consequence of the LHDI penetrating towards the current sheet center. However, *Ozaki et al. (1996)*, who also used a 2D PIC-code, argued that the DKI was completely independent of the LHDI. To prove their point they performed a simulation where LHDI was artificially suppressed and they still obtained a kinking current sheet.

A possible non-linear mechanism for triggering a global current sheet instability by LHDI was suggested by *Hesse et al. (1998)* and *Lapenta et al. (2003)*. These authors observed that the LHDI creates a velocity shear with higher ion velocities at the center and lower velocities at the current sheet edges. They attributed this feature to the focusing of the faster ion orbits at the current sheet center by magnetic intrusions generated by the non-linear LHDI evolution. Thus, the mechanism of DKI generation might be similar to the one of a Kelvin-Helmholtz instability. *Daughton (2002)* also noticed that as a result of

LHDI the ion distribution function at the current sheet edges resembles a drift-Maxwell distribution with a stationary background population of scattered particles, which make $\sim 3\%$ of the peak density. He suggested, that the resulting ion-ion streaming could also contribute to the non-linear growth of DKI.

Another essential question is the coupling of current-aligned modes with the tearing-mode instability in the three-dimensional reconnection. Recently there appeared a theory that LHDI could help tearing-mode instability by thinning the current sheet and thus enhancing the linear growth rate. *Horiuchi and Sato (1999)* performed a series of PIC-code simulations of the DKI. They observed LHDI at the edges of the current sheet before a kink-mode started to grow. They found that during the LHDI activity the current sheet profile was compressed and suggested that the LHDI could non-linearly trigger a DKI by thinning the current sheet. This idea was further pursued by *Lapenta and Brackbill (2002)* using PIC-code and fluid simulations. They showed, that on average along the current direction LHDI moves a small population of particles further away from the current sheet edges, which alters the initial current density profile to a thinner, more peaked one.

Scholer et al. (2003) found in their PIC-simulations that the thinning of the current profile, discussed previously by *Horiuchi and Sato (1999)* and *Lapenta and Brackbill (2002)* occurred not due to the plasma compression, but due to the acceleration of electrons. The particle density and ion drift velocity profiles across the current sheet remained practically unchanged, while the electron current, initially small compared to ion one, increased almost by an order of magnitude at the current sheet center. *Scholer et al. (2003)* suggested that this was the result of the electron acceleration by "the inductive electric field excited by the lower hybrid drift instability". *Shinohara (2003)* proposed a multi-stage mechanism of this electron acceleration. The LHD waves at the edges of the sheet decrease the initial current. As a result, the magnetic field decreases everywhere throughout the current sheet. The change of the magnetic field, in turn, leads to electron acceleration at the current sheet center, where electrons are unmagnetized. *Shinohara (2003)* tried to diagnose this electric field in their simulations by producing the history plots of the electric fields experienced by the accelerated electrons, but they failed to demonstrate any convincing evidence of a DC electric field.

The results concerning the effects of magnetic guide field also seem quite contradic-

tory. On the one hand, *Scholer et al.* (2003) suggested a significant decrease of reconnection rate in the presence of $B_{y0} \sim B_0$ although without any significant changes of the reconnection pattern in the anti-parallel fields. On the other hand, *Pritchett and Coroniti* (2004) found that a significantly larger guide field is required to affect the reconnection rate mainly by suppressing the quadrupolar B_y pattern and the Hall currents. However, it should be mentioned that in the former case spontaneous reconnection was studied, while in the latter case it was triggered as in the GEM challenge approach. Also, according to the theory of *Galeev et al.* (1985); *Kuznetsova and Zelenyi* (1985, 1990a) there must be a family of obliquely propagating modes in current sheets with guide fields, which were not found in any simulations so far. We try to clarify this situation by our Vlasov-code simulations of spontaneous reconnection in the presence of guide fields.

Finally, in this work we address the problem of reconnection through non-symmetric current sheets at the magnetopause. Since magnetopause is highly variable and has a complicated structure, the process of reconnection through it is far more complicated compared to the symmetric current sheets. For example, *Quest and Coroniti* (1981) calculated analytically linear growth rates of tearing-mode instability at the day side magnetopause, based on typical parameters measured by ISEE 1 and 2 and assuming a simple 2D reconnection geometry. They found that the linear growth rate was very sensitive to the interplanetary magnetic field (IMF) orientation, current sheet thickness and plasma density. They showed, that due to the finite transition time of electrons through the reconnection region, which is smaller than the Landau resonance time, the eigen-functions and hence also the wave spectrum of the tearing modes are necessarily two-dimensional in the magnetopause plane. On this ground, the authors speculated that the reconnection at the magnetopause is intrinsically three-dimensional.

A recent review of *Russell* (2003) summarizes the problems concerning magnetopause reconnection. The community is presently divided into two groups. One of these supports the "component reconnection" where the magnetic fields at the opposite sides of the magnetopause are not necessarily anti-parallel (e.g. *Sonnerup* (1974)). The other group believes that reconnection occurs only in the regions where magnetic fields are exactly anti-parallel at the magnetopause (e.g. *Luhmann et al.* (1984)). The observations of FAST spacecraft suggest that reconnection at the magnetopause, indeed, occurs primar-

ily in the regions of antiparallel fields. However, there are also undisputed evidences of reconnection in the presence of guide field (e.g. *Kim et al. (2002)*).

Previous theoretical and simulational investigations, indeed, suggest that the guide-field B_y suppresses reconnection at the magnetopause. Thus, *Kuznetsova et al. (1994)* considered analytically magnetopause with anti-parallel asymptotic magnetic fields but with the finite B_y component at the maximum density gradient horizon. They found that strong magnetic field B_y component leads to sheared plasma flow in the magnetopause plane and stabilizes the magnetopause against the tearing-type modes. This conclusion was also confirmed by three-dimensional MHD simulations of *Lee et al. (2002)* and PIC simulations of *Swisdak et al. (2003)*. In particular, *Swisdak et al. (2003)* pointed that in the presence of guide-field component the reconnection region advects with electron diamagnetic drift velocity. In case of large relative ion-electron drift velocities this may prevent the formation of plasma outflows and reconnection is completely suppressed.

The reason for reconnection onset at the magnetopause also remains largely a mystery. *Otto et al. (1995)* carried out 2D MHD simulations with the aim to compare the consequences of reconnection and solar wind pressure pulse at the magnetopause for the flux-transfer events (FTE's). They found that the normal magnetic field amplitude is proportional to the pressure impulse and is typically smaller than in the case of magnetic reconnection. Also, reconnection leads to strong plasma acceleration that does not correlate with solar wind pressure pulses. Although both pressure impulses and reconnection transport impulse and energy, it is only reconnection that leads to plasma penetration through the magnetopause. However, under certain conditions pressure perturbations can trigger reconnection, e.g. by compressing the magnetopause thickness, which can explain certain correlation between FTE's and solar wind inhomogeneities.

Apart from the classical tearing-mode reconnection, microscopic instabilities like LHDI, are also very active at the magnetopause. In-situ observations onboard ISEE 1 and 2 (*Gurnett et al. (1979)*), Prognoz-7 and 8 (*Vaisberg et al. (1983)*), Equator-S (*Lucek et al. (2001)*), Polar (*Bale et al. (2002)*) and Cluster (*Vaivads et al. (2004)*) spacecraft reveal strong electrostatic noise near lower-hybrid frequency. Theoretical and numerical investigations of LHDI evolution at the magnetopause suggested that it might be quite grow up to a nonlinear regime and produce strong perturbations. For instance, *Gary and*

Sgro (1990) carried out PIC simulations of LHDI at the magnetopause. They considered a "flat" configuration with just one drift direction and one magnetic field component. After the rapid growth of the small-scale LHD instability, the wavelength increased, the perturbations coalesced and formed large "plateaus" and "inclusions". The authors suggested that these surface waves were qualitatively similar to the structures observed by ISEE 1 and 2 spacecraft at the magnetopause. Similarly, the quasi-linear calculations of *Shapiro et al.* (1994) revealed that LHDI should lead to a nonlinear "modulational" instability at the magnetopause. Recently *Shukla and Mamun* (2002) solved the system of nonlinear equations governing the dynamics of short wavelength LHD waves at the magnetopause-like boundaries in the so-called hybrid approach (ions - particles, electrons - fluid). For derivation of saturated LHD wave spectra mixing length hypothesis and mode coupling process were assumed. The equations have stationary solutions in a form of vortices. The instability is driven by electron density inhomogeneity and ion drift. For typical magnetopause parameters its growth rate is estimated as 4sec^{-1} . The vortices induced by LHDI effectively lead to particle trapping and diffusion through the magnetopause boundary.

Does the reconnection occur only in the regions of the anti-parallel magnetic fields, as suggested, e.g. by *Russell* (2003), or can it happen at any location, and what controls it? How can the microscopic instabilities and reconnection explain stochastic percolation or flux-transfer events (FTE's) through the magnetopause? As we have shown, some attempts were made to apply the classical 2D tearing-mode reconnection scenario directly to the non-symmetric magnetopause current sheets. But the structure of fields and currents at the magnetopause is different from the one-dimensional Harris-type model used in the investigations. Thus, we developed our own model of dynamic tangential magnetopause equilibrium with magnetic field and currents rotating through the magnetopause plane. We investigated the stability of this configuration by numerical Vlasov-code simulations.

Chapter 2

Thin current sheet models

2.1 Symmetric current sheets

For the investigation of current sheets by analytical methods and numerical simulations an appropriate analytical model of the equilibrium plasma and electromagnetic fields distribution is required. The most widely accepted model of a current sheet equilibrium is the so-called Harris model (*Harris*, 1962). The aim of this approach was to explain plasma confinement by magnetic fields.

This model is based on the assumption that both particle species have Maxwellian distribution functions:

$$f_j = \left(\frac{m_j}{2\pi T_j} \right)^{3/2} n_j \exp \left(-\frac{m_j(v_x^2 + (v_y - u_j)^2 + v_z^2)}{2T_j} \right), \quad (2.1)$$

where index $j = i, e$ corresponds to ions and electrons, respectively. From now on, we shall express particle temperature T in energy-units and omit the Boltzmann's constant κ . The classical Harris model considers the case of equal ion and electron temperatures $T_i = T_e = T$ and the equal, but oppositely directed, particle drift velocities $u_i = -u_e = V$. Using this form of distribution functions as a setup, the stationary Vlasov-Maxwell equations were solved:

$$\begin{aligned} \mathbf{v} \cdot \frac{\partial f_j}{\partial \mathbf{r}} + \frac{e_j}{m_j} (\mathbf{E} + \mathbf{v} \times \mathbf{B}) \cdot \frac{\partial f_j}{\partial \mathbf{v}} &= 0, \\ \nabla \cdot \mathbf{E} &= \frac{1}{\epsilon_0} \sum_j e_j \int f_j d^3v, \\ \nabla \times \mathbf{B} &= \mu_0 \sum_j e_j \int \mathbf{v} f_j d^3v. \end{aligned} \quad (2.2)$$

Harris considered an equilibrium, where f , \mathbf{E} and \mathbf{B} depend only on one coordinate, we shall call it z . In this configuration there are three constants of motion of charged particles, namely the full energy, and the momenta conjugate to x and y ,

$$\begin{aligned} W &= \frac{m_j}{2} (v_x^2 + v_y^2 + v_z^2) + e_j \phi(z), \\ p_x &= m_j v_x + e_j A_x(z), \\ p_y &= m_j v_y + e_j A_y(z). \end{aligned} \quad (2.3)$$

Further, it is assumed that \mathbf{E} and \mathbf{B} have only z - and x -components, respectively. Then, the vector potential \mathbf{A} must have only y -component. Using a special combination of constants of motion, *Harris* (1962) then expressed the velocity-dependence of the distribution functions and obtained a set of ordinary differential equations for electrostatic and vector potentials:

$$\begin{aligned} \frac{d^2 \phi}{dz^2} &= -\frac{ne}{\epsilon_0} \exp \left[\frac{eV A_y}{cT} \right] \left(\exp \left[-\frac{e\phi}{T} \right] - \exp \left[\frac{e\phi}{T} \right] \right), \\ \frac{d^2 A_y}{dz^2} &= -\mu_0 neV \exp \left[\frac{eV A_y}{cT} \right] \left(\exp \left[-\frac{e\phi}{T} \right] + \exp \left[\frac{e\phi}{T} \right] \right). \end{aligned} \quad (2.4)$$

The first equation (2.4) is satisfied by $\phi = 0$, which corresponds to charge-neutral plasma in the given frame of reference. The remaining equation (2.4) gives the exact solution of the problem:

$$A_y(z) = -\frac{2Tc}{eV} \log \cosh \left(\frac{zV}{c\lambda_D} \right), \quad (2.5)$$

where λ_D is the Debye length. From this relation it follows immediately:

$$\begin{aligned} B_x(z) &= \sqrt{4\mu_0 n_0 T} \tanh \left(\frac{zV}{c\lambda_D} \right), \\ n_i(z) = n_e(z) = n(z) &= n_0 \cosh^{-2} \left(\frac{zV}{c\lambda_D} \right), \end{aligned} \quad (2.6)$$

where n_0 is the maximum particle number density at the current sheet center. This classical result can be easily extrapolated to the situation of the unequal particle temperatures:

$$\begin{aligned} B_x(z) &= \sqrt{2\mu_0 n_0 (T_i + T_e)} \tanh \left(\frac{z}{L_z} \right), \\ n(z) &= n_0 \cosh^{-2} \left(\frac{z}{L_z} \right), \end{aligned} \quad (2.7)$$

where $L_z = \sqrt{\frac{T_i + T_e}{2\mu_0 n_0 e^2}}$ is the current sheet half-width. The plasma is charge-neutral in the frame where particles drift with mean velocities related as $u_i/u_e = -T_i/T_e$.

Another simple but very important extension of the Harris model is the so-called "guided-field" current sheet with a constant magnetic field component in the y-direction. In fact, one can see that an addition of a constant term $\frac{B_{y0}^2}{2\mu_0}$ to the pressure balance equation does not break the equilibrium:

$$\frac{B^2}{2\mu_0} + n(T_i + T_e) = \text{const.} \quad (2.8)$$

Recently there appeared also some non-Harris models of current sheets. For example, *Mottez* (2003) found a family of pure analytical solutions of non-linear Vlasov-Maxwell equations using expansion of generalized distribution function in infinite series and parameterizing it by the vector-potential. *Mottez* (2003) presented convincing examples of analytical solutions for well-known structures encountered in interplanetary and auroral plasmas. Interestingly enough, the contributions of different particle species to the total current are proportional to their temperatures, like in Harris model, although no special assumption is made for that. The main problem of this model is that it is mono-dimensional, i.e. there is only one dimension of density and magnetic field gradients and one (orthogonal) particle drift dimension. As such, this model is only suitable for description of current sheets with antiparallel magnetic fields.

Génot et al. (2003) applied the mono-dimensional model of *Mottez* (2003) for description of the so-called "bifurcated" current sheets, which were observed by Cluster, ISEE and Geotail spacecraft. Contrary to the Harris model, where current is concentrated at the current sheet center, here the current is located at the edges of the sheet near the density gradient maxima.

The main motivation for the current sheet model of *Yoon and Lui* (2004) was that in the classical Harris equilibrium the particle drift velocity ratio is equal to the particle temperature ratio $u_i/u_e = -T_i/T_e$. The authors introduced the particle drift velocity as a new independent parameter and solved analytically the Vlasov-Maxwell equations. However, this new degree of freedom was obtained through the loss of charge quasi-neutrality across the current sheet. This is, perhaps, one of the weak points in this model, because the charge separation occurs on the scales comparable to the current sheet thickness, i.e.

ion gyro-scales, while, for example, in the Earth magnetotail these scales are typically three orders of magnitude larger than Debye length. And since plasma tends to reach a quasi-neutral state on the distances larger than Debye radius such large non-neutral plasma structures seem rather artificial.

2.2 Magnetopause-like current sheets at the boundary between two plasmas

Further we discuss a model of an interface between plasmas with comparable but different densities, temperatures and magnetic fields. This model will be used to describe analytically the local equilibrium at the Earth magnetopause. Some examples of current sheet models of the magnetopause have been developed by *Lee and Kan (1979)*; *Kuznetsova and Roth (1995)*; *De Keyser and Roth (1997, 1998)*; *Mottez (2003)*. However, these models have serious drawbacks. First, the models of Lee and Kan, Kuznetsova and Roth and the later model of De Keyser and Roth (the so-called DKR-model) assume that the plasma on both sides of the magnetopause has equal temperatures, while from in-situ measurements it is known that, e.g., proton temperature changes across the magnetopause at least by a factor of 10 and sometimes by a factor of 100. Secondly, in both these models plasma is represented as a superposition of several particle populations, stationary and drifting, warm and cold, which further complicates the definition of temperature in such mixed plasmas. Lastly, all the above-mentioned models, except the one-dimensional model of *Mottez (2003)* are not analytical, i.e. the differential equations are integrated numerically, which makes these equilibria hardly applicable for computer simulations. The one-dimensional fully analytical model of *Mottez (2003)*, on the other hand, does not allow magnetic field rotation in the magnetopause plane. That is why we decided to build up our own model, which would correspond to the realistic magnetopause properties observed by numerous spacecraft missions (see e.g. *Gosling et al. (1982)*).

We shall focus here on a relatively simple model of tangential magnetopause (without initial normal magnetic field B_z) because this configuration prevents the flux transfer between magnetosphere and magnetosheath, and the aim of the present investigation is

to find out how it happens that such configurations eventually become "open". There are also other aspects, like for example shear plasma flows at the magnetopause, which might play an important role in destabilizing the equilibrium situation, but this will be a matter of a separate investigation.

Our aim is to construct a preferably simple analytical particle distribution function which would balance the expected profiles of plasma density and temperature and magnetic fields across some limited region. Strictly speaking, this is not necessarily a kinetic equilibrium situation, where particle kinetic energy and momenta are conserved. The reason is that, as such, magnetopause occurs at the regions where the solar wind (previously slowed down by the bow-shock) encounters an obstacle, a geomagnetic field. Thus, two magnetized plasmas are pressed against each other and a certain local balance appears. It is known from in-situ observations that this balance is very dynamical, the location and width of the magnetopause depend very strongly on the pressure and drift velocity of the solar wind, the magnetopause is practically in constant motion with velocities up to 100 km/s. This means that the equilibrium in the classical sense of particle constants of motion can hardly be applied there.

We consider a boundary between two stationary plasmas with different densities, temperatures, magnetic fields and plasma betas. We assume that away from the boundary region all plasma properties and magnetic fields asymptotically reach some constant levels. As input parameters we shall employ asymptotic values of plasma density, plasma betas ($\beta = \frac{2\mu_0 n(T_i + T_e)}{B^2}$) and total pressure $P_0 = n(T_i + T_e) + \frac{B^2}{2\mu_0}$. In order to reduce the number of unknowns in the problem we make several assumptions, like in the Harris approach. We presume, that ion and electron temperatures at both sides of the magnetopause are proportional, i.e. $T_i/T_e = const$ and both particle species have mean drift velocities related as $u_i/u_e = -T_i/T_e$. The velocity distribution functions of both species are assumed Maxwellian. So far this has been typical for all analytical solutions (see *Harris (1962)* and *Mottez (2003)*). We impose some model dependence for plasma density, temperature and the B_x magnetic field component and seek for the particle distribution functions that will keep such a structure at equilibrium. Let us assume that:

$$B_x(z) = B_{MSH} + \frac{B_{MSP} - B_{MSH}}{2} \left(1 + \tanh \left(\frac{z}{L_z} \right) \right),$$

$$\begin{aligned}
T(z) &= T_0 - T_1 \tanh\left(\frac{z}{L_z}\right), \\
n(z) &= n_0 + n_1 \tanh\left(\frac{z}{L_z}\right),
\end{aligned} \tag{2.9}$$

where L_z now denotes a typical thickness of the magnetopause region, B_{MSH} and B_{MSP} are the asymptotic values of the magnetic fields in the magnetosheath and magnetosphere, respectively. The corresponding asymptotic plasma density and temperature in magnetosheath and magnetosphere are $n_{MSH} = n_0 + n_1$, $T_{MSH} = T_0 - T_1$ and $n_{MSP} = n_0 - n_1$, $T_{MSP} = T_0 + T_1$. The values of T_0 and T_1 are calculated from the plasma betas and the total pressure. The in-situ measurements do not show that there are any typical values of plasma betas near magnetopause, but as a starting point we take $\beta_{MSH} = 0.6$, $\beta_{MSP} = 0.9 - 2.5$. In our description T is just a dimensionless function. The real particle species temperatures are obtained by multiplication of T by the nominal T_i and T_e , typically of the order of few keV . The asymptotic values of magnetic fields are then calculated to maintain the pressure balance at both sides of the interface.

Now, with the model functions for $\mathbf{B}(z)$, $n(z)$ and $T(z)$ we shall look for particle distribution functions in the form

$$f_j = \left(\frac{m_j}{2\pi T(z)T_j}\right)^{3/2} n(z) \exp\left(-\frac{m_j((v_x - u_{jx}(z))^2 + (v_y - u_{jy}(z))^2 + v_z^2)}{2T(z)T_j}\right) \tag{2.10}$$

($j = i, e$ for ions and electrons, respectively) which would also satisfy the pressure-balance equation

$$\frac{B^2}{2\mu_0} + n(T_i + T_e) = P_0 = const. \tag{2.11}$$

Using this form of distribution functions in the Maxwell equations and applying the assumption $u_{ix}/u_{ex} = u_{iy}/u_{ey} = -T_i/T_e$, we obtain a system of differential equations for the particle drift-velocities:

$$\begin{aligned}
v_{ix}(z) &= \frac{1}{\mu_0 e(1 + T_e/T_i)n(z)} \frac{\partial B_y}{\partial z}, \\
v_{iy}(z) &= -\frac{1}{\mu_0 e(1 + T_e/T_i)n(z)} \frac{\partial B_x}{\partial z},
\end{aligned} \tag{2.12}$$

where the analytical expression for $B_y(z)$ can be obtained by

$$B_y(z) = \sqrt{2\mu_0(P_0 - n(z)T(z)(T_i + T_e)) - B_x^2(z)}. \tag{2.13}$$

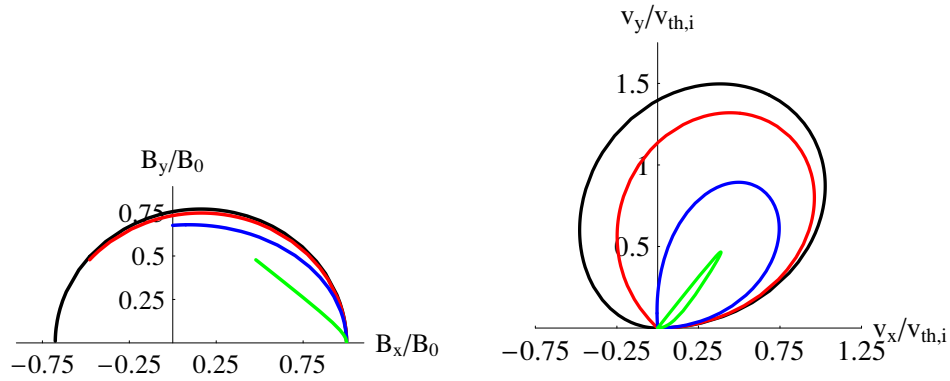


Figure 2.1: Examples of magnetic field (left) and ion drift velocity (right) hodographs across the model magnetopause current layer. The coloured curves correspond to the different rotation angles: black - $\Theta = \pi$, red - $\Theta = 3\pi/4$, blue - $\Theta = \pi/2$ and green - $\Theta = \pi/4$. All contours proceed from magnetosphere into magnetosheath in the counter-clockwise direction.

The main question concerning reconnection at the magnetopause is whether it occurs only at the regions of antiparallel field or there is also a possibility of "component reconnection". In other words, how does the stability of the boundary depend on the magnetic field full rotation angle Θ . In order to solve this question we introduce a finite asymptotic B_y component at the magnetosheath side and the magnetic field rotation angle is defined as $\Theta = \pi - \arctan(B_y/B_x)$, where the asymptotic ratio (B_y/B_x) in the magnetosheath is taken.

The resulting analytical expressions for the particle drift-velocities (as they are rather lengthy we shall skip the full expression here not to overload the text) give the solution of the problem. The advantages of this model are that it is fully analytical and can be directly ported in the numerical simulation and that it allows particle drifts and magnetic field rotation in the magnetopause plane. Three examples of hodographs of ion drift velocities and magnetic fields are shown in Figure (2.1). The black curves correspond to the antiparallel asymptotic magnetic fields (total rotation angle $\Theta = \pi$), the red curves show the $\Theta = 3\pi/4$ case, the blue curves show a case of perpendicular asymptotic fields ($\Theta = \pi/2$) and green curves - $\Theta = \pi/4$. Similar magnetic field hodographs with magnetic field rotation angles between $\pi/2$ and $3\pi/4$ were obtained experimentally during

the magnetopause crossings of ISEE 1 and ISEE 2 spacecraft (see e.g. Figures (8 - 12) in *Gosling et al.* (1982)).

In Figure (2.1) one immediately sees the consequence of the decreasing rotation angle of the magnetic field of a given magnitude - the total current (proportional to the linear integral of velocity hodograph) also decreases. Intuitively, this leads to stabilization of the magnetopause against Kelvin-Helmholtz instability (KHI) and other streaming-type instabilities due to weaker tangential velocity discontinuity. This argument seems to favour the scenario of anti-parallel reconnection at the magnetopause (see *Russell* (2003)).

Chapter 3

Linear theory of instabilities in thin Harris current sheets

3.1 Previous kinetic linear perturbation theories of thin current sheets

Dobrowolny (1968) suggested, that the main contribution to the instability is made by the electrons, meandering close to the neutral plane with perpendicular velocity $v_z \sim 0$. Thus, he assumed the particle orbits as straight lines and obtained very good agreement with more accurate but much more complicated analysis. To further simplify his analysis he also neglected the perturbations of the electrostatic potential and considering only the perturbation of the main component of vector potential A_y . *Dobrowolny* (1968) was probably the first to suggest, that the instability is driven by a resonant mechanism of the inverse Landau type.

The first discovery of cross-field propagating instabilities in current sheets should probably be attributed to *Yamanaka* (1978). He developed a linear stability theory of current sheets, considering only symmetric perturbations (sausage-type) of the current aligned vector-potential component and neglecting all other perturbations including electrostatic. In this approximation he found two modes, of which he considered only the electron mode as meaningful. It appeared that a linear instability can grow in thin current sheets with half-width $L_z \leq 0.9\rho_{0i}$. *Yamanaka* (1978) suggested that this unstable mode

would cause dissipation and consequently could trigger reconnection, e.g. in solar flares.

Lapenta and Brackbill (1997) further developed the linear kinetic theory of *Yamanaka* (1978). They considered the perturbations of all vector-potential components but still neglected the electrostatic perturbations. The particle trajectories near the center of the sheet were approximated by straight lines as by *Dobrowolny* (1968). They found that, in general, the cross-field propagating eigen-mode of the current sheet is not necessarily symmetric or antisymmetric about the central plane. Theoretical results were compared to implicit PIC-code simulations with particle mass ratios up to realistic. The simulations confirmed the growth rates predicted by linear dispersion relation. But the observed instability was asymmetric kink for small mass ratios and symmetric DSI for higher mass ratios. The growth rate of the instability slightly increased with the particle mass ratio.

Daughton (1998) reconsidered the linear instabilities of thin current sheets solving the Vlasov-Maxwell equations for the exact particle orbits instead of using the straight-line approach of *Dobrowolny* (1968). Contrary to previous analytical investigations, *Daughton* (1998) took into account also electrostatic perturbations. He found that the linear growth rate of the asymmetric DKI decreases with the particle mass ratio faster than the growth rate of the tearing mode instability, becoming negligible for the realistic mass ratio. *Daughton* (1998) considered only long-wavelength asymmetric kink modes with $kL_z \sim 0.5$. He confirmed his results by a two-fluid approach in the long-wavelength limit $kL_z < 0.5$ *Daughton* (1999a,b). This has put the entire previous discussion about current-aligned instabilities of current sheets under question.

3.2 Derivation of linear perturbation theory of thin Harris sheets

In our analytical and numerical investigations we shall use the following coordinate system: X – direction of magnetic field generated by the current flowing in Y-direction, Z – axis perpendicular to the current sheet plane (see Figure (1.1)). Throughout this chapter we shall denote all initial unperturbed quantities by 0-subscript and all perturbations by 1-subscript.

The unperturbed distribution function is the drift-Maxwellian

$$f_{0j} = \frac{n_j(z)}{(2\pi v_{th,j}^2)^{3/2}} \exp\left(-\frac{v_x^2 + (v_y - u_j)^2 + v_z^2}{2v_{th,j}^2}\right), \quad (3.1)$$

where index $j = i, e$ stands for ions and electrons, respectively; u_j are drift velocities of particles. Due to the charge-neutrality, the number density of both particle species is equal everywhere ($n_i = n_e = n$). The thermal velocity of particles is defined as $v_{th,j} = \sqrt{T_j/m_j}$, where T_j is temperature (which already includes Boltzmann's constant κ) and m_j is the mass of j -type particle species.

As shown by *Harris* (1962), if drift velocities of the drift-Maxwell distributions are related as $u_i/T_i = -u_e/T_e$, the zero-order electric field vanishes. This leads to a current sheet equilibrium with particle number density and magnetic field profiles:

$$\begin{aligned} n(z) &= n_0 \cosh^{-2}\left(\frac{z}{L_z}\right), \\ B_{0x}(z) &= B_0 \tanh\left(\frac{z}{L_z}\right). \end{aligned} \quad (3.2)$$

In such configuration plasma pressure inside the current sheet $\sum_j nT_j$ is exactly balanced by magnetic pressure $B_0^2/(2\mu_0)$ from outside the sheet.

In order to obtain the expression for the perturbation of distribution function we use the Vlasov equation for collisionless plasma

$$\frac{\partial f_j}{\partial t} + \mathbf{v} \cdot \frac{\partial f_j}{\partial \mathbf{r}} + \frac{e_j}{m_j} (\mathbf{E} + \mathbf{v} \times \mathbf{B}) \cdot \frac{\partial f_j}{\partial \mathbf{v}} = 0. \quad (3.3)$$

From Vlasov equation we get the linear perturbation of the distribution function at moment t by integration along the unperturbed trajectories

$$f_{1j}(t) = -\frac{e_j}{m_j} \int_{-\infty}^t \left((\mathbf{E}_1 + \mathbf{v} \times \mathbf{B}_1) \cdot \frac{\partial f_{0j}}{\partial \mathbf{v}} \right) dt'. \quad (3.4)$$

The perturbation of the distribution function generates perturbations of the initial plasma and current densities

$$\begin{aligned} \rho_{1j} &= e_j \int f_{1j} d^3v, \\ \mathbf{j}_{1j} &= e_j \int \mathbf{v} f_{1j} d^3v. \end{aligned} \quad (3.5)$$

We express electromagnetic fields by electrostatic and vector-potentials ϕ and \mathbf{A}

$$\begin{aligned}\mathbf{E}_1 &= -\nabla\phi_1 - \frac{\partial\mathbf{A}_1}{\partial t}, \\ \mathbf{B}_1 &= \nabla \times \mathbf{A}_1.\end{aligned}\tag{3.6}$$

Thus we arrive at a system of D'Alambert equations for potential perturbations

$$\begin{aligned}\Delta\phi_1 - \frac{1}{c^2}\frac{\partial^2\phi_1}{\partial t^2} &= -\frac{\rho_1}{\epsilon_0}, \\ \Delta\mathbf{A}_1 - \frac{1}{c^2}\frac{\partial^2\mathbf{A}_1}{\partial t^2} &= -\mu_0\mathbf{j}_1.\end{aligned}\tag{3.7}$$

We combine the oscillation frequency and the wave damping/growth rate in a complex frequency $\omega = \Omega + i\gamma$ and consider waves propagating in the current sheet plane: $\mathbf{k} = \{k_x, k_y, 0\}$, so that $\mathbf{k} \cdot \mathbf{r} = k_x x + k_y y$. We shall denote the angle between the wave propagation direction and the X-axis as θ . Then, in the polar coordinates we can write $\mathbf{k} = \{k \cos \theta, k \sin \theta, 0\}$.

So far we have made no serious simplifying assumptions, except linearizing the Vlasov equation. There we assumed that the perturbation of the distribution function is small and its derivative is small too. In order to further simplify the analysis we now make some approximations. First, we neglect the displacement current, since the phase velocities of the instabilities which we investigate are small compared to the speed of light

$$\frac{\omega^2}{k^2 c^2} \ll 1.\tag{3.8}$$

Second, it can be shown that in our long wavelength approximation $kL_z \ll 1$ (or $\partial/\partial z \rightarrow 0$) the equation for A_z is decoupled from equations for A_x , A_y and ϕ .

After substitution of expressions for electromagnetic fields into Equation (3.4)

$$f_{1j} = \frac{e_j f_{0j}}{m_j v_{th,j}^2} \int_{-\infty}^t \left(-\nabla\phi_1 - \frac{\partial\mathbf{A}_1}{\partial t} + \mathbf{v} \times (\nabla \times \mathbf{A}_1) \right) \cdot \mathbf{v} dt'.\tag{3.9}$$

Some reordering should be made in order to simplify the equation (3.9). Taking the double vector product, $\mathbf{v} \times (\nabla \times \mathbf{A}_1) = (\nabla\mathbf{A}_1) \cdot \mathbf{v} - (\mathbf{v} \cdot \nabla)\mathbf{A}_1$, and using the fact that

$$\frac{d}{dt} = \frac{\partial}{\partial t} + \mathbf{v} \cdot \nabla,\tag{3.10}$$

we separate the full derivatives. We investigate the stability of the current sheet against perturbations of the following wave form:

$$\phi_1(x, y, z, t) = \phi_1(z) \exp\{-i\omega t + i\mathbf{k} \cdot \mathbf{r}\},$$

$$\mathbf{A}_1(x, y, z, t) = \mathbf{A}_1(z) \exp\{-i\omega t + i\mathbf{k} \cdot \mathbf{r}\}. \quad (3.11)$$

Hence, applying the Fourier transformations

$$\begin{aligned} \frac{\partial \mathbf{A}_1}{\partial t} &= -i\omega \mathbf{A}_1, \\ \nabla \cdot \mathbf{A}_1 &= i\mathbf{k} \cdot \mathbf{A}_1, \end{aligned}$$

we can now partially take the integral:

$$f_{1j} = \frac{e_j f_{0j}}{m_j v_{th,j}^2} \left(A_{1y} u_j - \phi_1 + i(\omega - k_y u_j) \int_{-\infty}^t (\mathbf{A}_1 \mathbf{v} - \phi_1) dt' \right). \quad (3.12)$$

Now, if we confine our theory to modes of even symmetry, for which $\partial A_1 / \partial z = 0$ at $z = 0$, we can use the so-called *const A* and *const ϕ* approximation. Thus, variations of potentials are small in the center of the sheet on the scale of particle orbits and we can take A and ϕ out of integration over time, which would simplify our analysis. This is possible only for even modes and that is why we are not considering odd kink-type modes here, which were considered in detail by *Daughton* (1998).

We shall use straight-line orbit approximation. Argumentation of this approach was given by *Dobrowolny* (1968) and discussed in detail by *Lapenta and Brackbill* (1997). In fact, by integration over time, we average the real orbit over fast nonlinear oscillations around the neutral plane. Because average magnetic field \mathbf{B} , in which particles are bouncing is zero, after averaging one arrives at a situation, that although particles are oscillating around $z = 0$ plane, the projection of their motion in $z = 0$ plane occurs as if magnetic field is absent and particles move along straight lines, in analogy to the guiding-center motion.

For unstable modes, i.e. for $\gamma > 0$, the perturbation grows with time as $\exp(\gamma t)$ and the integral over t' converges:

$$\int_{-\infty}^t (\mathbf{A}_1 \mathbf{v} - \phi_1) dt' = \frac{\mathbf{A}_1 \mathbf{v} - \phi_1}{-i\omega + i\mathbf{k}\mathbf{v}}. \quad (3.13)$$

Thus, we can write the system of equations (3.7) in the form

$$\begin{aligned} \Delta A_{1x} &= - \sum_j \frac{2\omega_{pj}^2}{v_{th,j}^2 c^2} \int \left(A_{1y} u_j - \phi_1 - (\omega - k_y u_j) \frac{\mathbf{A}_1 \mathbf{v} - \phi_1}{\omega - \mathbf{k}\mathbf{v}} \right) v_x f_{0j} d^3 v, \\ \Delta A_{1y} &= - \sum_j \frac{2\omega_{pj}^2}{v_{th,j}^2 c^2} \int \left(A_{1y} u_j - \phi_1 - (\omega - k_y u_j) \frac{\mathbf{A}_1 \mathbf{v} - \phi_1}{\omega - \mathbf{k}\mathbf{v}} \right) v_y f_{0j} d^3 v, \end{aligned} \quad (3.14)$$

$$\Delta \phi_1 = - \sum_j \frac{2\omega_{pj}^2}{v_{th,j}^2} \int \left(A_{1y} u_j - \phi_1 - (\omega - k_y u_j) \frac{\mathbf{A}_1 \cdot \mathbf{v} - \phi_1}{\omega - \mathbf{k} \cdot \mathbf{v}} \right) f_{0j} d^3 v,$$

where we introduce the plasma frequency $\omega_{pj}^2 = n_j e_j^2 / (m_j \epsilon_0)$, $j = i, e$ for ions and electrons, respectively.

In system of equations (3.14) all functions under the integral, which are antisymmetric in v_x will give 0 after integration. Besides, one should notice that v_z is not included in the $\mathbf{k} \cdot \mathbf{v}$ expression, since \mathbf{k} lies in the X-Y plane. One could show that, due to symmetry properties of v_z , if term with A_{1z} is included formally in the expression $\mathbf{A}_1 \cdot \mathbf{v}$ in the formulas for current and density perturbations j_{1x} , j_{1y} and ρ_1

$$\begin{aligned} \int \frac{A_{1z} v_z}{\omega - \mathbf{k} \cdot \mathbf{v}} v_x f_{0j} d^3 v &= 0, \\ \int \frac{A_{1z} v_z}{\omega - \mathbf{k} \cdot \mathbf{v}} v_y f_{0j} d^3 v &= 0, \\ \int \frac{A_{1z} v_z}{\omega - \mathbf{k} \cdot \mathbf{v}} f_{0j} d^3 v &= 0. \end{aligned} \quad (3.15)$$

Thus, our system (3.14) is decoupled from perturbations of A_{1z} . So, implicitly the Lorentz gauge condition that we use can be written as:

$$ik_x A_{1x} + ik_y A_{1y} + \frac{\partial A_{1z}}{\partial z} - \frac{i\omega}{c^2} \phi_1 = 0. \quad (3.16)$$

Although A_{1z} is not necessarily 0 it doesn't play any significant role for the instabilities propagating in the current sheet plane. Indeed, wave and particle motion along the z-axis which could generate A_{1z} is strongly suppressed by the current sheet symmetry. That is why in our further derivations we shall omit A_{1z} and describe the electromagnetic part of instability using with A_{1x} and A_{1y} components. However, the A_{1z} can be always derived from the gauge relation (3.16).

From the system of equations (3.11) we obtain for the Laplace operator $\Delta = d^2/dz^2 - k^2$. Thus, we get

$$\begin{aligned} \frac{d^2 A_{1x}}{dz^2} - k^2 A_{1x} &= \\ \sum_j \frac{2\omega_{pj}^2}{v_{th,j}^2 c^2} \{ (\omega - k_y u_j) \int \frac{A_x v_x + A_y v_y - \phi_1}{\omega - k_x v_x - k_y v_y} v_x f_{0j} dv_x dv_y \}, \\ \frac{d^2 A_{1y}}{dz^2} - k^2 A_{1y} &= \\ - \sum_j \frac{2\omega_{pj}^2}{v_{th,j}^2 c^2} \{ A_y u_j^2 - \phi_1 u_j \\ - (\omega - k_y u_j) \int \frac{A_x v_x + A_y v_y - \phi_1}{\omega - k_x v_x - k_y v_y} v_y f_{0j} dv_x dv_y \}, \end{aligned} \quad (3.17)$$

$$\begin{aligned} \frac{d^2 \phi_1}{dz^2} - k^2 \phi_1 = & \\ & - \sum_j \frac{2\omega_{pj}^2}{v_{th,j}^2} \{A_y u_j - \phi_1 \\ & - (\omega - k_y u_j) \int \frac{A_x v_x + A_y v_y - \phi_1}{\omega - k_x v_x - k_y v_y} f_{0j} dv_x dv_y \}. \end{aligned}$$

For convenience in further computations we introduce dimensionless variables $q = kL_z$, $\xi_j = \omega - k_y u_j / kv_{th,j}$, $U_j = u_j / v_{th,j}$ and express the integrals over v_x, v_y in terms of plasma dispersion function:

$$Z_n(\xi) = \frac{1}{\sqrt{\pi}} \int_{-\infty}^{+\infty} \frac{t^n e^{-t^2}}{t - \xi} dt. \quad (3.18)$$

Following the approach of *Bulanov and Syrovatskyi* (1974), we consider the current sheets as infinitely thin. Then, the equations for potentials have the form

$$\frac{d^2 A}{dz^2} - k^2 A = U \delta(z), \quad (3.19)$$

where we use A for ϕ , A_{1x} , A_{1y} and U for the right-hand expressions from Equations (3.17).

The solutions of Equation (3.19) have the form

$$A(z) = \frac{U}{2} e^{-k|z|}. \quad (3.20)$$

The perturbations are limited to a thin region across the neutral sheet. Then, if we integrate Equation (3.19) in the layer of thickness 2δ along Z-axis, we get

$$\int_{-\delta}^{+\delta} \frac{d^2 A}{dz^2} dz - k^2 \int_{-\delta}^{+\delta} A dz = \int_{-\delta}^{+\delta} U \delta(z) dz. \quad (3.21)$$

It is easy to see, that with δ tending to zero the second integral in the left-hand part of Equation (3.21) vanishes. Thus, in the limit of infinitely thin current sheet we get

$$A'_+ - A'_- - U(0) = 0. \quad (3.22)$$

Here we used A'_+ and A'_- notations to indicate derivatives as $z \rightarrow 0$ from above and from below. Linking solutions of the form (3.20) at the neutral plane gives us

$$A'_+ - A'_- = -2kA(0). \quad (3.23)$$

This allows us to reduce the problem of coupled differential equations (3.14) to much more simple algebraic system and write the system of equations in the following form

$$2qA_{1x} =$$

$$\begin{aligned} & \sum_j \frac{\omega_{pj}^2 L_z^2}{c^2} \{ A_{1x} \xi_j (Z_0 \sin^2 \theta + 2Z_2 \cos^2 \theta) \\ & + A_{1y} \xi_j (2U_j Z_1 \cos \theta - (Z_0 - 2Z_2) \cos \theta \sin \theta) \\ & - \phi_1 \frac{2\xi_j Z_1 \cos \theta}{v_{th,j}} \}, \end{aligned}$$

$$\begin{aligned} 2q A_{1y} = & \\ & \sum_j \frac{\omega_{pj}^2 L_z^2}{c^2} \{ A_{1x} \xi_j (2U_j Z_1 \cos \theta - (Z_0 - 2Z_2) \cos \theta \sin \theta) \\ & + A_{1y} (\xi_j Z_0 \cos^2 \theta + 2\xi_j Z_2 \sin^2 \theta + 4U_j Z_2 \sin \theta + 2U_j^2 Z_1) \\ & - \phi_1 (2U_j + 2\xi_j (U_j Z_0 + Z_1 \sin \theta)) \}, \end{aligned} \quad (3.24)$$

$$\begin{aligned} 2q \phi_1 = & \\ & \sum_j \frac{\omega_{pj}^2 L_z^2}{v_{th,j}^2} \{ A_{1x} 2\xi_j Z_1 \cos \theta \\ & + A_{1y} (2\xi_j Z_1 \sin \theta + 2U_j Z_1) \\ & - \phi_1 \frac{2Z_1}{v_{th,j}} \}. \end{aligned}$$

In fact, one could easily verify that this solution represents the $q = kL \ll 1$ expansion of the standard solutions, expressed before via Legendre polynomials $P_1^q(z/L_z)$ (see *Dobrowolny* (1968) and *Galeev and Zelenyi* (1976)).

To make the formulas more compact we used Z_n instead of $Z_n(\xi_j)$. After rearranging the expressions in (3.24) we obtain a system of algebraic equations for perturbations of potentials:

$$\begin{aligned} \alpha_{11} A_{1x} + \alpha_{12} A_{1y} + \alpha_{13} \phi_1 &= 0, \\ \alpha_{21} A_{1x} + \alpha_{22} A_{1y} + \alpha_{23} \phi_1 &= 0, \\ \alpha_{31} A_{1x} + \alpha_{32} A_{1y} + \alpha_{33} \phi_1 &= 0. \end{aligned} \quad (3.25)$$

The coefficients of the matrix in Equations (3.25) are:

$$\begin{aligned} \alpha_{11} &= 2q - \sum_j \frac{\omega_{pj}^2 L_z^2}{c^2} \xi_j (Z_0(\xi_j) \sin^2 \theta + 2Z_2(\xi_j) \cos^2 \theta), \\ \alpha_{12} &= \sum_j \frac{\omega_{pj}^2 L_z^2}{c^2} \xi_j \{ (Z_0(\xi_j) - 2Z_2(\xi_j)) \sin \theta \cos \theta \\ & - 2U_j Z_2(\xi_j) \cos \theta \}, \end{aligned}$$

$$\begin{aligned}
\alpha_{13} &= \sum_j \frac{2\omega_{pj}^2 L_z^2}{c^2 v_{th,j}} Z_2(\xi_j) \cos \theta, \\
\alpha_{21} &= \sum_j \frac{\omega_{pj}^2 L_z^2}{c^2} \xi_j \{ (Z_0(\xi_j) - 2Z_2(\xi_j)) \sin \theta \cos \theta \\
&\quad - 2U_j Z_2(\xi_j) \cos \theta \}, \\
\alpha_{22} &= 2q - \sum_j \frac{\omega_{pj}^2 L_z^2}{c^2} \{ \xi_j (Z_0(\xi_j) \cos^2 \theta + 2Z_2(\xi_j) \sin^2 \theta) \\
&\quad + 4U_j Z_2(\xi_j) \sin \theta + 2U_j^2 Z_1(\xi_j) \}, \\
\alpha_{23} &= \sum_j \frac{2\omega_{pj}^2 L_z^2}{c^2 v_{th,j}} (U_j Z_1(\xi_j) + Z_2(\xi_j) \sin \theta), \\
\alpha_{31} &= - \sum_j \frac{2\omega_{pj}^2 L_z^2}{v_{th,j}} Z_2(\xi_j) \cos \theta, \\
\alpha_{32} &= - \sum_j \frac{2\omega_{pj}^2 L_z^2}{v_{th,j}} (U_j Z_1(\xi_j) + Z_2(\xi_j) \sin \theta), \\
\alpha_{33} &= 2q + \sum_j \frac{2\omega_{pj}^2 L_z^2}{v_{th,j}^2} Z_1(\xi_j).
\end{aligned} \tag{3.26}$$

Finally, we set real and imaginary parts of determinant of this system of equations to zero and obtain the dispersion relation:

$$\begin{aligned}
\Re[\det[\alpha]] &= 0, \\
\Im[\det[\alpha]] &= 0.
\end{aligned} \tag{3.27}$$

In order to consider separately the action of electromagnetic and electrostatic modes we also looked for solutions of the reduced matrix. Thus, to exclude the perturbations of the electrostatic potential, instead of determinant of 3×3 matrix we used its 2×2 minor

$$\begin{aligned}
\Re[\alpha_{11}\alpha_{22} - \alpha_{12}\alpha_{21}] &= 0, \\
\Im[\alpha_{11}\alpha_{22} - \alpha_{12}\alpha_{21}] &= 0.
\end{aligned} \tag{3.28}$$

3.3 Numerical solutions of dispersion relation

In our case the dispersion relation (3.27) is a system of non-linear non-algebraic equations in Ω , γ , k and θ coordinates. The region of interest for present investigation extends from 0 to approximately Ω_{0i} (ion gyro-frequency) in Ω and γ , from 0 to $0.5/L_z$ in wavenumber

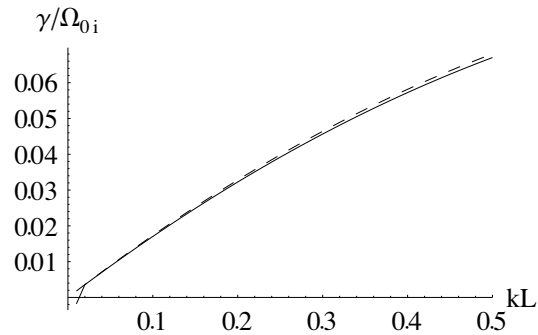


Figure 3.1: Dispersion relation for the tearing mode. Solid curve - including the influence of electrostatic potential, dashed curve - with ϕ perturbations neglected.

k and from 0 to $\pi/2$ in θ . We investigate the dependence of dispersion relation solutions on such parameters as k , θ , ρ_{0i}/L_z . For comparison with numerical simulation results we also find solutions of the dispersion relation for artificial ion-electron mass ratios.

There are no unique methods for solving systems of non-linear non-algebraic (in respect to wavenumber and complex frequency) equations. Since we have a system of only two equations (3.27) and the number of variables is four, the only way out is to fix two variables, according to some assumptions, and vary the other two. We applied the following procedure to find solutions: the real and imaginary parts of the dispersion relation were plotted in $\gamma - \Omega$ coordinates and the region where they both turned to 0 was localized. Further, to find an exact solution, the Newton - Raphson method (see e.g. *Press et al.* (1988)) was applied in the vicinity of this point.

From calculation point of view, the simplest case is the tearing mode, because then $\theta = 0$ and $\Omega = 0$. Figure (3.1) shows the dispersion of the tearing modes with and without taking electrostatic perturbations into account.

Figure (3.2) shows the dependence of the tearing-mode growth rate on the current sheet thickness. Logically, thinner current sheets are less stable.

The pairs of curves presented in Figures (3.1,3.2) are almost identical. This verifies the theoretical assumption of *Dobrowolny* (1968) that the tearing-mode instability does not depend on electrostatic potential perturbations and contradicts the linear theory and PIC-simulations of *Hoshino* (1987). The same results are obtained if only one perturbed component A_{1y} is considered.

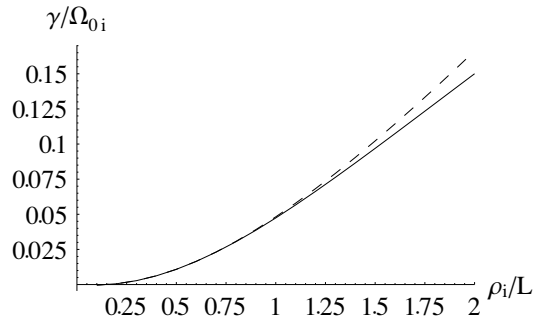


Figure 3.2: Tearing mode growth rate for different sheet thickness. Solid curve - including the perturbations of electrostatic potential, dashed curve - ϕ neglected.

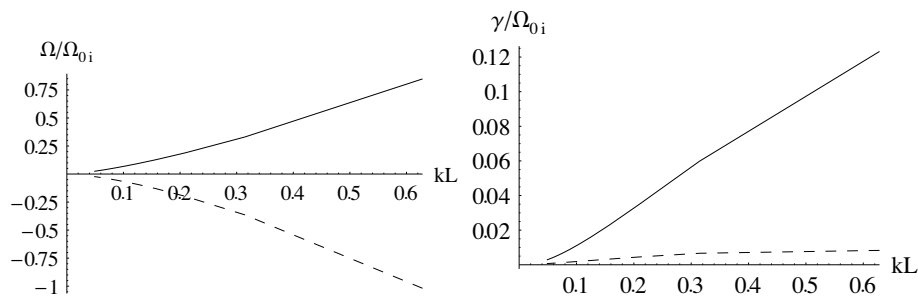


Figure 3.3: Dispersion relation for sausage quasi-modes (left panel - real frequencies, right - growth rates) when perturbations of ϕ are suppressed. Solid curve - ion quasi-mode, dashed curve - electron quasi-mode.

Quite different situation appears with the mode propagating in the current direction. Since our theory was developed only for symmetric perturbations, this mode corresponds to the sausage-type instability.

When the electrostatic potential is excluded from the consideration, two distinct branches of solutions are found (we shall further call them quasi- solutions or quasi-modes). One corresponds to electron, the other to ion drift. Figure (3.3) shows real frequencies and growth rates for ion (solid line) and electron (dashed line) quasi-modes. One can see that for electron quasi-mode the real frequency is negative, which means that the wave propagates in the direction of the electron drift. This mode was considered in detail by *Yamanaka (1978)*.

From the ratio of electron and ion growth rates in Figure (3.3) it is clear, that the ion

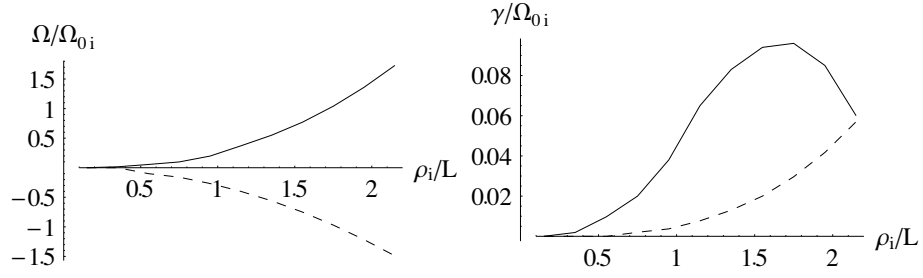


Figure 3.4: Dependence of sausage quasi-mode frequencies (left panel) and growth rates (right panel) on the current sheet thickness. Solid curve - ion quasi-mode, dashed curve - electron quasi-mode.

quasi-mode should dominate for all wavelengths, contrary to assumption of *Yamanaka* (1978). The dependence of wave properties on the sheet thickness is demonstrated in Figure (3.4).

It is difficult to draw direct comparison of these results with those of *Lapenta and Brackbill* (1997), because these authors did not discuss real frequencies or wavelengths of the modes, for which the growth rates were drawn (for kL_z range 0.1 to 0.5 the absolute values of growth rates differ by an order of magnitude). But the general dependence of instability growth rate on the sheet width in our case is the same as reported by them (for the range considered here). This contradicts the main result of *Yamanaka* (1978) that the wave becomes unstable only for current sheets with $L_z \leq 0.9\rho_{0i}$. When the electrostatic potential perturbations are taken into consideration both branches of solution disappear. They reappear only if the particle mass ratio m_i/m_e is artificially decreased to values of the order of 10.

In order to trace the transition from tearing to sausage mode, we investigated the dependence of dispersion relation solutions on the propagation angle θ . Figure (3.5) shows several branches of solutions for current sheet width $L_z = \rho_{0i}$ and wave number $k = 2\pi/20L_z$. The left-hand panel demonstrates the real frequencies, the right-hand one shows the growth rates. The thick solid curve corresponds to electron mode which is obtained with electrostatic potential taken into consideration. The thin dashed line shows the properties of the electron quasi-mode when ϕ perturbations are absent. The thin solid line shows the ion quasi-mode. The latter appears solely when the perturbations of ϕ are

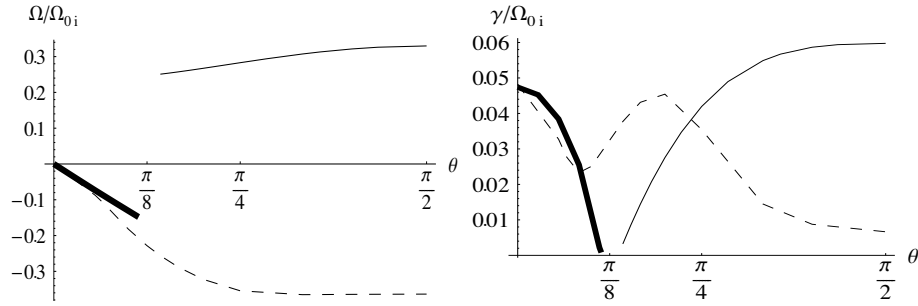


Figure 3.5: Dependence of dispersion relation solution (left panel - Ω , right panel - γ) on the propagation angle θ . Thick solid curve - electron mode obtained when electrostatic perturbations are included, thin dashed curve and thin solid curve - electron and ion quasi-modes with perturbations of ϕ neglected, respectively.

neglected.

It follows, that the perturbations of electrostatic potential stabilize the modes, which propagate at angles larger than approximately $\pi/8$ to the magnetic field direction. Thus, in accordance with the previous subsection we see, that in the general case of linear perturbation theory for long wavelengths, there are no sausage-type solutions when perturbations of ϕ are taken into account. This is in perfect agreement with findings of *Daughton* (1999a) (in particular, see Figure 8 on page 1337 therein).

The dependence of oblique modes with $k = 2\pi/20L_z$ on the sheet thickness is demonstrated in Figure (3.6). All solutions were obtained with full dispersion relation Equation (3.27). As expected, thinner current sheets are found to be more unstable against tearing-type instabilities. But the oblique modes are strongly stabilized with the increasing propagation angle.

Perhaps, the main result of this linear perturbation theory is reflected in Figure (3.5). Namely, this diagram shows that the linear long-wavelength ion and electron oblique modes (including the cross-field propagating sausage mode) found in previous linear theories are artifacts of neglecting the electrostatic part of perturbations. As soon as the problem is treated with the full contribution of the electrostatic potential perturbations, these modes vanish, leaving only the aperiodic tearing-mode instability. A similar result has been previously obtained by *Daughton* (1998) in a more sophisticated investi-

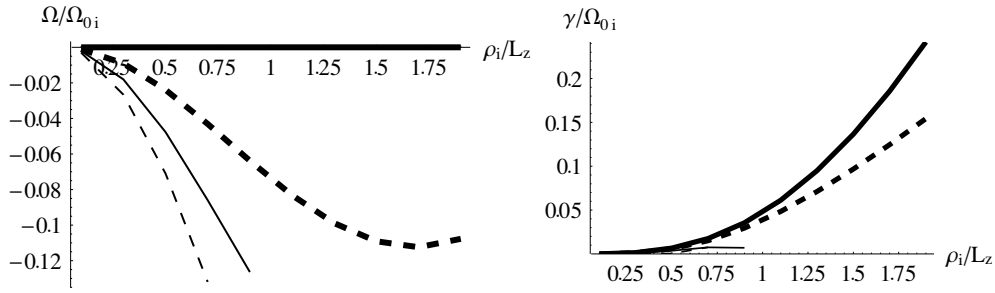


Figure 3.6: Dependence of dispersion relation solutions (left panel - Ω , right panel - γ) on the sheet thickness for several propagation angles θ . Thick solid curve - tearing mode ($\theta = 0$), thick dashed curve - $\theta = \pi/18$, thin solid curve - $\theta = \pi/9$, thin dashed curve - $\theta = \pi/6$.

gations of the long-wavelength anti-symmetric kink-mode instability of current sheets. This finding puts under question the observed kink and sausage instabilities obtained in numerical simulations. As was shown by *Silin et al.* (2002), for artificial particle mass ratio $m_i/m_e \sim 10$ the instability still exists in all regimes, while for higher mass ratios $m_i/m_e \sim 100$ all the oblique linear modes are suppressed. However, it turns out that in different simulations the kink and sausage modes still exist for high mass ratios, up to realistic (see e.g. *Ozaki et al.* (1996); *Büchner and Kuska* (1996); *Lapenta and Brackbill* (1997, 2002); *Daughton* (2002)). There are at least two plausible explanations for this fact. One is that the long-wavelength approximation $kL_z < 1$ usually adopted in the linear theories does not correspond to the fastest-growing modes. The other is that there are some processes which can trigger the current instabilities nonlinearly. To name just a few - Kelvin-Helmholtz instability (KHI), ion-ion kink instability, lower-hybrid-drift instability (LHDI). In order to consider the nonlinear evolution of current sheets we developed the numerical code which directly integrates Vlasov-Maxwell system of equations. The results of this investigation are discussed in the following chapters.

Chapter 4

Vlasov-code simulations

4.1 Description of the numerical code

The main feature which distinguishes the Vlasov-code simulations from other numerical methods of plasma simulation, such as magneto-hydro-dynamic (MHD), hybrid and particle-in-cell (PIC) codes, is that plasma is represented by particle distribution functions. For comparison, in MHD codes plasma is considered as fluid, in PIC-codes as an ensemble of so-called super-particles, in hybrid codes - ions are represented by super-particles and electrons by fluid. MHD-codes allow diagnostics only of the mean local velocity of plasma. In PIC-codes, the number of super-particles per cell usually does not exceed 100. In case of inhomogeneous plasmas, the number of particles in low-density regions even turns to zero. Thus, information about particle distribution in the velocity space is available only in dense plasma regions. But even there the number of particles per each velocity dimension is only $100^{1/3} \approx 4$.

The advantage of the Vlasov approach is the detailed information about the distribution of particles in the velocity space. This allows investigations which cannot be carried out in MHD or PIC approaches, e.g. of collective kinetic effects, like resonant wave-particle interactions, pitch-angle scattering, etc. The distribution functions have to be sampled by at least 15 - 20 points in every velocity dimension. Besides, the local plasma density changes only the amplitude of the distribution and does not affect the velocity range coverage. Theoretically, such simulation corresponds to using a PIC code with

3400 - 8000 super-particles in every cell.

There are, however, limits of application of Vlasov-code simulations. First, the classical Vlasov equation describes only collisionless plasmas, i.e. very hot and rarefied matter. It cannot be directly applied to simulations of laboratory and stellar plasmas, where collisions are important. Also, the Vlasov approach is based on consideration of a limited volume in velocity space. Thus, high energy tails of distribution function usually cannot be taken into consideration. This is, however, not of great concern since the classical Vlasov equation is valid only for non-relativistic interactions. In order to describe very hot plasmas or energetic tails of particle distributions one has to use generalized relativistic kinetic equations. Thus, the present work is only limited to the non-relativistic energy-range, which is, however, sufficient for considering most processes in magnetospheric plasmas where relativistic particles are rare and do not produce significant influence.

An important question is the normalization of the code and the selection of the consistent set of physical and technical parameters for each simulation. We shall briefly list the physical and technical constraints for a typical kinetic simulation and discuss the consequent parametric relations between the input parameters.

- Courant-Friedrichs-Levy condition for resolving the electromagnetic wave propagation: $\Delta_x > cdt$

For all leap-frog numerical schemes, except iterative ones, the information at every time step is updated only using the information at the adjacent grid points. That is why, if the time step is so large that the electromagnetic waves propagate the distance longer than one space grid, the usual finite-difference numerical scheme produces a non-physical result.

- Resolution of electrostatic interactions: $\Delta_x \leq 3\lambda_{De}$

It has been shown by *Birdsall and Langdon* (1991) that in case the grid space contains more than approximately 3 Debye radii a strong numerical instability arises which resembles a resonant interaction of particle beam with electrostatic perturbations.

- Fitting of at least 3 LHD wavelengths in the simulation box: $L_y \sim 3\lambda_{LHD}$

Since LHDI is the fastest instability, which is expected to grow in our simulation

we have to resolve its wavelength. And since periodic boundary conditions allow only an integer number of wavelengths in the simulation box, there is a danger of artificial modifying the wavelength by introducing a box length slightly smaller or slightly larger than the natural wavelength. Thus, it is important to have as many wave periods in the box as technically possible, and 3 is a kind of compromise.

- Exclusion of relativistic particles: $c > 3v_{th,e}$

Since the classical Vlasov equation does not describe relativistic particle dynamics, one has to make sure that the limits of the velocity space are fixed at the appropriate values. Usually three thermal velocities are sufficient to confine the Maxwellian distribution without cutting away too many energetic particles.

- Charge-separation condition: $\omega_{pe} \geq \Omega_{C,e}$

This condition has been shown to play essential role during the charge separation processes. Besides, this situation is also typical for the magnetospheric plasmas. That is why it is important to comply with this relation when investigating electrostatic effects in the magnetospheric plasmas.

For our investigations we have to consider spatial scales of the order of several ion gyroradii ρ_{0i} on temporal scales of the order of several ion gyroperiod Ω_{0i}^{-1} . These are two basic normalizing units in our system. The unit velocity is the ion thermal velocity $v_{th,i} = (T_i/m_i)^{1/2} = \rho_{0i}\Omega_{0i}$. In order to fully determine the simulated plasma regime we input five dimensional values, namely the speed of light c , the elementary charge e , a mass of proton m_i , the maximum plasma density n_0 and the ion temperature T_i . Additionally, we have to define some dimensionless parameters: particle mass and temperature ratios m_i/m_e and T_i/T_e , current sheet half-width and simulation-box sizes in terms of ion gyroradii L_z/ρ_{0i} and l_x, l_y, l_z , the number of grid-points in every dimension nx, ny, nz and nv , and the time-step in terms of electron gyrofrequency $dt = 0.04/\Omega_{C,e}$.

In order to allow the growth of investigated global instabilities the simulation box must usually contain at least several ion gyroradii in every spatial dimension and at the same time the smallest scale (electron gyroradius or Debye radius) must be also resolved by at least one grid-step in order to prevent numerical instability. This dilemma poses a limit on the particle mass ratios (we could only reach as high as $m_i/m_e = 64$ in 3D

and $m_i/m_e = 150$ in 2D simulations so far). In a typical three-dimensional simulation we used $16 \times 16 \times 16$ coverage in the velocity space and $80 \times 80 \times 40$ resolution in the configuration space which amounts to approximately 30 Gb of RAM. Such a high memory task can be only completed on a parallel machine. The production runs were carried out on parallel IBM machines RS6000-SP and p690. The details about the parallelization techniques and efficiency and original technical solutions are discussed in the following section.

Our realization of Vlasov code consists of four separate blocks. First, the particle distribution functions are initialized as drift-Maxwellians:

$$f_j(\mathbf{r}, \mathbf{v}, t = 0) = \frac{n(z)}{(2\pi v_{th,j}^2)^{3/2}} \exp \left\{ -\frac{v_x^2 + (v_y - u_j)^2 + v_z^2}{2v_{th,j}^2} \right\}, \quad (4.1)$$

where $j = i, e$ for ions and electrons, respectively. The number density for both types of particles is set equal to ensure charge-neutrality.

The charge and current densities are integrated (zero- and first-order moments of the distribution function):

$$\begin{aligned} \rho &= \sum_j e_j \int f_j d^3v \\ \mathbf{j} &= \sum_j e_j \int \mathbf{v} f_j d^3v. \end{aligned} \quad (4.2)$$

Further, the Maxwell equations for electromagnetic fields are solved. In our version of the code the electromagnetic fields are expressed in terms of electrostatic and vector-potentials:

$$\begin{aligned} \mathbf{E} &= -\nabla\phi - \frac{\partial \mathbf{A}}{\partial t} \\ \mathbf{B} &= \nabla \times \mathbf{A}. \end{aligned} \quad (4.3)$$

The potentials are calculated by solving the Poisson and D'Alambert equations using the Coulomb gauge ($\nabla \cdot \mathbf{A} = 0$):

$$\begin{aligned} \Delta\phi &= -\frac{\rho}{\epsilon_0} \\ \Delta\mathbf{A} - \frac{1}{c^2} \frac{\partial^2 \mathbf{A}}{\partial t^2} &= -\mu_0 \mathbf{j}. \end{aligned} \quad (4.4)$$

Because we want to suppress the propagation of electromagnetic waves and subsequent heating of plasma we omit the part of displacement current $1/c^2 \nabla \partial\phi/\partial t$. There are two

reasons for doing this. The technical reason is that fluctuations during the initialization of simulation generate non-physical electromagnetic waves which heat the plasma and destroy the equilibrium within the first ion gyroperiod. Another theoretical argument against the displacement current term is that the investigated phenomena are all slow compared to the electromagnetic waves, i.e. $(\omega/(ck))^2 \ll 1$. For example, linear theories, which describe the instabilities investigated by our code, neglected completely the displacement currents. Thus, provided the technical problem with the initial noise and plasma heating could be eliminated, in the long-term dynamics the displacement currents would cause only a small error, probably comparable to the errors introduced by finite differentiation methods.

Finally, the electromagnetic fields are used to solve the Vlasov equations in order to update the particle distribution functions:

$$\frac{\partial f_j}{\partial t} + \mathbf{v} \cdot \frac{\partial f_j}{\partial \mathbf{r}} + \frac{e_j}{m_j} (\mathbf{E} + \mathbf{v} \times \mathbf{B}) \cdot \frac{\partial f_j}{\partial \mathbf{v}} = 0. \quad (4.5)$$

From this step the program returns to Equation (4.2) and the cycle repeats. This is the main program loop. The numerical analogues of Equations (4.2-4.5) are readily obtained by replacing integrals and derivatives by the numerical time- and space-centered sums or differences, respectively. The only exception is the Poisson equation (4.4), which is solved by the Gauss-Seidel iterative method (see e.g. *Press et al.* (1988) and *Hockney and Eastwood* (1988)).

4.2 Parallelization architectures

Because in our simulations we describe plasma by particle distribution functions in the six-dimensional phase space (three velocity coordinates and three configuration space coordinates) we have to provide sufficient computer memory and hence also processing power for our simulations. This can only be done on massively parallel computers. Typical requirements are of the order of 10 gigabytes (Gb) of memory. In order to process the data arrays in acceptable time we used up to 64 CPU's. We have implemented several parallel architectures, which are optimized for use with various types of parallel machines, depending on the memory access. In this section we shall describe the basic principles of

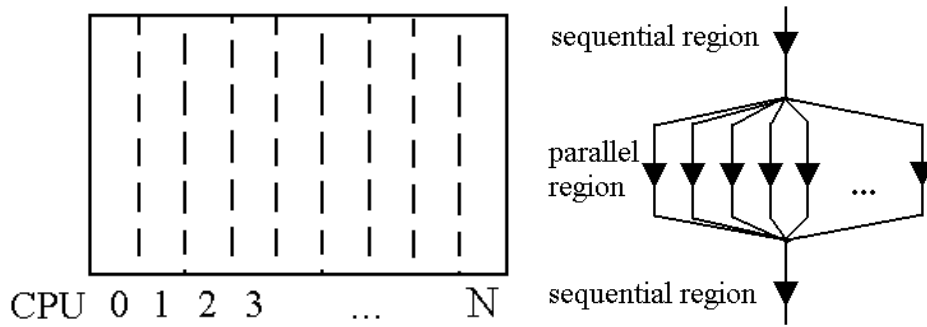


Figure 4.1: Schematic data-array decomposition between CPU's (left panel) and fork-join execution scheme (right panel) in parallel OpenMP region.

parallel computing and also give examples of particular technical solutions implemented in our numerical code.

4.2.1 OpenMP

One of the simplest parallelization standards is the OpenMP library (for details see **"Scientific Applications in RS6000 SP Environments"** at www.redbooks.ibm.com). On a machine with shared memory such as IBM p690 the parallelization is straightforward. The code is executed in a usual sequential manner and only the massive calculation loops are parallelized. Within each parallel loop the array of data is shared between different CPU's. The domain decomposition of the data array and the so-called "fork-join" execution of the code in the parallel region are shown schematically in Figure (4.1). In all our parallel simulations the domain decomposition was carried out along the spatial x -coordinate. For the optimal performance one has to ensure that the size of the decomposed array, i.e. the number of grid-points in the x -dimension, is proportional to the number of CPU's used. Then the job will be shared equally between all CPU's and the time losses for synchronization will be minimized.

The use of OpenMP is enabled by including the header file

```
#include <omp.h>
```

and by appropriate comments in the makefile during compilation and linking

```
mpicc_r -c -O3 -qsmp=omp ...
```


and

```
mpicc_r -lm -o vlasov -qsmp=omp ...
```

With the option `-qsmp = auto` every loop in the program will be parallelized automatically, which often leads to a less efficient execution of the run, since time will be lost for parallelization and synchronization of all small loops. With the option `-qsmp = omp` only the loops which are provided with a preprocessor header, e.g.

```
#pragma omp parallel for private(i)
```

will be executed in parallel. This allows to efficiently share the massive calculations between the CPU's and at the same time avoid the time losses during parallelization of the small loops, where the calculation time is comparable or smaller than the parallelization and synchronization time.

4.2.2 Message-Passing Interface (MPI)

On parallel machines with distributed memory where each CPU has access to its own block of memory, e.g. a Linux-PC cluster, the OpenMP parallelization loses sense. Instead, one has to use the message-passing interface (MPI) library (details under www.mpi-forum.org and "**RS6000 SP: Practical MPI Programming**" at www.redbooks.ibm.com). Being probably the most wide-spread and thus fully portable parallelization library, MPI has the only disadvantage that it must be explicitly programmed in the code. The MPI library is activated by linking the header file

```
#include <mpi.h>
```

The parallel environment is launched by the commands

```
MPI_Init (&argc, &argv);  
MPI_Comm_size (MPI_COMM_WORLD, &nprocs);  
MPI_Comm_rank (MPI_COMM_WORLD, &npid);
```

where *nprocs* and *npid* correspond to the total number of MPI-tasks and the private id-number of a given task. The aim of parallelization is to decrease the calculation time

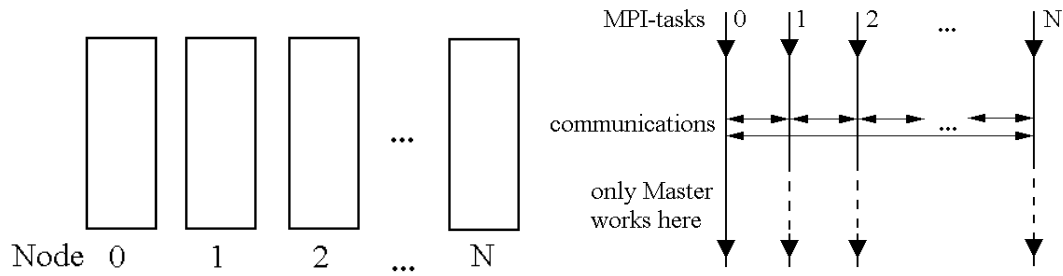


Figure 4.2: Schematic domain decomposition between nodes (left panel) and parallel execution scheme (right panel) of an MPI code.

or to bind together separated memory resources. From this point of view it is worth to initialize only one task on every CPU/memory block, although technically it is possible to launch more than one task on every CPU. Now, the domain decomposition is carried out in the same manner as in the shared-memory case, with the only exception that each CPU "knows" only its own part of the data and "does not know" anything about the rest of the field. The domain decomposition and the execution scheme are illustrated in Figure (4.2).

In every calculation loop corresponding to a differential equation, each CPU needs the parts of the data-arrays from the neighbours directly adjacent to it. In the Equations (4.3-4.5) we encounter the following spatial derivatives along the x-axis: $\partial\phi/\partial x$, $\partial A_x/\partial x$, $\partial A_y/\partial x$, $\partial A_z/\partial x$, $\partial f_i/\partial x$ and $\partial f_e/\partial x$. It means that the layers of arrays containing ϕ , A_x , A_y , A_z , f_i and f_e must be sent from each CPU to its neighbours. In a typical production run the size of such data blocks can reach up to 16 Kb for the potentials and up to 60 Mb for the distribution functions. Such volumes of data do not cause any significant time delays on machines connected by Gigabit Ethernet or on IBM RS6000-SP with high performance switch. An example of distribution function layers exchanged between different MPI-tasks is given below:

```
Vlasov_solver(...);

for(ip=0;ip<nprocs;ip++){
  if(npid==ip){
    if(ip==0){
```

```

    for(i=0;i<sx;i++){right[i]=fi[sall-2*sx+i];}
    istat=MPI_Send(&right[0],sx,MPI_FLOAT,ip+1,0,
MPI_COMM_WORLD);
}
if(ip>0 && ip<nprocs-1){
    istat=MPI_Recv(&right[0],sx,MPI_FLOAT,ip-1,0,
MPI_COMM_WORLD,&status);
    Vlasov_bound(...);
    for(i=0;i<sx;i++){right[i]=fi[sall-2*sx+i];}
    istat=MPI_Send(&right[0],sx,MPI_FLOAT,ip+1,0,
MPI_COMM_WORLD);
}
if(ip==nprocs-1){
    istat=MPI_Recv(&right[0],sx,MPI_FLOAT,ip-1,0,
MPI_COMM_WORLD,&status);
    Vlasov_bound(...);
}
}
}
istat=MPI_Barrier(MPI_COMM_WORLD);

for(ip=0;ip<nprocs;ip++){
    if(npid==ip){
        if(ip>0){
            for(i=0;i<sx;i++){left[i]=fhelpt[i];}
            istat=MPI_Send(&left[0],sx,MPI_FLOAT,ip-1,0,
MPI_COMM_WORLD);
        }
        if(ip<nprocs-1){
            istat=MPI_Recv(&left[0],sx,MPI_FLOAT,ip+1,0,
MPI_COMM_WORLD,&status);

```

```

    Vlasov_bound( . . . );
}
}
}
istat=MPI_Barrier(MPI_COMM_WORLD);

```

In this code passage first the Vlasov equation is solved in the inner volume of each domain. Then, every MPI-task with id-number $npid$ first sends its right part of the array $fhelp$ consisting of sx elements of size MPI_FLOAT to its right neighbour with id-number $npid + 1$. Then each task receives the parcel and solves Vlasov equation at the left-most boundary of the domain. The thread corresponding to the left-most domain ($npid == 0$) only sends the parcel and the thread corresponding the right-most domain ($npid == nprocs - 1$) only receives the parcel. Then, the left-most boundaries of all threads are exchanged in the similar manner. Afterwards the left-most layer from the left-most node $npid == 0$ is sent to the right-most node and, vice-versa, the right-most node sends the right-most part of its distribution functions arrays to the left-most node in order to satisfy the periodic boundary conditions.

A particularly tricky situation occurs with the iterative Gauss-Seidel solver for the potentials. The point is that this loop carries out the differentiation many times per cycle. In this case transmitting/receiving even small packages of data is too costly. In order to avoid it we gather the arrays of charge and current densities from all MPI-tasks on the Master ($npid = 0$) and solve the iterative routine locally on the Master-thread, while other tasks are suspended. Then, the necessary domains of the resulting potentials are redistributed among all the threads. Compared to jobs parallelized with OpenMP architecture, the productivity of MPI-runs increases slower with the increasing number of CPU's, because the inter-processor traffic (the number of communication commands and the volume of data sent) increases proportionally.

4.2.3 Hybrid architecture

The most general case of parallel architecture is the "hybrid" one when MPI and OpenMP libraries are combined (recommended reading "**Scientific Applications in RS6000 SP**

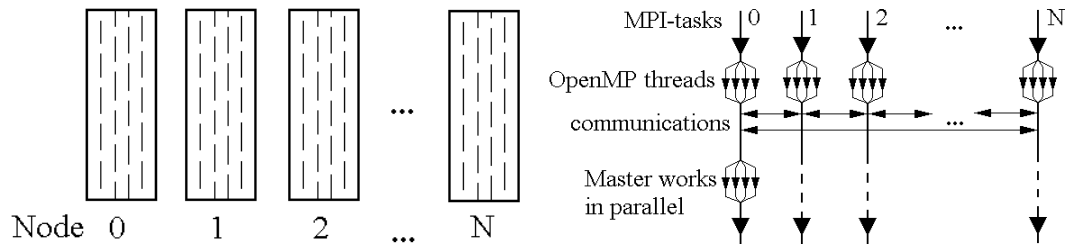


Figure 4.3: Schematic domain decomposition between nodes and CPU's (left panel) and execution scheme (right panel) of a code with hybrid parallel architecture.

Environments" at www.redbooks.ibm.com). This architecture has been successfully employed for $2\frac{1}{2}D$ Vlasov simulations on the IBM RS6000-SP machine at GWDG. On this machine four processors have access to a common 2 Gb memory block. This unit is called a node. The nodes are connected between each other by the IBM high-performance switch, which enables high-rate data traffic between the nodes. Thus, it makes sense to start a single MPI task on each node to avoid the MPI-communications within the single memory block and keep only the necessary data traffic between the isolated domains. At the same time the processing of the data in each domain is carried out by all the CPU's which have access to it, i.e. under the OpenMP parallelization. This architecture uses the advantages of both standards in the most rational way. It is also portable as is on any other hardware, e.g. several IBM Regatta machines connected by Ethernet. The domain decomposition and the execution line are schematically illustrated in Figure (4.3).

An example of hybrid parallel code is given below.

```
#ifdef _OPENMP
#pragma omp parallel for private(i)
#endif
for(i=0;i<nxnz;i++){
    glsigma[npid*(nxnz-nz)+i]=sigma[i];
}
for(ip=0;ip<nprocs;ip++){
    if(npid==ip){
        if(ip==0){
```

```

    for(i=1;i<nprocs;i++){
        istat=MPI_Recv(&glsigma[i*(nxnz-nz)],nxnz,
            MPI_DOUBLE,i,0,MPI_COMM_WORLD,&status);
    }
}
if(ip>0){
    istat=MPI_Send(&glsigma[ip*(nxnz-nz)],nxnz,
        MPI_DOUBLE,0,0,MPI_COMM_WORLD);
}
}
}
istat=MPI_Barrier(MPI_COMM_WORLD);

for(ip=0;ip<nprocs;ip++){
    if(npid==ip){
        if(ip==0){
            Poisson(glsigma,glphi,schritt);
        }
    }
}
istat=MPI_Barrier(MPI_COMM_WORLD);

for(ip=0;ip<nprocs;ip++){
    if(npid==ip){
        if(ip==0){
            for(i=1;i<nprocs;i++){
                istat=MPI_Send(&glphi[i*(nxnz-nz)],nxnz,
                    MPI_DOUBLE,i,0,MPI_COMM_WORLD);
            }
        }
    }
    if(ip>0){

```

```

    istat=MPI_Recv(&glphi[ip*(nxnz-nz)],nxnz,
    MPI_DOUBLE,0,0,MPI_COMM_WORLD,&status);
}
}
}
#ifdef _OPENMP
#pragma omp parallel for private(i)
#endif
for(i=0;i<nxnz;i++){
    phi[i]=glphi[npid*(nxnz-nz)+i];
}
istat=MPI_Barrier(MPI_COMM_WORLD);

```

In this passage the local arrays of charge density *sigma* are gathered from all nodes to the array *glsigma* on the Master-node. Notice that all assignment operations on each node are provided with the OpenMP statements. After the Master-node solves the Poisson equation using the charge density *glsigma* and records new values of the electrostatic potential in *glphi* array the appropriate parts of this array are distributed among other nodes and copied to usual *phi* data-set.

The efficiency of the production runs on different machines, with different numbers of CPU's and different parallelization can be estimated by the calculation time per one program cycle. The time measured for this purpose is not the CPU-time but the so-called "wall-clock time". Instead of standard *clock()* function it is measured by the function

```

double zeit(void){
    static double tima=0.;
    double tim, t=0.;
    tim=(double)MPI_Wtime(); t=tim-tima; tima=tim;
    return (t);
}

```

Every time the function *zeit()* is called it returns the time in seconds which elapsed since it was called last time. Contrary to the *clock()* function which has different values on

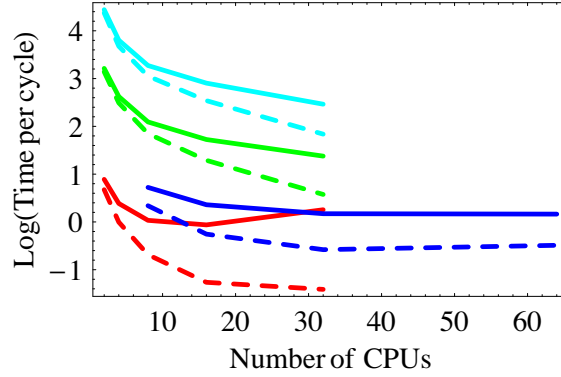


Figure 4.4: Logarithm of wall-clock time per one program cycle (logarithmic scale) of OpenMP (red green and cyan lines) on IBM p690 and hybrid parallelization techniques on IBM RS6000-SP (blue lines) for different numbers of CPU's used. Solid lines show the full program cycle duration, dashed lines correspond to fully parallel part of the cycle. The cyan lines are drawn for the run with 30 Gb memory block, the green - 8 Gb, red and blue - 800 Mb.

different CPU's, the $MPI_Wtime()$ function is uniquely defined on all CPU's/MPI tasks.

The time required for one program cycle depends on the number of CPU's involved can be estimated as approximately

$$\Delta t = \frac{t_{calc}}{N_{CPU}} + t_{sync} \times N_{CPU}, \quad (4.6)$$

where t_{calc} is the total calculation time and t_{sync} is the time needed for synchronization, parallelization and communication. The first term t_{calc} is usually proportional to the size of the memory block used by the program, while the other, t_{sync} , is constant. Thus, it is impossible to separate the diagnostics of the program efficiency from its memory consumption. Figure (4.4) demonstrates this effect. In this figure we compare relative calculation time (in seconds, logarithmic scaling) of a $2\frac{1}{2}D$ Vlasov-code test-run with approximately 800 Mb on IBM RS6000-SP with hybrid architecture (blue lines) and OpenMP version with 800 Mb, 8 Gb and 30 Gb (red, green and cyan lines, respectively) memory on IBM p690 machine. The solid lines correspond to the total program cycle (integration of distribution function moments, calculation of potentials and electromagnetic fields and solving the Vlasov equation), while the dashed lines show only the fully-parallelized part of the cycle (without iterative Gauss-Seidel solver). For the 800-Mb memory test-run

the amount of calculations is rather small and the synchronization and communication time with the increasing number of CPU's become comparable to the calculation duration. Hence, the strong saturation tendency in both red and blue dashed curves. The solid red and blue curves even show the increase of the calculation time because they include a sequential part which is not accelerated by the use of more processors, but the synchronization and traffic duration before and after it increase. However, for massive production runs with large memory the amount of calculation work exceeds significantly the synchronization and communication part and the time gain with more CPU's is very efficient. Thus, one can see, that it takes longer to execute a small-memory job on 32 or 64 CPU's than on 16, while the high-memory jobs may still run faster on an even larger number of processors.

Chapter 5

Simulation results

5.1 Thin current sheets with anti-parallel magnetic fields

5.1.1 Resonant interaction of lower-hybrid drift waves with ion flow

As we have already said in the introduction section, in the regions of plasma density gradients a fast lower-hybrid drift instability (LHDI) is excited (see e.g. *Krall and Liewer* (1971); *Davidson and Gladd* (1975); *Davidson et al.* (1976); *Huba et al.* (1978)). This mode is driven unstable by the diamagnetic current produced by the pressure inhomogeneity. Originally, it was suggested that the LHDI could increase the reconnection growth rate by dissipating magnetic field energy. However, it is strongly dependent on the local plasma beta and is suppressed near the current sheet proper. Some numerical investigations demonstrated that the LHDI is not completely stabilized in the high-beta inner region of the current sheet *Winske* (1981); *Tanaka and Sato* (1981). Also, the detailed consideration of kinetic effects for both particle species revealed strong tearing mode growth rate increase in the presence of LHDI (see *Sundaram and Fairfield* (1995, 1996)). There are at least two important reasons why numerical simulations are more favourable for studying this problem. First, the sharp gradients at the current sheet edges might render the local analytical description of the instability invalid. Second, the nonlinear phase of the instability, interaction of different modes and various kinetic processes can only be self-consistently described in simulations, while analytical theory considers each process separately.

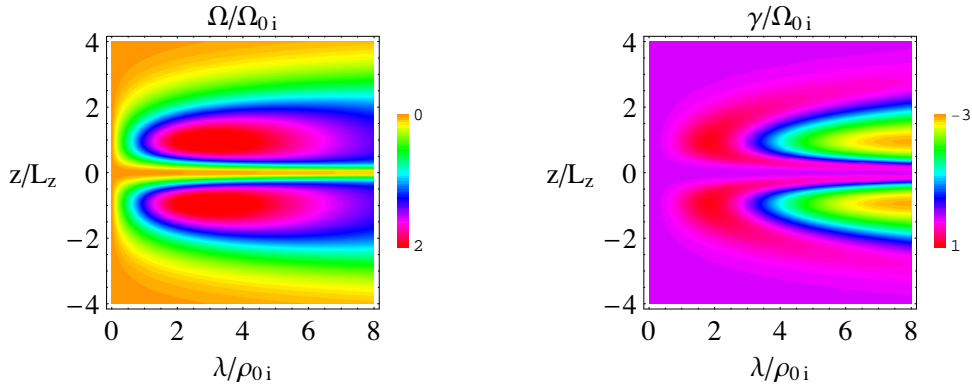


Figure 5.1: Linear dispersion relations for lower-hybrid drift waves as given by *Huba et al.* (1978, 1980): left panel - oscillation frequency, right panel - growth rates. For direct comparison with simulations the dispersion relations are calculated for particle mass ratio $m_i/m_e = 16$.

In Harris-type current sheets the drift velocities of particles are inversely proportional to the thickness of the sheet and related by the particle temperature ratio:

$$\begin{aligned} u_i &= 2v_{th,i}\rho_{0i}/L_z \\ u_e &= -u_i T_e/T_i. \end{aligned} \quad (5.1)$$

As follows from Figure (5.1), the fastest-growing LHD waves are excited in the regions of maximum density gradient at the edges of the current sheet. At the center of the current sheet the waves do not grow and further to periphery longer waves tend to be more unstable. The LHD waves, drifting at the diamagnetic drift velocity, encounter a positive slope of ion distribution function, i.e. more ions which are faster than the wave and fewer ions which are slower than the wave. With the counter-streaming electrons the situation is opposite - the majority of electrons drifts against the wave and only few faster than the wave. In this situation the free energy of the ion flow can be transformed to amplify the wave through the inverse Landau resonance. The electrons, on the other hand act to damp this mode through the direct Landau-resonance.

In order to demonstrate the resonant wave-particle interactions through Landau damping we diagnose the perturbations of the particles' distribution functions. Figure (5.2) demonstrates typical perturbations of particle distribution functions as a result of resonant

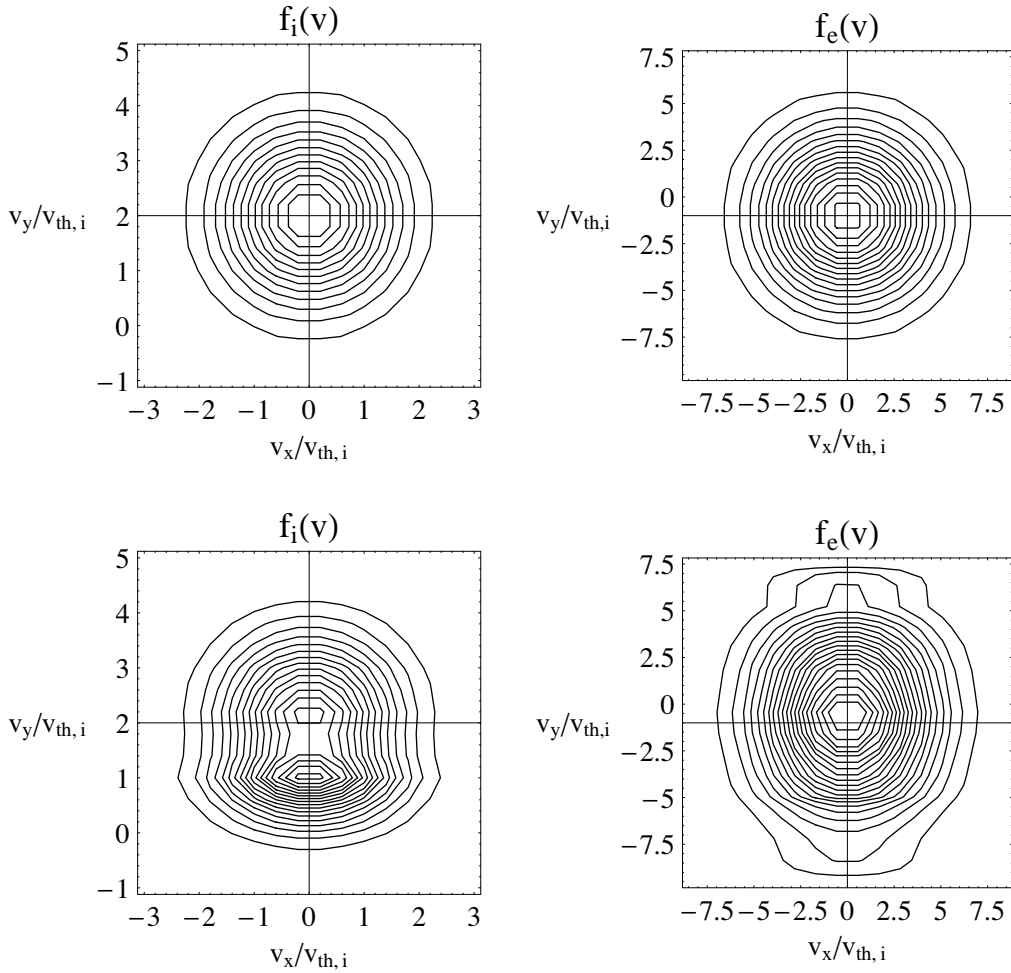


Figure 5.2: Two-dimensional perturbations of local distribution functions (ions - left, electrons - right) at the edge of a current sheet. Upper panel shows the initial distribution, lower panel corresponds to the time $t\Omega_{0i} = 27$ obtained in simulation with particle mass ratio $m_i/m_e = 16$.

interaction with LHD waves. One sees a prominent peak forming in ion distribution near $v_y = v_{th,i}$, which corresponds to the group velocity of LHD waves. In the electron distribution the perturbation is smoother, since the trapping condition is fulfilled in a wider phase space volume, but the tendency is the same - an increase of electrons drifting in the positive Y-direction is seen. This situation is encountered in the local potential well, the configuration space region with local electrostatic potential minimum. At the potential barrier the situation is inverse - there is a lack of particles in the vicinity of LHD

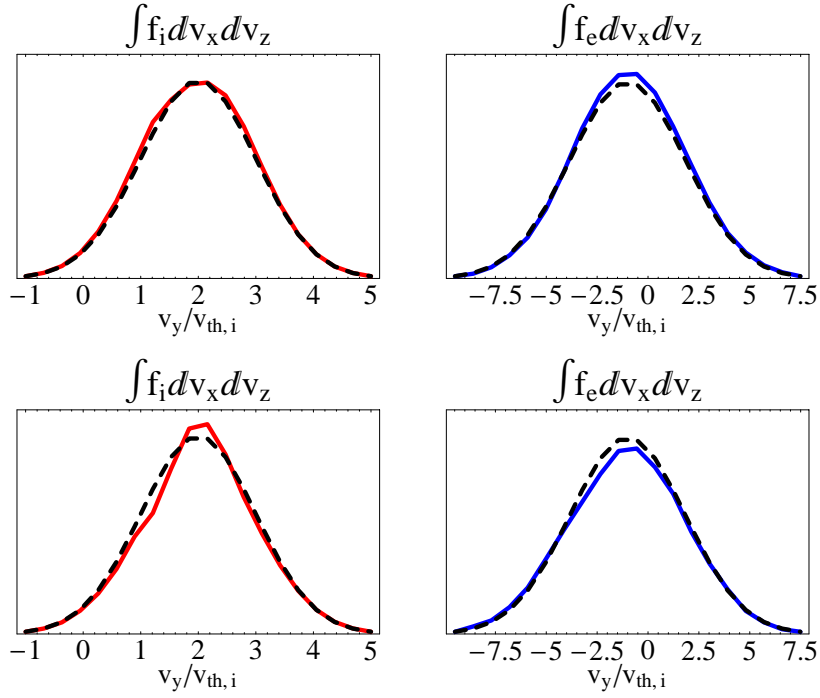


Figure 5.3: Perturbations of reduced local distribution functions (ions - left, electrons - right) at the edge of a current sheet. Upper and lower panels corresponds to potential well and potential barrier, respectively. The dashed lines show the initial Maxwellian distributions. Results of Vlasov-code simulation with particle mass ratio $m_i/m_e = 32$.

group velocity. For comparison, we show reduced distribution functions with only one dimension along v_y at local potential well and at local potential barrier (Figure (5.3)).

As a result of resonant amplification by ions, the lower-hybrid drift waves grow exponentially with growth rate of the order of ion gyrofrequency and expand from the current sheet edges further to the periphery and towards the neutral plane (Figure (5.4)). In the Figure (5.4) we plotted the Fourier component of current-aligned electric field (normalized to B_0) corresponding to the fastest-growing LHD wave mode plotted versus the cross-current sheet Z-axis and time. The colour coding shows that the LHD waves are first excited at the current sheet edge (in accordance with the linear theory prediction) and then the domains of LHD activity expand, also towards the high plasma beta regions near current sheet center.

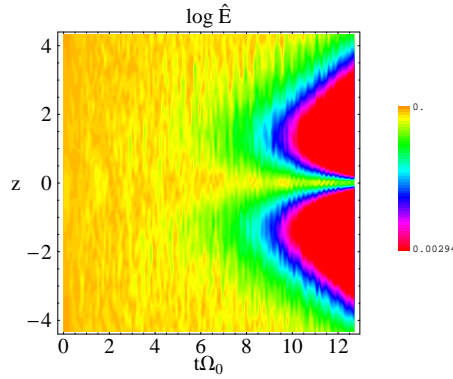


Figure 5.4: Temporal evolution of current-aligned electric field Fourier component corresponding to the dominant LHD wave mode revealing penetration of LHD waves to the current sheet center.

5.1.2 Coupling between the resonantly amplified lower-hybrid drift waves and the eigenmodes of the current sheet

As was demonstrated by eigen-mode theory of *Yoon et al.* (2002), the LHD waves are the higher-order eigen modes of thin current sheets. Apart from these eigen modes localized at current sheet edges, there are also global modes, which grow at the central plane of the current sheet. A linear instability theory or eigen-mode theory cannot self-consistently describe the interaction between different eigen modes. That is why numerical simulations are necessary to solve such problems. In our Vlasov-code simulations we investigated the triggering of global current sheet oscillations by the LHD waves. It appeared that as the LHD waves from the opposite edges penetrate to the neutral plane. Being completely independent from each other, they can have any relative phase shift. Since a whole spectrum of different LHD waves is excited, sometimes the dominant modes at the opposite edges of the current sheet may even have slightly different wavelengths and frequencies. As a result, the interaction of these waves can lead to excitation of both symmetric sausage-modes and asymmetric kink-modes with equal probability. We propose to call this global current sheet mode a drift-resonant instability (DRI). Frequency and wavenumber of the fastest-growing DRI mode scale with the LHD frequency $\Omega_{LH} = \omega_{pi}(1 + \omega_{pe}^2/\Omega_{0e}^2)^{-1/2} \approx (\Omega_{0i}\Omega_{0e})^{1/2}$ and the LHD wavenumber

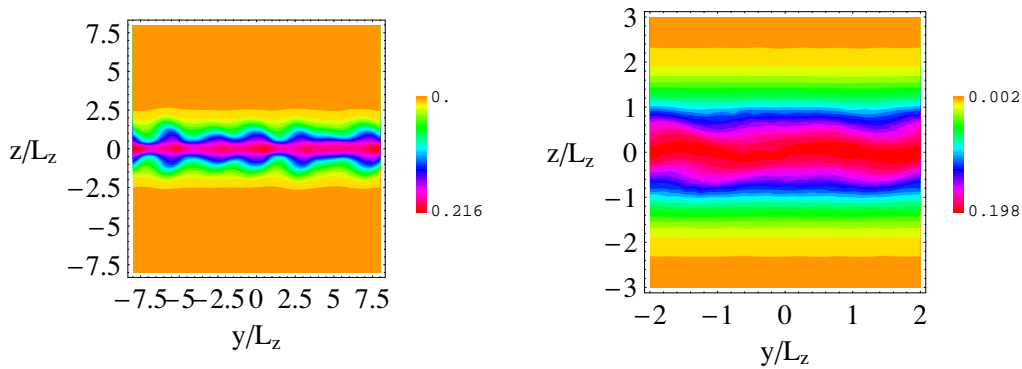


Figure 5.5: Examples of even sausage-mode and odd kink-mode instabilities in a thin current sheet (as seen in plasma density). The different wavelengths are due to different particle mass ratios used in simulations ($m_i/m_e = 25$ for the left and $m_i/m_e = 100$ for the right figure, respectively).

$k_{LH} = \Omega_{LH}/v_{th,i} \approx \rho_{0i}^{-1}(m_i/m_e)^{1/2} \approx \rho_{0e}^{-1}(T_e/T_i)^{1/2}$, respectively. At the same time, the growth rate of the instability scales with ion gyrofrequency, thus implying that the global instability grows due to ion dynamics.

Apart from numerical stability, diagnostics and visualization techniques, one of the most difficult questions related with simulations is the scaling of results with real physical values and extrapolation to the realistic parameters, e.g. particle mass ratio. In order to estimate the relevance of the instabilities discussed above one has to make sure that they still exist for higher mass ratios and estimate their wavelength and oscillation frequency. Having this in mind, we carried out simulations for several mass ratio values. The results are presented in Table (5.1).

It follows immediately, that the wavenumber and oscillation frequency of the instability change with mass ratio in terms of ion gyroradius and gyrofrequency, but remain practically constant in terms of hybrid spatial and temporal scales: $k \approx 0.5k_{LH} = 0.5\rho_{0i}^{-1}(m_i/m_e)^{1/2} = 0.5r_{0e}^{-1}(T_e/T_i)^{1/2}$ and $\omega = \Omega_{LH}/(2\pi)$. Indeed, the wavenumber of the instability is almost exactly proportional to $(m_i/m_e)^{1/2}$, as first discovered by *Pritchett et al.* (1996) (see Figure (5.6)). At the same time, the growth rate in terms of lower-hybrid frequency changes stronger than in terms of ion gyrofrequency. Indeed, as we have shown, the global mode is driven by the inverse Landau-resonance of LHD waves with

m_i/m_e	T_i/T_e	$k\rho_{0i}$	k/k_{LH}	Ω/Ω_{0i}	ω/Ω_{LH}	γ/Ω_{0i}	γ/Ω_{LH}
4	1	1.2	0.6	0.12	0.06	0.7	0.35
10	2	1.6	0.5	0.18	0.06	0.62	0.2
16	2 - 7	1.7	0.44	0.29	0.07	0.53	0.13
32	3	2.3	0.41	0.5	0.09	0.45	0.08
50	5	3.1	0.45	0.65	0.09	0.42	0.06
64	7	3.9	0.5	0.75	0.09	0.4	0.05
100	11	4.5	0.45	0.8	0.08	0.38	0.04

Table 5.1: Dependence of the nonlinear global instability properties (wavenumber k , frequency Ω and growth rate γ) on the simulation parameters (particle mass m_i/m_e and temperature T_i/T_e ratios).

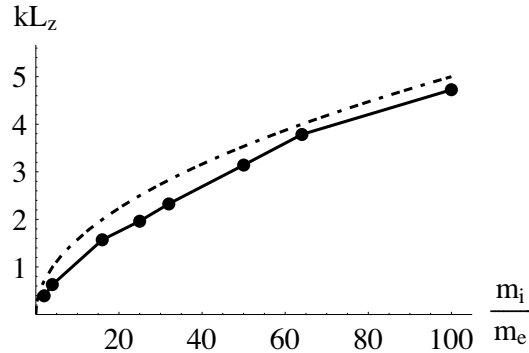


Figure 5.6: Dependence of the wavenumber of the drift resonant instability on the particle mass ratio used in simulations (dots, solid line). For comparison, analytic dependence $0.5 (m_i/m_e)^{1/2}$ is given (dashed line).

ions and thus it should come as a logical consequence that the instability growth rate is different from the one of LHDI.

When the simulation box allowed a large number of wavelengths we also observed excitation of several LHD modes to the same amplitude. In this case the waves can locally enhance or deplete each other along their propagation direction. This effect further complicates the situation with global modes triggering. As an example, we show current-aligned electric field and plasma density obtained in a simulation with $m_i/m_e = 16$

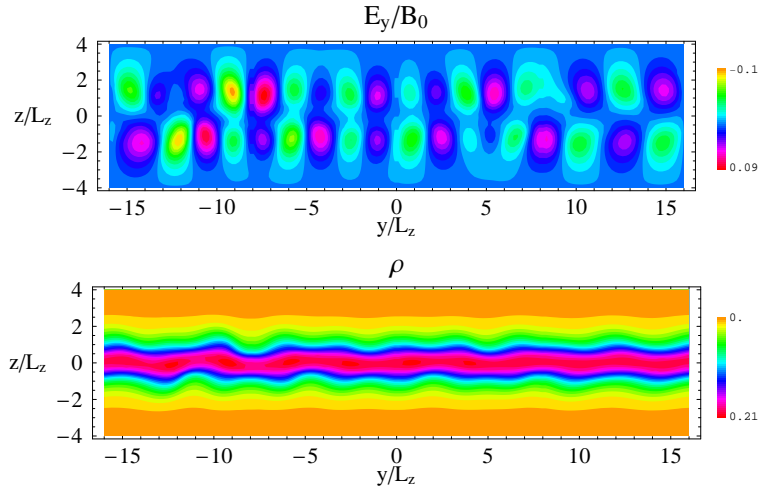


Figure 5.7: Examples of mixed sausage and kink modes obtained in a thin current sheet (upper panel - E_y electric field, lower panel - plasma density). Obtained in a simulation with $m_i/m_e = 16$.

(Figure (5.7)). One sees clear odd-parity waves near the edges of the simulation box and even-parity wave at the center of the box. Since in turbulent space plasmas there are strong variations in plasma and magnetic field properties, the local dispersion of LHD waves may favour development of different wavemodes and thus, the mixed-parity instability shown in Figure (5.7) is probably the most realistic one.

We have considered thin current sheets (half-width $L_z \in [0.5\rho_{0i}, 2\rho_{0i}]$) with anti-parallel magnetic fields. The measured growth rates of global oscillations at the current sheet center decrease drastically for thick current sheets with $L_z \rightarrow 2\rho_{0i}$, and slightly saturate when the half-width decreases below $0.5\rho_{0i}$ (see Figure (5.8), solid line). The examination of the electric fields in the extremely thin sheets showed that the global instability follows immediately after the LHD waves appear. Thus, current sheets with half-widths $L_z \leq 0.5\rho_{0i}$ decay due to direct interaction of LHD waves with the meandering particles at the current sheet center. Figure (5.8) also demonstrates that the tearing-mode instability (thin line) grows almost as fast as the current-driven mode in thin current sheets. This is due to the direct coupling of these two modes, as we show below.

We also compared the growth rates of the tearing-mode instability from two- and three-dimensional simulations for various current sheet thicknesses (see Figure (5.9)).

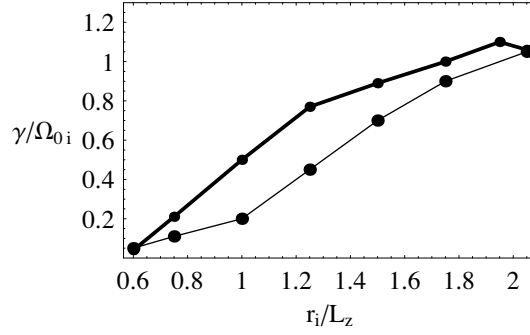


Figure 5.8: The dependence of the global wave-mode (thick line) and tearing (thin line) growth rates on the current sheet thickness.

Contrary to the forced two-dimensional reconnection case, where magnetic island is introduced into the simulation by thinning of the current sheet, in our simulations we did not perturb the current sheet, but looked for spontaneous reconnection. As a result, instead of linear growth of reconnected flux, as typically obtained in forced reconnection configurations (see e.g. *Birn et al. (2001); Silin and Büchner (2003)*), we obtained exponential growth. This growth of the tearing-mode instability at the current sheet center also strongly increased for thinner current sheets. However, in the two-dimensional case the tearing-mode is always weaker than the current-driven instability, while in the 3D simulations for thin sheets the growth of the tearing mode becomes almost equal to the growth of the LHD-induced mode. We would like to explain the increase of tearing-mode growth rate due to the LHD-waves. The tearing mode starts growing exponentially immediately after the simulation begins, while the perturbations due to the current-driven waves first appear after the LHD waves have been excited at the current sheet edges. Then, the wave-perturbations need some time to penetrate to the current sheet center. This time delay also strongly depends on the current sheet thickness - for $L_z = 2\rho_{0i}$ it is approximately $15\Omega_{0i}^{-1}$, while for $L_z = \rho_{0i}$ it is only 7 - 8 Ω_{0i}^{-1} . In thinner sheets the LHD waves interact directly with the meandering particles at the center of the sheet, i.e. there is no time delay.

Let us now consider the consequence of the global LHD-induced drift-resonant instability (DRI) for reconnection. Figure (5.10) demonstrates the three-dimensional structure of the instability. The dark and light domains correspond to the maximum positive and minimum negative domains of current-aligned E_y electric field (left) and normal B_z mag-

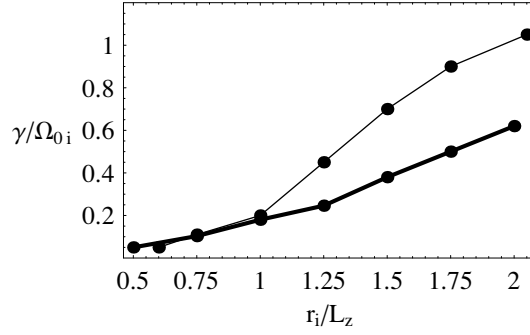


Figure 5.9: The dependence of the tearing-mode instability growth rate on the current sheet thickness measured in the two-dimensional (thick line) and three-dimensional (thin line) simulations. In the two-dimensional simulations the growth rate smoothly increases for thinner sheets but always remains small compared to the growth rate of the current-aligned waves.

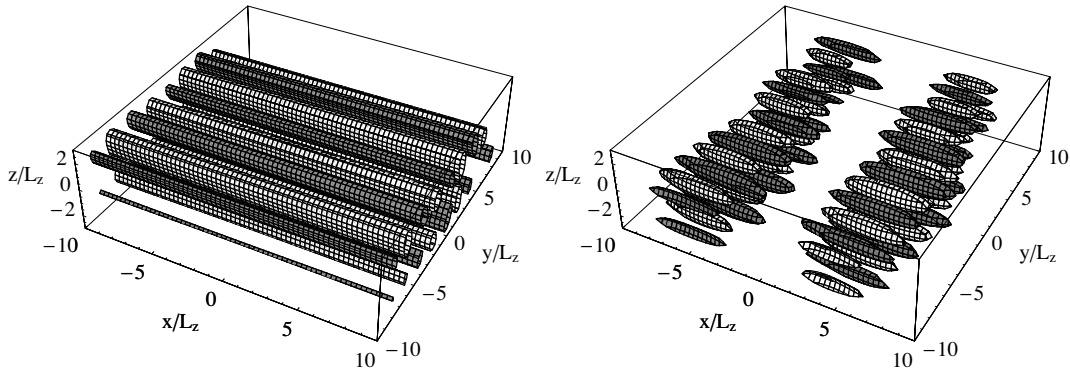


Figure 5.10: The maximum and minimum domains of current-aligned electric field E_y (left) and normal magnetic field B_z (right) at $t\Omega_{0i} = 25$ obtained in 3D simulation with antiparallel fields.

netic field (right), respectively. These structures drift in the ion flow direction with velocity $v_y \approx v_{th,i}$. The formation of the "cigar-like" LHD domains in magnetized plasmas is an example of the self-organizing structures, described, for example by *Tsytovich* (1995). The cross-section of B_z field at the neutral plane at $t\Omega_{0i} = 25$ (Figure (5.11)) shows a wave-like profile in the Y-direction and at the same time a tearing-mode reconnection, i.e. the change of sign at $x = 0$.

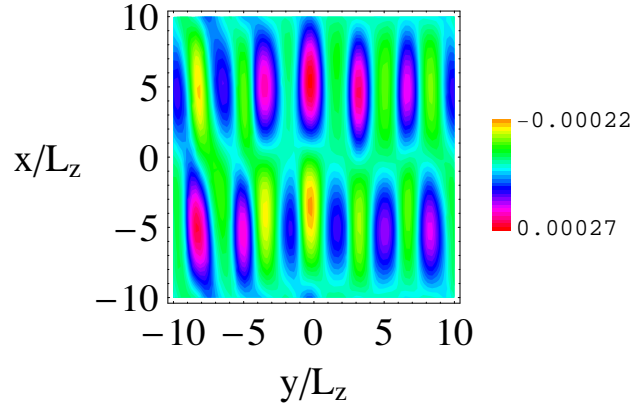


Figure 5.11: Cross-section of normal magnetic field component B_z/B_0 at the neutral plane $z = 0$ at $t\Omega_{0i} = 25$ in a 3D simulation. One sees the periodic wave structure in current direction which corresponds to the sausage-mode instability and the change of sign across the line $x = 0$ which shows the tearing-mode instability.

Figure (5.12) demonstrates the temporal evolution of the main unstable modes of the current sheet. The curves show the temporal evolution of the Fourier modes of the current-aligned electric field E_y corresponding to the LHD waves at the edge of the sheet (dashed line), the global mode with the dominant LHD wavelength at the center of the sheet (solid line) and the tearing-mode with half-period along the X-axis (dash-dotted line). These Fourier modes were obtained for a single data set with $m_i/m_e = 16$ and $T_i/T_e = 2$. They show the consequent action of the global wave and reconnection structures growth shown in Figures (5.10) and (5.11). One sees that in the beginning the tearing-mode quickly reaches certain level and then continues to grow very slowly (dash-dotted curve). At the same time, the LHD modes are excited at the edges of the sheet (dashed curve) and then, as a consequence, the global current-driven instability of the sheet follows (solid curve). After the E_y component of the global current-aligned mode reaches the level of the reconnection E_y perturbations they continue their growth together at the rate of the global LHD mode.

The topology of the resulting 3D reconnection is presented in Figure (5.13). One can see two classical X- and O-line structures changing polarity along the Y-axis. There is a clear periodicity in the Y-direction. This way the structure of tearing-mode instability can directly couple to the current-driven mode of the current sheet. At a first glance, the

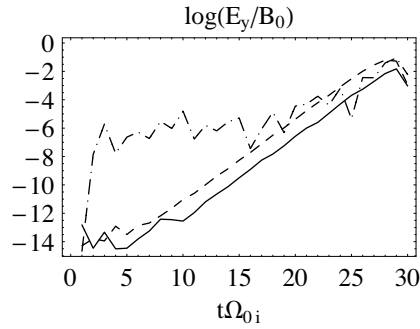


Figure 5.12: Temporal evolution of the dominant LHD mode $k_y L_z = 0.5\pi$ at the edge of the current sheet (dashed line), the global mode at the center of the sheet (solid line) and the tearing-mode instability obtained in 3D simulation (dash-dotted line).

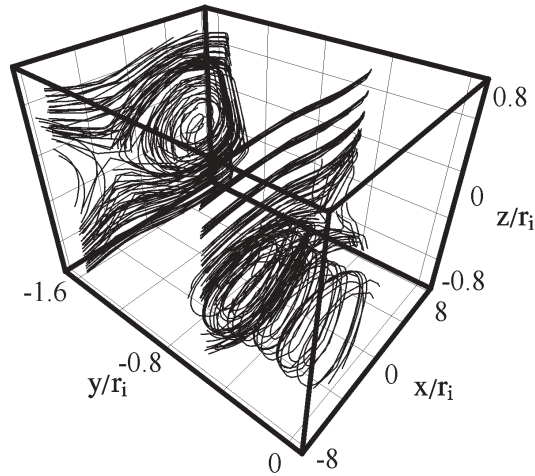


Figure 5.13: The three-dimensional structure of reconnected magnetic field lines at $t\Omega_{0i} = 25$ obtained in a simulation run with antiparallel magnetic fields and current sheet half-thickness $L_z = \rho_{0i}/1.5$. For the sake of clarity of presentation the box size in the Y dimension is limited to one LHD wavelength only.

small-scale structure of reconnection contradicts the traditional expectation of reconnection as a large-scale process, because long-wavelength modes more efficiently interact with particles, since particle travel time in the wave field is longer. But there is one aspect which must be kept in mind, the longer waves must be excited before the short waves destroy the current sheet. Here we are dealing with competing processes: either LHD waves destabilize the current sheet through the inverse Landau resonance with ions, or

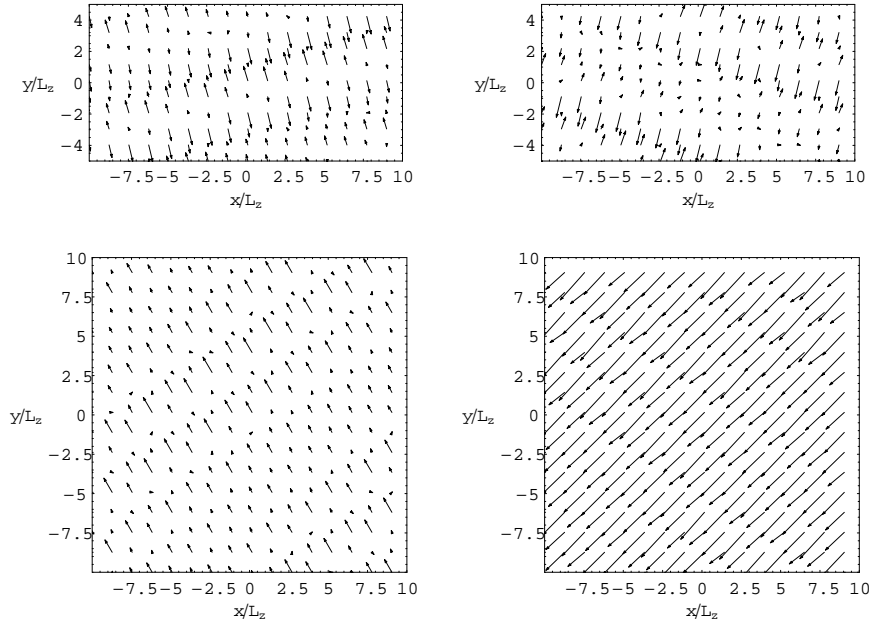


Figure 5.14: Two dimensional vector-plots of electric fields in the XY-planes at $z = L_z$ (left panel) and $z = -L_z$ (right panel). The upper and lower panels show simulation results for the guide field $B_{y0}/B_0 = 0.25$ and 0.5 respectively.

tearing-mode instability will be excited by the Landau resonance with electrons. If a 2D tearing-mode is triggered, e.g. by current sheet thinning along the $x = 0$ line, it will suppress the current-aligned modes from ever appearing and the current sheet will decay through the classical 2D reconnection. But, alternatively, if the current-aligned modes are excited first by internal turbulence of the current sheet, they will subsequently trigger kink- or sausage-eigenmodes of the sheet in the current direction and the tearing-mode. In that case the current sheet will quickly decay through the three-dimensional small-scale reconnection.

5.2 Thin current sheets with guided magnetic fields

In order to investigate the influence of a constant guide field we varied B_{y0}/B_0 up to 1 and show here the results for mass ratio $m_i/m_e = 16$. The simulations with different values of guide magnetic field amplitude revealed the generation of two independent LHD modes, one above the neutral plane and one below propagating at angles $\theta \approx \pm \arctan(B_{y0}/B_0)$ to the current flow direction. This way the LHD waves propagate always perpendicular to

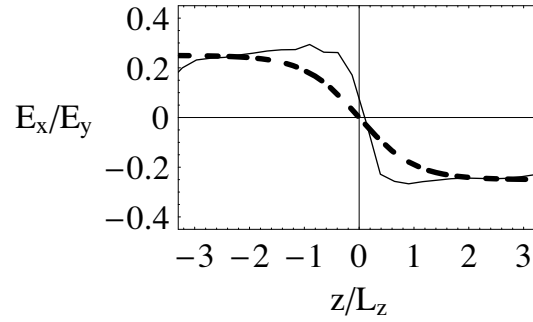


Figure 5.15: The ratio of electric field components E_x/E_y at different distances from the neutral plane with guide field $B_{y0}/B_0 = 0.25$. The dashed solid line shows theoretical dependence $-0.25 \tanh(z/L_z)$.

the local magnetic field ($\mathbf{k}_{LH} \cdot \mathbf{B} = 0$) (see e.g. *Huba et al. (1980)*). An example shown in Figure (5.14) demonstrates the electric fields in the horizontal planes $z = \pm L_z$. The mean electric field in the X-Y planes also are longitudinal, i.e. in the wave propagation direction. Since the local magnetic field direction rotates around the Z-axis, the electric field of the LHD waves follows the law $B_x(z)/B_y(z) \sim \tanh(z/L_z)$. In fact, the ratio E_x/E_y is equal to tangent of the angle between the electric field orientation and the current flow direction. In the regions where the LHD waves have non-zero electric fields this ratio should also follow the $\tanh(z/L_z)$ dependence. Figure (5.15) demonstrates that, indeed, the direction of the electric field of the wave tends to keep perpendicular to the local magnetic field. One can notice that E_x/E_y turns to zero at the neutral plane due to the fact that the LHD waves are excited outside the current sheet. The electric fields can only reach the $z = 0$ plane due to penetration of the LHD waves towards the center of the sheet similarly to the 2D case (see Figure (5.16)). Hence, at distances $|z| \geq L_z$ from the neutral plane the y- and x-components of the electric field are proportional $E_x = E_y \sin \theta$, where the propagation angle $\theta = \pm \arctan(B_{y0}/B_0)$. Taking this into account, one can visualize the evolution of instability in the 3D space by diagnosing the amplitude of oscillations of E_y .

In Figure (5.17) we show the domains of maximum positive and negative E_y in cases with guide fields $B_{y0}/B_0 = 0.25$ and 0.5 . These structures of the electric field represent cigar-like magnetized lower-hybrid modes stretched along the magnetic field lines.

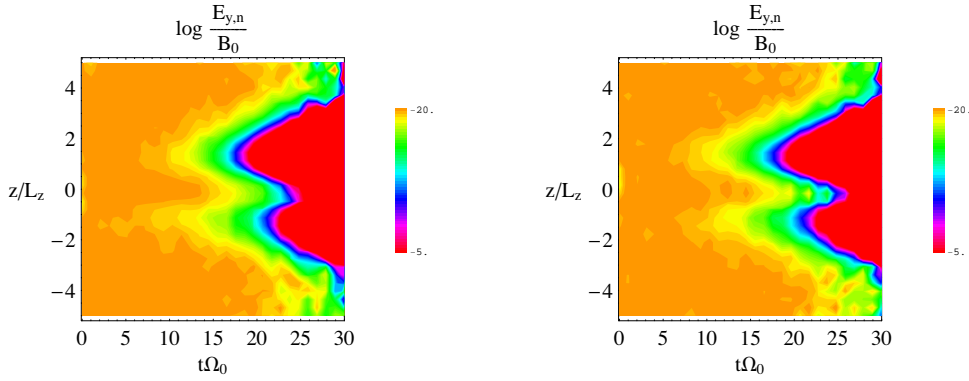


Figure 5.16: Logarithm of the most unstable Fourier modes in Y- and X-directions for $n_y = 6$ and $n_x = 4$ of E_y (left and right panels) obtained in 3D simulation with guide field $B_{y0}/B_0 = 0.5$. One sees the wave-field grow at the periphery of the current sheet and gradually penetrate to the neutral plane.

Their formation was predicted by *Tsytovich* (1995). These waves are an example of self-organizing structures in plasma due to the resonant excitation of waves by ions. The Landau resonance of these waves with electrons leads to their damping. This way the energy is transferred from the ion flow via the unstable wave to electron heating. A temporal sequence of these pictures (see our web-page <http://www.linmpi.mpg.de/~šilin/simulations>) demonstrates that the waves above and below the neutral plane drift in different directions. This way the magnetic guide field effectively "splits" the two LHD-ion resonances at the opposite edges of the sheet and, therefore, lowers the efficiency of their coupling to the global eigenmodes of the sheet (kink or sausage modes). As the wave propagation turns further away from the current-flow direction the density of resonant particles decreases, as shown in Figure (5.18), and as a result the instability grow slower.

This theoretical prediction is fully supported by our simulations results. In Figure (5.19) we show the ion (left) and electron (right) distribution functions at the edge of the current sheet. For better orientation in space we also show the direction of the local magnetic field (inclined solid line) and the cross-field wave propagation direction (the inclined dotted line). One sees a principal difference in the evolution of the ions and electrons. As we expected, contrary to the zero guide-field case shown in Figure (5.11), the peak of the resonant plateau in ion distribution appears not in the current flow direc-

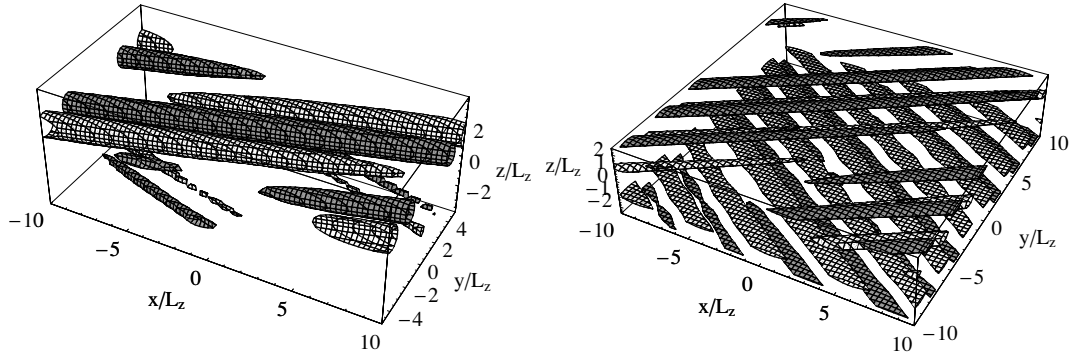


Figure 5.17: Domains of the maximum positive (white contours) and negative (grey contours) values of E_y showing the three-dimensional structure of the unstable LHD modes. The left and right panels show simulation results for the guide fields $B_{y0}/B_0 = 0.25$ and 0.5 , respectively.

tion but along the line of cross-field wave propagation. The electrons in this case remain magnetized and demonstrate slight temperature anisotropy, i.e. the width of the distribution function in the magnetic field direction gradually increases while in the perpendicular direction it remains close to the initial.

The peaks of the wave amplitudes are located at the edges of the current sheet, as in the classical Harris current sheet, with the only exception that now the wave structures are propagating at different angles to the current flow direction (see Figure (5.17)). Comparison of several simulations with different B_{y0}/B_0 ratios demonstrates that the electrostatic field domains, indeed, follow the local magnetic field directions.

Assuming that the growth rate of the instability is proportional to the density of the resonant particles, one obtains a growth rate dependence on the magnetic guide field as

$$\gamma \sim \exp\left\{-\sin^2\left(\arctan\left(\frac{B_{y0}}{B_0}\right)\right) - \left(\cos\left(\arctan\left(\frac{B_{y0}}{B_0}\right)\right) - u_i/v_w\right)^2\right\}, \quad (5.2)$$

where u_i is the ion drift velocity and v_w is the phase velocity of the fastest-growing LHD wave. This situation is schematically illustrated in Figure (5.18). Without guide field the velocity of LHD waves is directed along the Y-axis ($\theta = 0$) and the wave encounters the maximum population of resonant particles. With the increasing ratio B_{y0}/B_0 the LHD waves turn further away from the Y-axis and encounter ever smaller fractions of resonant

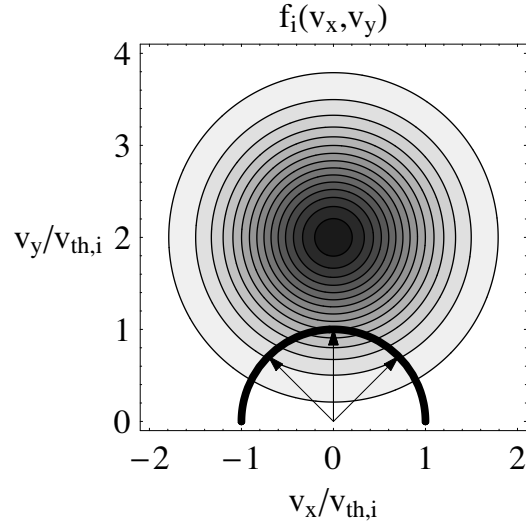


Figure 5.18: The regions of ions' resonance with the LHD waves. The shaded contours represent ion distribution function (darker area shows the density maximum) and the thick line shows the velocity of LHD for different values of local magnetic field from $-\pi/2$ to $\pi/2$ across the current sheet. For example, two inclined radius-vectors correspond to resonant velocities above and below a current sheet with a guide field $B_{y0} = B_0$.

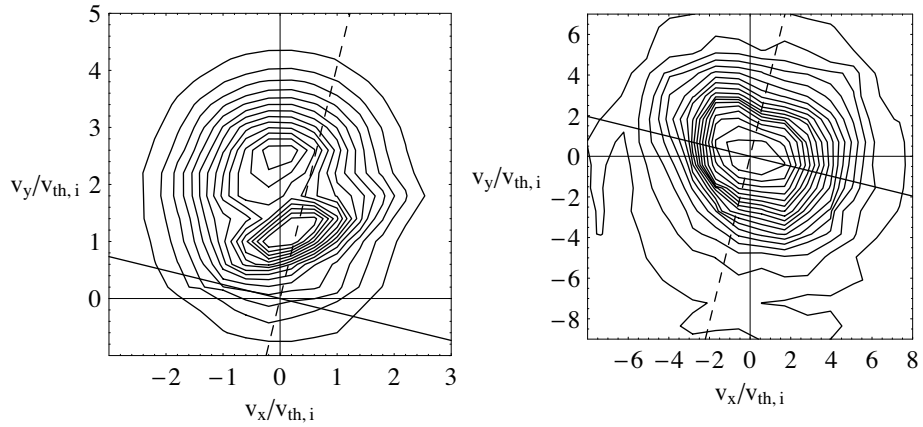


Figure 5.19: Contour plots of particle distribution functions (ions - left panel, electrons - right panel, respectively) at the upper edge of the current sheet ($z = L_z$). Result of a simulation with $B_{y0}/B_0 = 0.25$.

particles.

The deviation of Landau resonances in velocity space is also confirmed by our di-

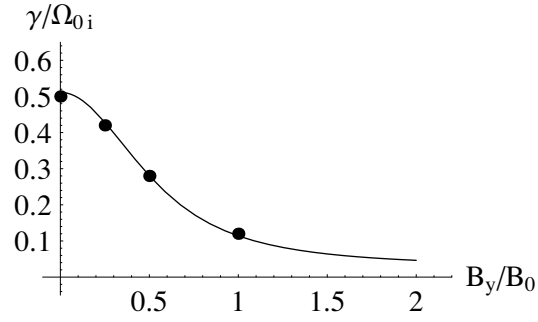


Figure 5.20: Analytical dependence of the resonant LHD waves growth on the value of magnetic guide field according to equation (5.2) for mass ratio $m_i/m_e = 16$ extrapolating from the pure DRI growth rate $\gamma_0 = 0.5\Omega_{0i}$. The solid dots show results of 3D simulations for $B_{y0}/B_0 = 0, 0.25, 0.5$ and 1.0

agnostics of resonant plateaus in the particle distribution functions (Figure (5.19)). We found that the resonant plateau in ion distribution lies exactly on the line of cross-field propagation. At the same time, the behaviour of electrons undergoes significant changes. It has been known before, that the presence of guide field can lead to the stabilization of electron tearing-mode instability by introducing a new degree of freedom in the reconnection geometry (Wiegmann and Büchner, 2002). Thus, instead of being trapped in circular orbits, electrons escape from the reconnection regions along the spiral Speiser-like orbits in the central plane along the guide field. We have observed a consequence of this escape process in our simulations. Right panel of Figure (5.19) does not show any distinct plateau in the electron distribution. Instead, one finds that electrons are anisotropically heated, i.e. the parallel temperature increases, due to electron scattering along the guide field.

For guide fields in the range $0 \leq B_{y0}/B_0 \leq 2$ we obtain a strong growth rate decrease for $B_{y0}/B_0 \sim 1$ as shown in Figure (5.20). The agreement between the theoretical curve and the results of simulations suggests that our assumption of growth rate being proportional to resonant ion density was, in fact, correct.

In the light of our results we now propose a new physical mechanism of stochastic percolation of plasma through current sheets in the presence of guide magnetic field. Although no numerical simulations found evidence for oblique drift-tearing modes pre-

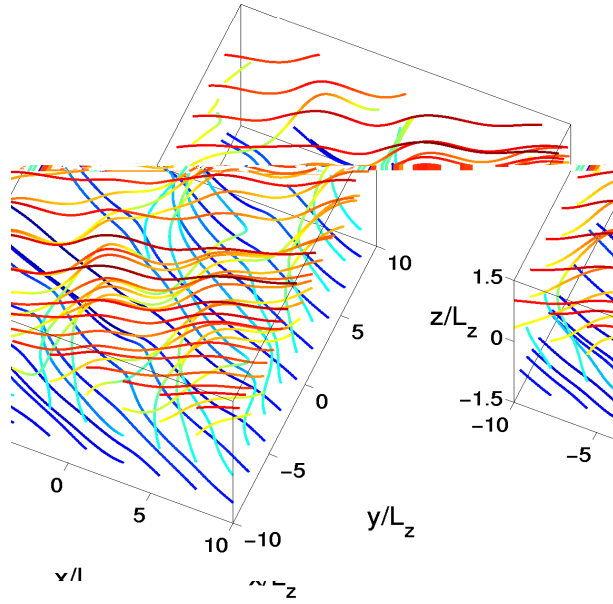


Figure 5.21: Magnetic field lines in the simulation with $B_{y0}/B_0 = 0.25$ at time $t\Omega_{0i} = 34$. The colour shows the position of the line along the Z-axis (blue - top, red - bottom).

dicted by *Galeev et al.* (1985); *Kuznetsova and Zelenyi* (1985, 1990a), we, nevertheless, observed a similar process in the course of nonlinear evolution of LHD waves. The resulting magnetic field structures are shown in Figure (5.21). Originally, all field lines are launched at the distance $\pm L_z$ from the central plane of the current sheet. Eventually, as one finds from the figure, the lines start twisting, forming spirals around their original directions, and when they reach sufficiently close to the center of the sheet they become reconnected. On the one hand, this is similar to the percolation scenario, proposed by *Kuznetsova and Zelenyi* (1990a), when different magnetic islands at different magnetic horizons start merging and eventually lead to field lines connection across the current sheet. But, on the other hand, the underlying physical process of turbulence and magnetic field chaotization found by us here is different. Although we also have a spread of drift directions and wavelengths as a function of distance from the current sheet center, the peak of the instability corresponds to the relatively short wavelengths and the growth initiates at the periphery of the current sheet, not at the center. Also, contrary to the results of *Scholer et al.* (2003) and *Pritchett and Coroniti* (2004), no classical X- or O-lines are formed, the reconnected normal fields present quite a chaotic picture in the central plane.

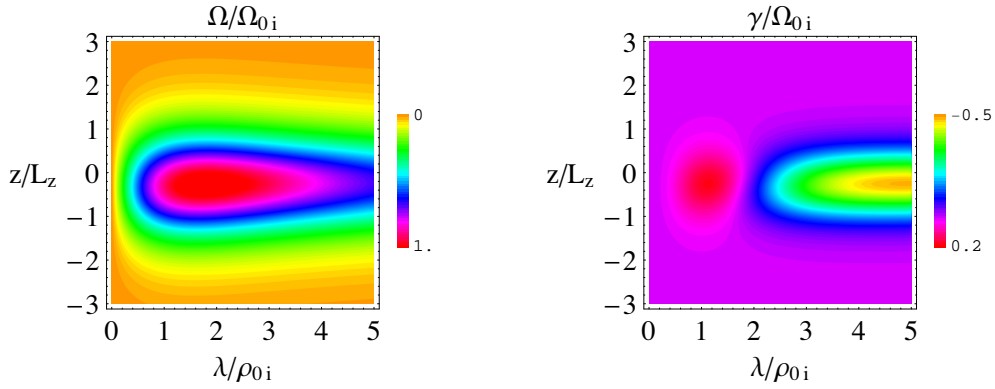


Figure 5.22: Linear dispersion relation for LHD waves at the magnetopause model described in Section (2.2): left panel - oscillation frequencies, right panel - growth rates. The asymptotic plasma betas are $\beta_{MSH} = 0.6$ and $\beta_{MSP} = 0.9$.

5.3 Magnetopause-like boundaries

As the first step, let us consider the linear dispersion relation of lower hybrid waves for the model presented in Section (2.2). Figure (5.22) demonstrates the linear dispersion relation for LHD waves derived by *Huba et al.* (1980). One sees that contrary to the symmetric current sheet case with plasma beta changing from zero to infinity, here with beta remaining everywhere close to unity the range of unstable wavelengths becomes very limited. Also, the fastest-growing wavelength is approximately two times shorter than in a symmetric Harris current sheet of the same width.

Perhaps, the most interesting feature in Figure (5.22) is the asymmetry across the $z = 0$ line, which marks the density gradient peak. One sees a distinct shift of the unstable region to the magnetosphere side (negative z region). Also, in this case there is a slight difference of wavelengths of the most-unstable modes at the opposite sides of the magnetopause. This asymmetry becomes more distinct with the increasing difference of plasma betas from the two sides of the magnetopause. Thus, one can expect that during the magnetopause transitions with plasma betas being of the same order, the wavelet analysis should give almost constant estimate of LHD wavelength, while in the presence of strong changes in plasma beta, the wavelength of the dominant LHD mode must significantly change, as follows from Figure (5.23). It is not a rare case, that plasma beta changes

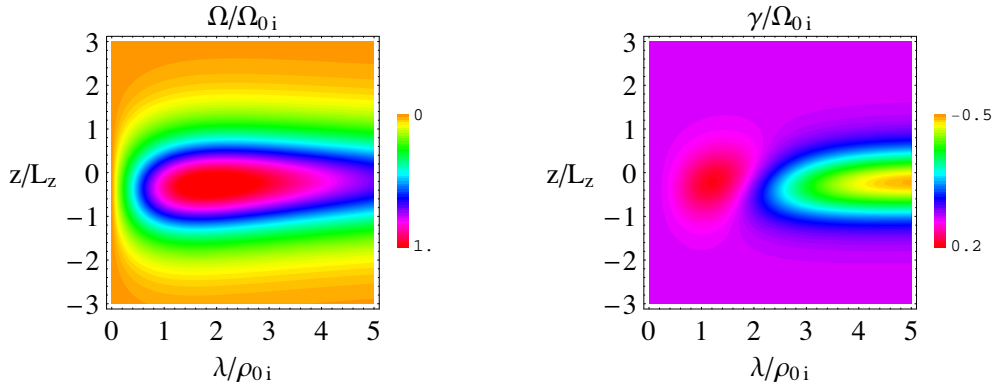


Figure 5.23: Same as in Figure (5.22) but for asymptotic plasma betas $\beta_{MSH} = 0.6$ and $\beta_{MSP} = 2.5$.

during a magnetopause crossing by a factor of 10, as was observed by Cluster, e.g., on 15.02.2002 at 23:37 - 23:43 or on 11.02.2002 at 4:00 (*Panov (2004)*).

In order to investigate the evolution of tangential discontinuities at the magnetopause we carried out Vlasov-code simulations with various asymptotic plasma betas from the opposite sides of the interface and with different total angles of magnetic field rotation in the magnetopause plane. For all simulated cases the typical scale of density gradient in the Z-direction and thus current sheet layer L_z was equal to one ion gyroradius from the magnetospheric side. The particle mass and temperature ratios were chosen as $m_i/m_e = 16$ and $T_i/T_e = 6$. The asymptotic value of plasma betas in magnetosphere and in the magnetosheath were selected as $\beta_{MSP} = 0.9, 1.5, 2.5$ and $\beta_{MSH} = 0.6$, respectively. The total angle of magnetic field rotation in the XY-plane through the magnetopause was varied from $\pi/2$ to π radians.

Numerical simulations confirm the linear theory prediction and in-situ observations concerning the region of electrostatic wave activity maximum being shifted to the Earthward side of the density ramp. Figure (5.24) demonstrates an example which was obtained in a simulation with magnetic field rotation $\Theta = \pi$. First, the E_y arises at the magnetospheric side of the density gradient. Then, it penetrates towards the magnetosheath side and in the region near $z = 0$ the dominant field is E_x . This is an expected result, since near $z = 0$ the magnetic field is directed along y-axis, and thus the electric field remains quasi-perpendicular to the magnetic field.

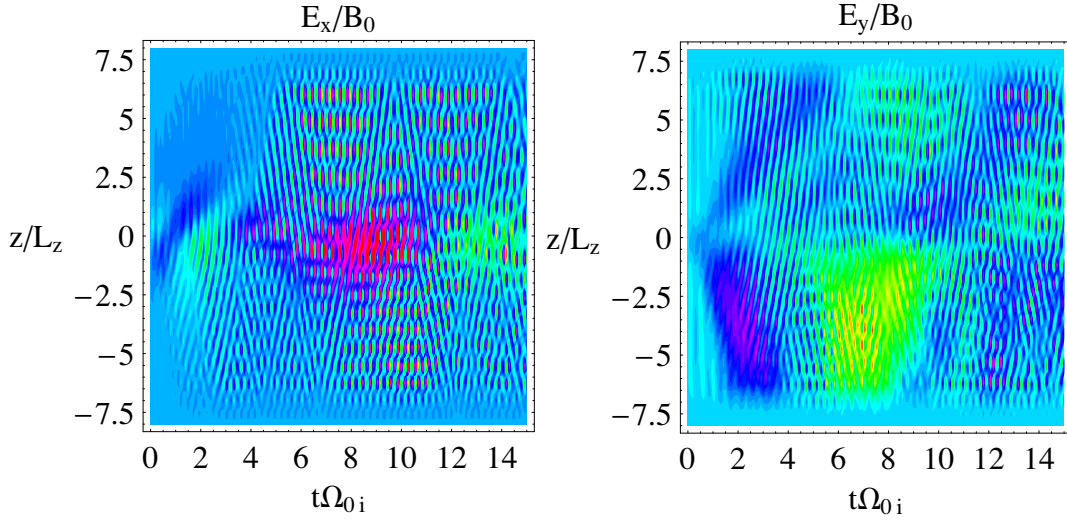


Figure 5.24: Evolution of electric field components E_x (left) and E_y (right) across the magnetopause in time interval $t\Omega_{0i} = 0 - 15$. Result of simulation with asymptotic plasma betas 0.6 and 2.5 and rotation angle $\Theta = \pi$.

At the same time, the amplitude of normal magnetic field B_z fluctuations is either stronger to the magnetosheath side or practically equal everywhere. However, the origin of these fluctuations is also LHD waves. One sees that the magnetic field fluctuations have a much smaller amplitude than the electric field (the mode is quasi-electrostatic) but they have the same wavelength and arise in the same region as the initial electrostatic perturbations.

The confirmation of LHD waves cross-field orientation is demonstrated in Figure (5.25). We calculate the angle between electric and magnetic fields in a simulation with total rotation angle $\Theta = \pi$. At the edges of the box, along the z -axis, the magnetic field is directed along the X -axis, and there E_y component of LHD wave should be much larger than the E_x component. In the central region, the magnetic field is predominantly oriented in the y -direction and E_x should prevail there. This theoretical expectation is confirmed. The sporadic peaks in both plots in Figure (5.25) are due to E approaching zero.

As a result of the LHD excitation, we see characteristic perturbations in the particle distributions which can be attributed to resonance with lower hybrid waves, similarly to the symmetric Harris-type current sheets (see Figure (5.26)). The main difference

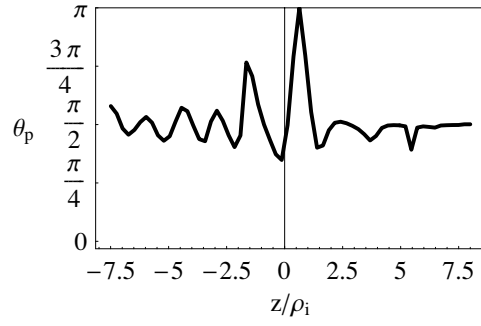


Figure 5.25: Angle between electric and magnetic fields $\theta_p = \arccos((\mathbf{B} \cdot \mathbf{E})/(B \cdot E))$. Result of simulation with asymptotic plasma betas 0.6 and 2.5 and rotation angle $\Theta = \pi$.

from the Harris current sheet is that the propagation direction changes with the distance from the magnetopause (sometimes called magnetic horizons) in accordance with the normal to the local magnetic field direction. This leads to loss of coherence of wave-particle interactions. When a particle performs gyro-motion across the magnetic field it crosses different magnetic horizons and at each horizon it experiences electrostatic field with different orientation. In combination with wave asymmetry due to large plasma beta gradients this effectively leads to particle scattering in the velocity space and the efficiency of resonant Landau damping interactions decreases. Thus, even despite a relatively strong electrostatic fields we do not observe any significant particle heating, compared to the symmetric current sheet simulations.

In all simulations which continued for about 10 ion gyroperiods (with $\Theta = \pi/2$, $2/3\pi$, $3/4\pi$ and π) we observed that in the late non-linear phase longer waves started to dominate due to some coalescence process. The transition is very clear: we show a sequence of three snapshots of normal magnetic field B_z from one simulation with $\Theta = \pi$ and plasma betas 0.6 and 2.5 in the magnetosheath and magnetopause, respectively (see Figure (5.27)).

We present here two limiting cases - with $\Theta = \pi/2$ and $\theta = \pi$ (Figure (5.28)). In the first case with perpendicular asymptotic magnetic fields the wave profile appears in the XZ-plane and it is shifted to the magnetospheric side. In the second case with anti-parallel asymptotic fields the wave is seen in the YZ plane and is shifted to the magnetosheath side. It must be noted, that although the asymptotic antiparallel fields are aligned along X axis,

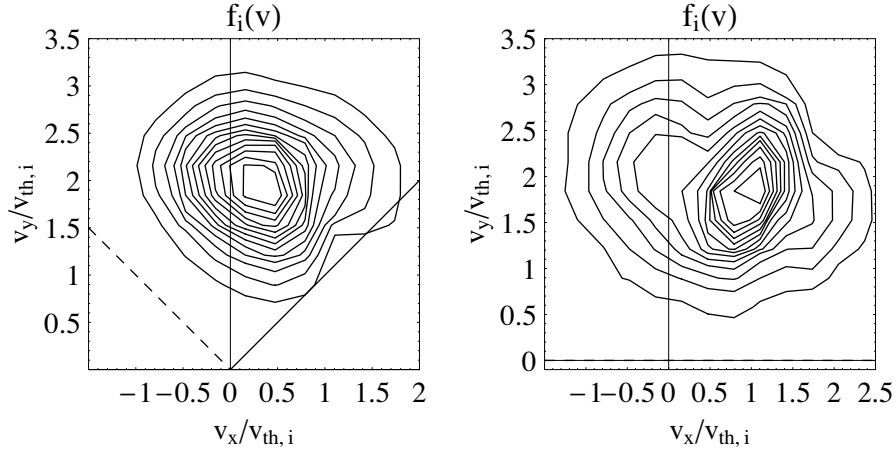


Figure 5.26: Deformations of ion distribution functions at $t\Omega_{0i} = 6$ at the magnetosheath (left) and at the magnetospheric (right) sides of the magnetopause. In the left plot the dashed line marks local magnetic field and the normal solid line corresponds to the cross-field propagation direction. In the right plot the cross-field propagation approximately corresponds to the vertical line. Result of simulation with asymptotic plasma betas 0.6 and 0.9 and rotation angle $\Theta = 3/4\pi$.

local magnetic fields near the magnetopause are predominantly in the Y-direction. Also, the wave appears to be a standing one, there is no significant drift. Whether this long wave can be compared to classical aperiodic tearing-mode is not clear, but there is certain resemblance.

Perhaps the main reason why we obtain tearing-type instabilities, although previous theories and simulations suggest that these modes should be strongly suppressed by the B_y field (see e.g. *Kuznetsova et al. (1994)*; *Nakamura and Scholer (2000)*; *Swisdak et al. (2003)*), is that in the previous models B_y was introduced as a current-aligned component on top of the antiparallel magnetic field reversal. This effectively led to particle drift being almost aligned with magnetic fields. In our model, on the contrary, the particle drift velocities keep approximately normal to the local magnetic field at all magnetic horizons. This makes the configuration linearly unstable against the lower-hybrid waves as well as provides efficient Landau damping necessary for the tearing-mode instability. Also, from the point of view of wave-particle resonances, it is logical that the longer waves should eventually prevail in this system. Since the gyrating particles move between different

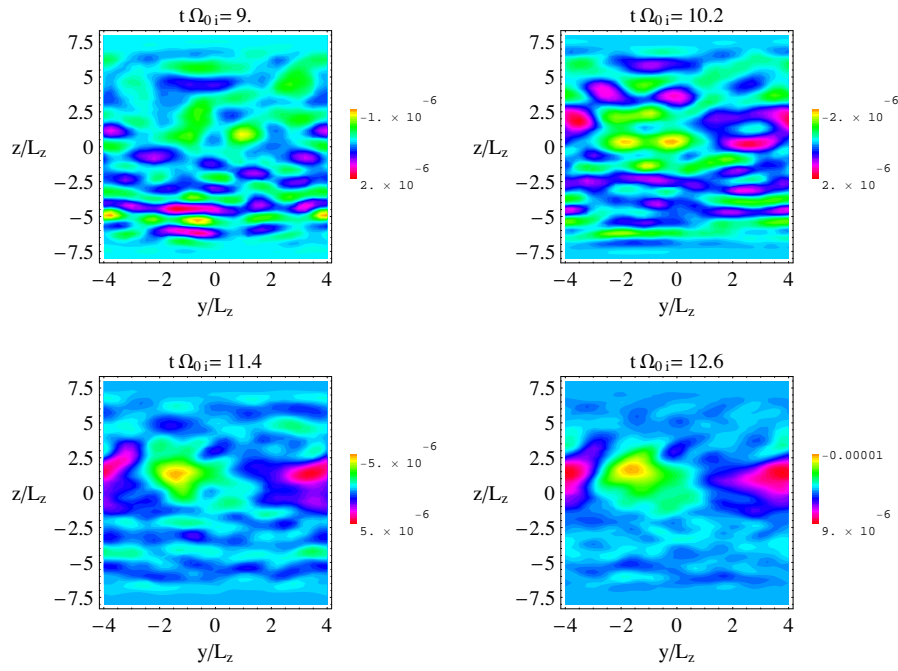


Figure 5.27: Coalescence of short lower hybrid waves and formation of the long-wavelength mode (as seen in normal magnetic field B_z fluctuations). Result of simulation with asymptotic plasma betas 0.6 and 2.5 and rotation angle $\Theta = \pi$.

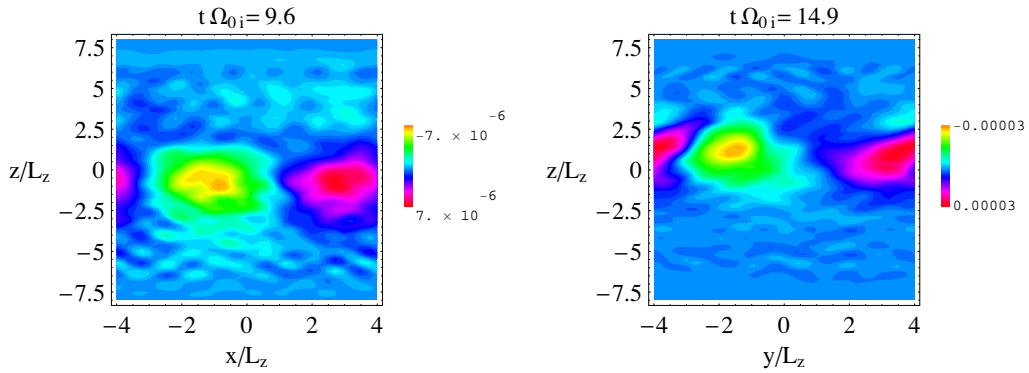


Figure 5.28: Long-wavelength perturbations of normal magnetic field B_z . Results of simulations with rotation angle $\Theta = \pi/2$ (left) and $\Theta = \pi$ (right).

magnetic horizons they experience small scale electrostatic fields of lower-hybrid waves of different orientation but the interaction time is too short for any coherent structure to form from such random interactions. When, however, a longer wave forms, particle travel

time in its domain increases and the interaction becomes more efficient.

5.4 Comparison of simulation results with space experiments

Our linear kinetic theory and numerical Vlasov-code simulations have demonstrated that among the variety of possible instabilities of thin current sheets the particularly fast and common one is the lower-hybrid drift instability (LHDI), associated with lower-hybrid (LH) waves. Luckily, LH waves are also relatively well investigated by spacecraft in the Earth magnetosphere, because they are encountered everywhere near plasma density gradients and contrary to the long waves, like tearing, KHI or kink/sausage modes, LH waves do not require non-local multi-point analysis for their identification. That is why we would concentrate on the comparison of properties of LH waves found in our simulations with those observed in-situ and avoid speculative discussions about the origin and structure of reconnection in general, since at present no appropriate experimental techniques exist to answer this question.

At present, the theoretical and simulational results concerning the activity of LHD waves in magnetospheric tail are more numerous and advanced than laboratory experiments or spacecraft in-situ observations. Perhaps the first observations of LH turbulence in magnetotail were carried out by *Gurnett et al.* (1976) using the IMP 8 spacecraft. It was discovered, that the most common wave type was electrostatic broadband noise with frequencies from approximately 10 Hz to few kHz. It occurred practically everywhere but was particularly active near magnetic field gradients at plasmashet edges. The electric field of the wave was always perpendicular to the local magnetic field. Because the linear theory of LH waves still was not established at that time the authors could not explicitly prescribe their observations to this mode and instead tried to draw comparisons with other plasma waves known at that time.

Using the electric and magnetic field measurements of ISEE 1 and ISEE 2 *Gurnett et al.* (1979) investigated the waves at the magnetopause. By comparison of signals received by 215 m antenna on ISEE 1 and 30 m antenna on ISEE 2 spacecraft it was

shown, that the wavelengths of the low-frequency waves (below 10 kHz) are significantly larger than typical antenna length. Comparison between magnetic and electric fluctuations showed that the part of the spectrum with frequencies ~ 1 kHz is nearly electromagnetic and is most probably generated by whistler modes. However, waves with frequencies of the order of 10 Hz have a strong electrostatic component. Two possible instabilities were named which could account for the observed electrostatic turbulence - ion cyclotron and lower-hybrid. However, even taking into account the Doppler shift effects, very high harmonics of ion cyclotron mode have to be excited in order to produce continuous wave spectrum. That is why lower-hybrid waves seem to be more plausible explanation.

Another observation of lower-hybrid waves at the magnetopause was made by Equator-S spacecraft (see e.g. *Lucek et al.* (2001)). The authors analysed magnetic fields during several "smooth" magnetopause crossings with the aim to identify small-scale structures predicted theoretically by *Shapiro et al.* (1994) and in simulations of *Gary and Sgro* (1990). Similar to the previous experiments of ISEE 1 and 2, sub-km scales were not observed. As far as typical LH wavelengths are concerned, the predictions of linear theory and simulations point not to the sub-km scales, but rather 10 - 100 km, i.e. there seems to be no disagreement with observations. The regions of strongest wave activity were usually located at the magnetospheric side of the magnetopause. A new interesting result was obtained by comparison of field-aligned and transverse power of the turbulence. It turned out, that for frequencies below 10 Hz the power of transverse waves was almost an order of magnitude higher than that of the field-aligned ones, while above that frequency they became practically equal. Besides, the energy density increased towards the lower-frequency range of the spectrum, which could mean that longer waves are more favourable and some cascading effect, similar to the one found in our simulations can take place. Also, our simulations showed that the turbulence is primarily electrostatic and transverse.

A comprehensive study of LH waves at the magnetopause was carried out by *André et al.* (2001). They analysed electric and magnetic field data from Electric Field and Wave (EFW) instrument and STAFF and FGM instruments on all four Cluster spacecraft. It was discovered, that electric fields in the lower-hybrid frequency domain near 10 Hz can have amplitudes of up to 5 mV/m. They are persistent feature at all magnetopause crossings

and occur at the Earthward side of the magnetopause on the scales of several hundred kilometers, i.e. comparable to ion gyroradius. At the same time, relevant magnetic field fluctuations were observed also at the magnetosheath side of the density ramp. In fact, our simulations showed, that quasi-electrostatic perturbations first arise on the magnetospheric side of the density gradient, but later penetrate also to the magnetosheath side, i.e. the electromagnetic perturbations in the magnetosheath can be induced by the LH waves from the magnetosphere.

Based on electric and magnetic field and plasma measurements on Polar spacecraft, *Bale et al.* (2002) investigated lower hybrid waves at the reconnecting magnetopause. Large amplitude electrostatic fields (~ 10 mV/m) were found at the edges of the current layer. The polarization of the electric field was almost perfectly perpendicular to the magnetic field. At the center of the reconnection region, where plasma beta was large the instability was quenched. The authors extrapolated their observations to the corresponding Harris current sheet and tried to analytically derive the contribution of LH waves to anomalous resistivity in the reconnection region. According to their estimates it was negligible and thus it was concluded that LH waves could not play any significant role in reconnection. However, the authors remarked that the intensity of LH waves could be underestimated in their experiment due to instrumental limitations and also that recent numerical simulations suggested that theoretical estimates of wave contribution to anomalous resistivity could be several orders of magnitude too low.

Recently *Vaivads et al.* (2004) and *André et al.* (2004) analysed one magnetopause crossing by Cluster spacecraft at 2002-02-06 0811:57. They found, a thin current layer with a thickness of the order of several electron gyroradii near the magnetopause. The activity of LH waves was confined to vicinity of this thin current layer. Thus, the authors concluded that LH turbulence does not play any significant role for the global processes at the magnetopause. However, there are several ambiguities in this work. Firstly, the magnetopause location and its normal were obtained by the time-delays between the density-gradient detection by different spacecraft. The authors did not mention about checking deHoffmann-Teller frame or Walen relation. Later tests with Cluster magnetic field and plasma measurements showed that, in fact, the moment considered in this work corresponded rather to an FTE at an open magnetopause and then a tangential magnetopause

crossing followed 5 minutes later, at 0817:00 (*Panov (2004)*). Secondly, the magnetic field normal had large x- and y-components, which was rather far from the expected direction, and the thin current sheet was "not completely flat and aligned with the magnetopause plane" (see *André et al. (2004)*). In the frame calculated by magnetic field variance method for this event, which coincided with the Tsyganenko model estimate, there is a strong normal magnetic field and it is logical to expect a strong flux across the imaginary magnetopause plane in the earthward direction.

Chapter 6

Summary of the main results

In this work we tried to clarify the role of kinetic effects in the process of magnetic reconnection through thin collisionless current sheets. For our investigations we developed a linear perturbation theory and a numerical simulation method. The linear theory was aimed in particular at linear symmetric sausage-modes of symmetric current sheets, while numerical simulations had to clarify the possible nonlinear interactions of different plasma instabilities in current sheets. The results obtained by these two methods are now summarized.

Although the linear perturbation theory failed to find unstable global sausage-modes in thin current sheets, it revealed several important aspects. We found that the long-wave approximation, in fact, leads away from the fastest-growing waves which evolve in current sheets. This shows the importance of correct scaling of instability properties with particle mass ratio used in numerical simulations. For example, an instability with a wavelength $\lambda = 10\rho_{0i}$ found in simulations with $m_i/m_e = 16$ would have a wavelength of only $\lambda = 1\rho_{0i}$ for $m_i/m_e = 100$. This explains the paradox of stabilization of linear current-aligned kink instabilities predicted by *Daughton* (1998, 1999a,b) which, nevertheless, were obtained in simulations (e.g. by *Lapenta and Brackbill* (1997); *Büchner and Kuska* (1998); *Horiuchi and Sato* (1999)). The fastest-growing wavenumber is proportional to the $(m_i/m_e)^{1/2}$ and the long-wavelength approximation is only valid for small particle mass ratios. Another consequence of the linear theory is the confirmation of validity of averaged particle motion first used by *Dobrowolny* (1968) and later by *Lapenta and*

Brackbill (1997). Indeed, using the same approximate approach we managed to obtain a result which is very close to the one obtained by far more sophisticated calculations of *Daughton* (1998) for anti-symmetric modes. By including and excluding the electrostatic perturbations from our dispersion relation, we demonstrated that it is the electrostatic interactions which stabilize the long-wavelength eigen oscillations of current sheets. At the same time, we showed that the tearing-mode instability is fully electromagnetic.

Our new simulation technique, using particle distribution functions instead of fluid or super-particles allowed detailed description of collective kinetic phenomena, which were either neglected or underestimated in the previous numerical simulations. Although the use of six-dimensional phase space posed large demands on computer memory and computing time, we managed to parallelize the program and execute it in a rational way on parallel machines, so that one production run took at most 48 hours.

The main unexpected result of our simulations is that in symmetric mono-dimensional current sheets the lower-hybrid drift (LHD) waves get in a strong Landau-type resonance with the ion flow. As these waves grow in amplitude, they also penetrate to the current sheet center and couple to the global eigen-mode oscillations of the current sheet. The resulting global instability (we proposed to call it drift-resonant instability (DRI)) has wavelength and oscillation frequency proportional to hybrid ion-electron scales $\lambda \sim \rho_{0i}(m_e/m_i)^{1/2}$ and $\Omega \sim (\Omega_{0i}\Omega_{0e})^{1/2}$, while its growth rate scales with ion gyrofrequency $\gamma \sim \Omega_{0i}$. The reason for this scaling has a clear physical explanation: the instability is initiated by charge separation effects near the plasma density gradients, while in the late nonlinear regime its growth is governed by the resonant interaction with thermal ions.

We observed the direct coupling of current-aligned instabilities with aperiodic tearing-mode, which can explain the fast onset of reconnection in thin current sheets. According to our results, even if the tearing-mode is relatively strong in the beginning of simulation, its growth rate is always smaller than that of current-aligned modes. After a certain time, which strongly depends on the current sheet thickness and the initial perturbation, the wave-mode eventually reaches higher amplitude than tearing and they both continue to grow further at the high growth rate.

Our simulations clarified the stabilizing effect of current-aligned magnetic guide field

in thin current sheets. The diagnostics of electrostatic fields showed the persistent self-organized structures of LHD drifting across the magnetic field. The shift of resonant plateau in ion distribution functions in accordance with cross-field propagation direction demonstrated the principle of instability stabilization through the weakening of ion-LHD Landau resonance.

We proposed a new physical explanation for stochastic percolation through thin current sheets in the presence of guide magnetic field. Instead of oblique drift-tearing modes predicted by analysis of *Galeev et al. (1985); Kuznetsova and Zelenyi (1985, 1990a)* we found that the LHD waves, which propagate across local magnetic fields and penetrate to the current sheet center, lead to chaotic pattern in reconnected magnetic fields. The field lines, initially parallel to the current sheet plane, with time start winding around the original direction and form spirals, reaching to the center of the current sheet and to the periphery. This eventually allows plasma diffusion through the current sheet and could account for flux-transfer events (FTE's) at the magnetopause.

We have developed an analytical model of tangential discontinuity typical for Earth magnetopause, as observed by ISEE 1 and 2 and Cluster spacecraft. The linear dispersion relation and numerical simulations of this model predict strong activity of short lower-hybrid waves at the magnetospheric side of the density gradient region. We found, that in case of large plasma beta differences from the magnetosheath and magnetosphere sides there is a significant asymmetry in wave properties. Some weak traces of resonant interaction of LHD waves with particles exist, but due to magnetic field rotation the LHD waves at different magnetic horizons are incoherent and Landau damping is saturated. Thus, we do not find any stochastic percolation like in the symmetric current sheets with guide magnetic field. With time, the short-wavelength LHD modes trigger longer tearing-type waves through some kind of cascading or coalescence process similar to the one predicted by *Gary and Sgro (1990)*. Probably the key reason for lower-hybrid and tearing modes stabilization found in previous works and not found by us appears to be the particle drift profile. While in previous studies the B_y field was imposed over a mono-dimensional current sheet, the particle drift was getting field-aligned, in our model the particle drift velocities remain quasi-perpendicular to local magnetic fields, which is the main condition for lower-hybrid waves excitation, as well as for efficient Landau damping mechanism

of tearing-mode instability. Another result of our investigation is that there seems to be no strong dependence of reconnection through the magnetopause on the magnetic field rotation angle, which suggests that "component reconnection" is possible.

Our simulations are in agreement with the existing experimental knowledge about small-scale instabilities and waves in thin current sheets encountered in Earth magnetosphere. We verified that lower-hybrid waves are excited at the Earthward side of the magnetopause. In accordance with Cluster observations the electrostatic perturbations are strongest at the Earthward side of the density gradient, while corresponding magnetic perturbations penetrate further to the magnetosheath. Also, in agreement with observations of Cluster and Equator-S missions, we see that the electrostatic waves are primarily transverse to the local magnetic field.

Unfortunately, not much can be said in connection with the Earth magnetotail. Firstly, because the current sheet in the tail is typically much thicker than ion gyroradius and as we showed the LHD waves there do not influence the global dynamics directly - they are weak and located too far from the neutral plane. Secondly, most of the effort in experiments has been invested so far in investigation of global structure and dynamics of the current sheet, e.g. *Sergeev et al. (2004)*. But the general properties observed in-situ, e.g. by IMP 8 spacecraft, - cross-field propagating quasi-electrostatic mode located at the plasma sheet boundaries - have been confirmed in our simulations.

It must be mentioned, that our results do not render other recent theories or simulations invalid (e.g. *Lapenta et al. (2003)*; *Karimabadi et al. (2003a,b)*). In our simulations we observe the scattering of particles in the phase space and formation of nonlinear resonant plateaus in the course of interaction with LHD, which can be compared also to the streaming secondary ion population or stationary plasma background. At this stage the arguments of *Lapenta et al. (2003)*; *Karimabadi et al. (2003a,b)* become valid: the tangential velocity discontinuity or relative ion-ion streaming come into play and can lead to the longer-wavelength instabilities, such as Kelvin-Helmholtz or ion-ion kink instability. However, we emphasize that all these processes take place after the resonant instability discussed in this work, since they are much slower.

Bibliography

André, M., A. Vaivads, S. C. Buchert, A. N. Fazakerley, and A. Lahiff (2004), Thin electron-scale layers at the magnetopause, *Geophys. Res. Lett.*, *31*, L03,803.

André, M., et al. (2001), Multi-spacecraft observations of broadband waves near the lower hybrid frequency at the earthward edge of the magnetopause, *Ann. Geophysicae*, *19*, 1471 – 1481.

Bale, S. D., F. S. Mozer, and T. Phan (2002), Observation of lower hybrid drift instability in the diffusion region at a reconnecting magnetopause, *Geophys. Res. Lett.*, *29*, 2180.

Bieber, J. W., E. C. Stone, E. W. Hones, D. N. Baker, S. J. Bame, and R. P. Lepping (1984), Geospace environmental modelling (gem) magnetic reconnection challenge, *J. Geophys. Res.*, *89*, 6705.

Birdsall, C. K., and A. B. Langdon (1991), *Plasma Physics via Computer Simulation*, Adam Hilger, Bristol, Philadelphia and New York.

Birn, J., and M. Hesse (1994), Particle acceleration in the dynamic magnetotail: Orbits in self-consistent three-dimensional mhd fields, *J. Geophys. Res.*, *99*, 109.

Birn, J., et al. (2001), Geospace environmental modelling (gem) magnetic reconnection challenge, *J. Geophys. Res.*, *106*, 3715.

Büchner, J., and J.-P. Kuska (1996), "Three-dimensional collisionless reconnection through thin current sheets: theory and selfconsistent simulations" in *Proceedings of the IIIrd International Conference on Substorms (ICS-3)*, edited by E. J. Rolfe and B. Kaldeich, 373 pp., ESA Publications Division, Noordwijk, The Netherlands.

- Büchner, J., and J.-P. Kuska (1998), *Magnetospheric Research with Advanced Techniques, Proceedings of the 9th Committee on Space Research Colloquium*, edited by R. L. Xu and A. T. Y. Lui, 179 pp., Elsevier Science, Amsterdam.
- Büchner, J., and J.-P. Kuska (1999), Sausage mode instability of thin current sheets as a cause of magnetospheric substorms, *Ann. Geophysicae*, *17*, 604.
- Bulanov, S. V., and S. I. Syrovatskyi (1974), *Proceedings of P. N. Lebedev Physics Institute, Academy of Sciences of USSR*, 88 (in Russian) pp., Nauka Publishers, Moscow.
- Bulanov, S. V., E. Y. Echkina, I. N. Inovenkov, and F. Pegoraro (2002), Current sheet formation in three-dimensional magnetic configurations, *Phys. Plasmas*, *9*, 3835.
- Buneman, O. (1958), Instability, turbulence and conductivity in a current carrying plasma, *Phys. Rev. Lett*, *1*, 8.
- Coppi, B., G. Laval, and R. Pellat (1966), Dynamics of the geomagnetic tail, *Phys. Rev. Lett.*, *16*, 1207.
- Daughton, W. (1998), Kinetic theory of the drift kink instability in a current sheet, *J. Geophys. Res.*, *103*, 29,429.
- Daughton, W. (1999a), The unstable eigenmodes of a neutral sheet, *Phys. Plasmas.*, *6*, 1329.
- Daughton, W. (1999b), Two-fluid theory of the drift-kink instability, *J. Geophys. Res.*, *104*, 28,701.
- Daughton, W. (2002), Nonlinear dynamics of thin current sheets, *Phys. Plasmas.*, *9*, 3668.
- Davidson, R. C., and N. T. Gladd (1975), Anomalous transport properties associated with the lower-hybrid-drift instability, *Phys. Fluids*, *18*, 1327.
- Davidson, R. C., and N. A. Krall (1977), Anomalous transport in high-temperature plasmas with applications to solenoidal fusion systems, *Nuclear Fusion*, *17*, 1313.

- Davidson, R. C., N. T. Gladd, C. S. Wu, and J. D. Huba (1976), Influence of finite- β effects on the lower-hybrid-drift instability in post-implosion θ pinches, *Phys. Rev. Lett.*, *37*, 750.
- De Keyser, J., and M. Roth (1997), Equilibrium conditions for the tangential discontinuity magnetopause, *J. Geophys. Res.*, *102*, 9513 – 9530.
- De Keyser, J., and M. Roth (1998), Equilibrium conditions and magnetic field rotation at the tangential discontinuity magnetopause, *J. Geophys. Res.*, *103*, 6653 – 6662.
- Dmitruk, P., W. H. Matthaeus, L. J. Milano, S. Oughton, G. P. Zank, and D. J. Mullan (2002), Coronal heating due to low-frequency wave driven turbulence, *Astrophys. J.*, *575*, 571.
- Dobrowolny, M. (1968), Instability of neutral sheet, *Il Nuovo Cimento*, *LV*, 427.
- Drake, J. F., M. Swisdak, C. Catell, M. A. Shay, B. N. Rogers, and A. Zeiler (2003), Formation of electron holes and particle energization during magnetic reconnection, *Science*, *299* (5608), 873–877.
- Dungey, J. W. (1961), Interplanetary magnetic field and auroral zones, *Phys. Rev. Lett.*, *6*, 47–48.
- Dungey, J. W. (1963), "The structure of the exosphere or adventures in velocity space", in *GEOPHYSICS: THE EARTH'S ENVIRONMENT*, edited by C. Dewitt, J. Hieblot and A. Lebeau, 505-550 pp., Gordon and Breach, New York.
- Galeev, A., and L. Zelenyi (1976), Tearing instability in plasma configurations, *Sov. Phys. JETP, Engl. Transl.*, *43*, 1113.
- Galeev, A. A., L. M. Zelenyi, and M. M. Kuznetsova (1985), Nonlinear drift tearing mode: Hard onset and stabilization mechanisms, *JETP Lett.*, *41*, 387.
- Gary, S. P., and A. G. Sgro (1990), The lower hybrid drift instability at the magnetopause, *Geophys. Res. Lett.*, *17*, 909 – 912.

- Génot, V., F. Mottez, G. Fruit, P. Louarn, J. A. Sauvaud, and A. Balogh (2003), Bifurcated current sheets: Model and cluster observations, *submitted to Planetary and Space Science, private communication*.
- Gosling, J. T., J. R. Asbridge, S. J. Bame, W. C. Feldman, G. Pashmann, N. Skopke, and C. T. Russell (1982), Evidence for quasi-stationary reconnection at the dayside magnetopause, *J. Geophys. Res.*, *87*, 2147 – 2158.
- Greenly, J. B., and B. U. Ö. Sonnerup (1981), Tearing modes at the magnetopause, *J. Geophys. Res.*, *86*, 1305 – 1312.
- Gurnett, D. A., L. A. Frank, and R. P. Lepping (1976), Plasma waves in the distant magnetotail, *J. Geophys. Res.*, *81*, 6059.
- Gurnett, D. A., R. R. Anderson, B. T. Tsurutani, E. J. Smith, G. Paschmann, G. Haerendell, S. J. Bane, and C. T. Russell (1979), Plasma waves at the magnetopause: Observations from isee 1 and 2, *J. Geophys. Res.*, *84*, 7043 – 7058.
- Harris, E. G. (1962), On a plasma sheath separating regions of oppositely directed magnetic field, *Il Nuovo Cimento*, *XXIII*, 115.
- Hesse, M., D. Winske, J. Birn, and M. Kuznetsova (1998), "Predictions and explanations of plasma sheet dissipation processes: current sheet kinking" in *SUBSTORMS-4 edited by S. Kokubun and Y. Kamide*, 437 pp., Terra Scientific Publishing Company / Kluwer Academic Publishers, Tokio, Amsterdam.
- Hockney, R. W., and J. W. Eastwood (1988), *Computer Simulation Using Particles*, Adam Hilger, Bristol and Philadelphia.
- Horiuchi, R., and T. Sato (1999), Three-dimensional particle simulation of plasma instabilities and collisionless reconnection in a current sheet, *Phys. Plasmas*, *6*, 4565.
- Hoshino, M. (1987), The electrostatic effect for the collisionless tearing mode, *J. Geophys. Res.*, *92*, 7368 – 7380.

- Huba, J. D., N. T. Gladd, and K. Papandopoulos (1977), The lower-hybrid-drift instability as a source of anomalous resistivity for magnetic field line reconnection, *Geoph. Res. Lett.*, *4*, 125.
- Huba, J. D., N. T. Gladd, and K. Papandopoulos (1978), Lower-hybrid-drift wave turbulence in the distant magnetotail, *J. Geophys. Res.*, *83*, 5217.
- Huba, J. D., J. F. Drake, and N. T. Gladd (1980), Lower-hybrid-drift instability in field reversed plasmas, *Phys. Fluids*, *23*(3), 552.
- Karimabadi, H., W. Daughton, P. L. Pritchett, and D. Krauss-Varban (2003a), Ion-ion kink instability in the magnetotail: 1. linear theory, *J. Geophys. Res.*, *108*, SMP 10.
- Karimabadi, H., P. L. Pritchett, W. Daughton, and D. Krauss-Varban (2003b), Ion-ion kink instability in the magnetotail: 2. three-dimensional full particle and hybrid simulations and comparison with observations, *J. Geophys. Res.*, *108*, SMP 11.
- Kim, K.-H., N. Lin, C. A. Catell, Y. Song, and D.-H. Lee (2002), Evidence for component merging near the subsolar magnetopause: Geotail observations, *Geophys. Res. Lett.*, *29*, 1080.
- Kobak, T., and M. Ostrowski (2000), Energetic particle acceleration in a three dimensional magnetic field reconnection model: the role of magnetohydrodynamic turbulence, *MNRAS*, *317*, 973.
- Krall, N. A., and P. C. Liewer (1971), Low-frequency instabilities in magnetic pulses, *Phys. Review*, *4*, 2094.
- Krall, N. A., and A. W. Trievelpiece (1973), *Principles of plasma physics*, 674 pp., McGraw-Hill book company, New York.
- Kusano, K. (2001), Three-dimensional simulation study of magnetic reconnection in the solar corona, *EARTH PLANETS SPACE*, *53*, 491–494.
- Kuznetsova, M. M., and M. Roth (1995), Thresholds for magnetic percolation through the magnetopause current layer in asymmetrical magnetic fields, *J. Geophys. Res.*, *100*, 155 – 174.

- Kuznetsova, M. M., and L. M. Zelenyi (1985), Stability and structure of the perturbations of the magnetic surfaces in the magnetic transitional layer, *Plasma Phys. and Controlled Fusion*, 27, 363.
- Kuznetsova, M. M., and L. M. Zelenyi (1990a), Nonlinear evolution of magnetic island in a sheared magnetic field with uniform plasma background, *Plasma Phys. and Controlled Fusion*, 32, 1183.
- Kuznetsova, M. M., and L. M. Zelenyi (1990b), The theory of the stochastic percolation model, *Geophys. Monograph*, 58, 473.
- Kuznetsova, M. M., M. Roth, Z. Wang, and M. Ashour-Abdalla (1994), Effect of the relative flow velocity on the structure and stability of the magnetopause current layer, *J. Geophys. Res.*, 99, 4095 – 4104.
- Lapenta, G., and J. U. Brackbill (1997), A kinetic theory for the drift-kink instability, *J. Geophys. Res.*, 102, 27,099.
- Lapenta, G., and J. U. Brackbill (2002), Nonlinear evolution of the lower hybrid drift instability: Current sheet thinning and kinking, *Phys. Plasmas*, 9, 1544.
- Lapenta, G., J. U. Brackbill, and W. S. Daughton (2003), The unexpected role of the lower-hybrid drift instability in magnetic reconnection in three dimensions, *Phys. Plasmas*, 10, 1577 – 1587.
- Lee, E., K. W. Min, D.-Y. Lee, J. Seon, and K. J. Hwang (2002), Effect of b_y in three-dimensional reconnection at the dayside magnetopause, *Phys. Plasmas*, 9, 5070 – 5078.
- Lee, L. C., and J. R. Kan (1979), A unified kinetic model of the tangential magnetopause structure, *J. Geophys. Res.*, 84, 6417 – 6426.
- Lee, L. C., S. Wang, C. Q. Wei, and B. T. Tsurutani (1988), Streaming sausage, kink and tearing instabilities in a current sheet with applications to the earth's magnetotail, *J. Geophys. Res.*, 93, 7354.
- Lembege, B., and R. Pellat (1982), Stability of a thick two-dimensional quasineutral sheet, *Phys. Fluids (B)*, 25 (11), 1995.

- Lesch, H., and G. T. Birk (1997), Particle acceleration by magnetic field-aligned electric fields in active galactic nuclei, *Astron. Astrophys.*, *324*, 461–470.
- Lesch, H., and G. T. Birk (1998), On the origin of extended nonthermal optical emission in extragalactic jets, *Astrophys. J.*, *499*, 167–171.
- Lesch, H., and W. Reich (1992), The origin of the monoenergetic electrons in the arc of the galactic center. particle acceleration by magnetic reconnection, *Astron. Astrophys.*, *264*, 493–499.
- Lucek, E. A., P. Cargill, M. W. Dunlop, L. M. Kistler, A. Balogh, W. Baumjohann, K.-H. Fornacon, E. Georgescu, and G. Haerendell (2001), The magnetopause at high time resolution: structure and lower-hybrid waves, *Geophys. Res. Lett.*, *28*, 681 – 684.
- Luhmann, J. G., R. J. Walker, C. T. Russell, N. U. Crooker, J. R. Spreiter, and S. S. Stahara (1984), Patterns of potential magnetic field merging sites on the dayside magnetopause, *J. Geophys. Res.*, *89*, 1739 – 1742.
- Melrose, D. B. (1986), *Instabilities in space and laboratory plasmas*, Cambridge University Press, Cambridge.
- Mottez, F. (2003), Exact nonlinear analytic vlasov-maxwell tangential equilibria with arbitrary density and temperature profiles, *Phys. Plasmas*, *10*, 2501 – 2508.
- Nakamura, M., and M. Scholer (2000), Structure of the magnetopause reconnection layer and of flux transfer events: Ion kinetic effects, *J. Geophys. Res.*, *105*, 23,179 – 23,191.
- Øieroset, M., T. D. Phan, M. Fujimoto, R. P. Lin, and R. P. Lepping (2001), In situ detection of collisionless reconnection in the earth’s magnetotail, *Nature*, *412*, 414.
- Otto, A., L. C. Lee, and Z. W. Ma (1995), Magnetic field and plasma properties associated with pressure and magnetic pulses and magnetic reconnection at the dayside magnetopause, *J. Geophys. Res.*, *100*, 14,895 – 14,911.
- Ozaki, M., T. Sato, R. Horiuchi, and C. S. Group (1996), Electromagnetic instability and anomalous resistivity in a magnetic neutral sheet, *Phys. Plasmas*, *3*, 2265.

- Panov, E. (2004), Magnetopause crossings by cluster spacecraft, *private communication*.
- Parker, E. N. (1957), Sweet's mechanism for merging magnetic fields in conducting fluids, *J. Geophys. Res.*, *62*, 509.
- Parker, E. N. (1973), The reconnection rate of magnetic fields, *Astrophys. J.*, *180*, 247–252.
- Petschek, H. E., and R. M. Thorne (1967), The existence of intermediate waves in neutral sheets, *Astrophys. J.*, *147*, 1157–1163.
- Press, W. H., S. A. Teukolsky, W. T. Vetterling, and B. P. Flannery (1988), *Numerical recipes in C*, Cambridge University Press, Cambridge, New York, Port Chester, Melbourne, Sydney.
- Priest, E. R. (1976), Current sheet models of solar flares, *Solar Phys.*, *47*, 41.
- Priest, E. R. (2001), Three-dimensional reconnection on the sun, *EARTH PLANETS SPACE*, *53*, 483–490.
- Pritchett, P. L., and F. V. Coroniti (2004), Three-dimensional collisionless magnetic reconnection in the presence of a guide field, *J. Geophys. Res.*, *109*, A01,220.
- Pritchett, P. L., F. V. Coroniti, and V. K. Decyk (1996), Three-dimensional stability of thin quasi-neutral current sheets, *J. Geophys. Res.*, *101*, 27,413.
- Pulkkinen, T. I., D. N. Baker, R. J. Pellinen, J. Büchner, H. E. J. Koskinen, R. E. Lopez, R. L. Dyson, and L. A. Frank (1992), Particle scattering and current sheet stability in the geomagnetic tail during the substorm growth phase, *J. Geophys. Res.*, *97*, 19,283.
- Quest, K. B., and F. V. Coroniti (1981), Tearing at the dayside magnetopause, *J. Geophys. Res.*, *86*, 3289 – 3298.
- Russell, C. T. (2003), The structure of the magnetopause, *Planetary and Space Sciences*, *51*, 731–744.
- Schaefer, B. E., J. R. King, and C. P. Deliyannis (2000), Superflares on ordinary solar-type stars, *Astrophys. J.*, *529*, 1026–1030.

- Scholer, M., I. Sidorenko, C. Jaroschek, R. A. Treumann, and A. Zeiler (2003), Onset of collisionless magnetic reconnection in thin current sheets: Three-dimensional particle simulations, *Phys. Plasmas*, *10*, 3521 – 3527.
- Schopper, R., H. Lesch, and G. T. Birk (1998), Magnetic reconnection and particle acceleration in active galactic nuclei, *Astron. Astrophys.*, *335*, 26–32.
- Sergeev, V. A., D. G. Mitchell, C. T. Russell, and D. J. Williams (1993), Structure of the tail plasma/current sheet at 11 re and its changes in the course of a substorm, *J. Geophys. Res.*, *98*, 17,345.
- Sergeev, V. A., A. Runov, W. Baumjohann, R. Nakamura, T. L. Zhang, A. Balogh, P. Louarnd, J.-A. Sauvaud, and H. Reme (2004), Orientation and propagation of current sheet oscillations, *Geophys. Res. Lett.*, *31*, L05,807.
- Shapiro, V. D., V. I. Shevchenko, P. J. Cargill, and K. Papadopoulos (1994), Modulational instability of lower hybrid waves at the magnetopause, *J. Geophys. Res.*, *99*, 23,735 – 23,740.
- Shinohara, I. (2003), Formation of thin electron current layer associated with lower hybrid drift instability and its relation to quick reconnection triggering, *private communication*.
- Shukla, P. K., and A. A. Mamun (2002), Lower hybrid drift wave turbulence and associated electron transport coefficients and coherent structures at the magnetopause boundary layer, *J. Geophys. Res.*, *107*, SMP 34.
- Silin, I., and J. Büchner (2003), Kinetic instabilities of thin current sheets. results of 2 1/2d vlasov code simulations, *Phys. Plasmas*, *10*, 1299 – 1307.
- Silin, I., J. Büchner, and L. M. Zelenyi (2002), Instabilities of collisionless current sheets: Theory and simulations, *Phys. Plasmas*, *9*, 1104.
- Slavin, J. A., et al. (2002), Simultaneous observations of earthward flow bursts and plasmoid ejection during magnetospheric substorms, *J. Geophys. Res.*, *107*, 1106.

- Sonnerup, B. U. Ö. (1974), Magnetopause reconnection rate, *J. Geophys. Res.*, *79*, 1546 – 1549.
- Sonnerup, B. U. Ö., and B. G. Ledley (1979), Ogo-5 magnetopause structure and classical reconnection, *J. Geophys. Res.*, *84*, 399 – 405.
- Sonnerup, B. U. Ö., G. Paschmann, I. Papamastorakis, N. Sckopke, G. Haerendel, S. J. Bame, J. R. Asbridge, J. T. Gosling, and C. T. Russell (1981), Evidence for magnetic field reconnection at the earth's magnetopause, *J. Geophys. Res.*, *86*, 10,049.
- Sundaram, A. K., and D. H. Fairfield (1995), Localized tearing modes in the magnetotail driven by curvature effects, *J. Geophys. Res.*, *100*, 3563.
- Sundaram, A. K., and D. H. Fairfield (1996), The tearing instabilities driven by lower hybrid waves in the current sheet, *J. Geophys. Res.*, *101*, 24,919.
- Swisdak, M., B. N. Rogers, J. F. Drake, and M. A. Shay (2003), Dianagnetic suppression of component magnetic reconnection at the magnetopause, *J. Geophys. Res.*, *108*, SMP 23.
- Syrovatskii, S. I. (1971), Formation of current sheets in a plasma with a frozen-in strong magnetic field, *Sov. Phys. JETP*, *33*, 933.
- Tanaka, M., and T. Sato (1981), Simulations on lower hybrid drift instability and anomalous resistivity in the magnetic neutral sheet, *J. Geophys. Res.*, *86*, 5541.
- Tsyтович, V. (1995), *Lectures on non-linear plasma kinetics*, 349-353 pp., Springer, Berlin, Heidelberg, New York.
- Vaisberg, O. L., et al. (1983), Fine structure of the magnetopause based on measurements on the prognoz-7 and prognoz-8 satellites, *Kosmich. Issled.*, *21*, 57 – 63.
- Vaivads, A., M. André, S. C. Buchert, J.-E. Wahlund, A. N. Fazakerley, and N. Cornilleau-Wehrlin (2004), Cluster observations of lower-hybrid turbulence within thin layers at the magnetopause, *Geophys. Res. Lett.*, *31*, L03,804.

- Wiegelmann, T., and J. Büchner (2002), Evolution of magnetic helicity under kinetic magnetic reconnection. Part II $B \neq 0$ reconnection, *Nonlinear Proc. Geoph.*, *9*, 139–147.
- Winske, D. (1981), Current-driven microinstabilities in a neutral sheet, *Phys. Fluids*, *24(6)*, 1069.
- Winske, D., and P. C. Liewer (1978), Particle simulation studies of the lower hybrid drift instability, *Phys. Fluids*, *21(6)*, 1017.
- Yamanaka, K. (1978), Threshold of electromagnetic instability in a magnetic neutral sheet, *Physica Scripta*, *17*, 15.
- Yoon, P. H., and A. T. Y. Lui (2004), Model of ion or electron dominated current sheet, *private communication*.
- Yoon, P. H., A. T. Y. Lui, and H. K. Wong (1998), Two-fluid theory of drift-kink instability in a one-dimensional neutral sheet, *J. Geophys. Res.*, *103*, 11,875.
- Yoon, P. H., A. T. Y. Lui, and M. I. Sitnov (2002), Generalized lower-hybrid drift instabilities in current-sheet equilibrium, *Phys. Plasmas*, *9*, 1526.
- Zhu, Z., and R. M. Winglee (1996), Tearing instability, flux ropes, and the kinetic current sheet instability, *J. Geophys. Res.*, *101*, 4885.

Curriculum Vitae

- Name: Silin, Illia Vladimirovich
- Birthdate: 30 August 1976
- Birthplace: The Crimea, Ukraine
- Parents: Vladimir Silin and Anna Silina, born Vinogradova
- Education and research:
 - Nauchnyi Secondary and High School, the Crimea, Ukraine, 1983 - 1993
(with a golden medal)
 - Master of Sciences in Physics (with honours) from Physics Department at Moscow State University, Moscow, Russian Federation, 1993 - 1999
 - Topic of the Master degree project: The possibility of radio-tomography in the magnetosphere by a group of closely-positioned spacecraft
 - Junior scientist researcher at Space Plasmas Laboratory, Space Research Institute of Russian Academy of Sciences, Moscow, Russian Federation, January 1999 - July 2000
 - Visiting scientist at Max-Planck Institut für Aeronomie, Germany, August 2000 - December 2000
 - Promotionsstipendium: Max-Planck Gesellschaft, at Max-Planck Institut für Aeronomie, Germany, January 2001 - July 2001
 - Promotionsstipendium: Deutscher Akademischer Austauschdiens, at Technische Universität Carolo-Wilhelmina zu Braunschweig, Germany, October 2001 - July 2004